

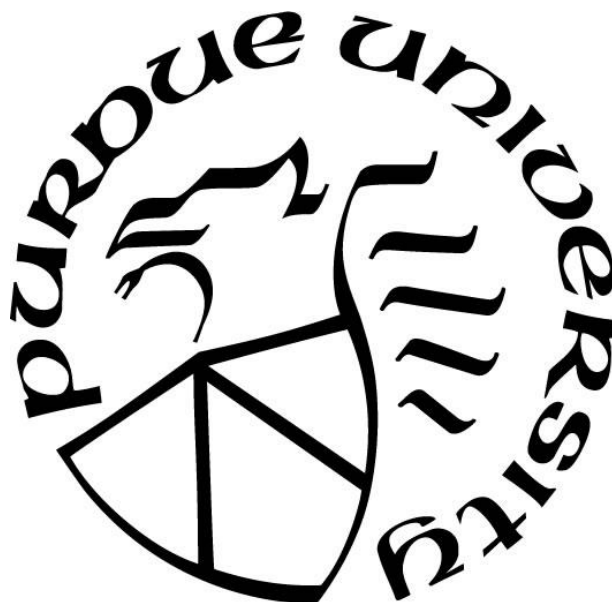
**MOLECULAR TRANSPORTATION IN POLYMER AND COMPOSITE
MATERIALS: BARRIER PERFORMANCE AND MECHANICAL
PROPERTY EVALUATION**

by
Md Nuruddin

A Dissertation

*Submitted to the Faculty of Purdue University
In Partial Fulfillment of the Requirements for the degree of*

Doctor of Philosophy



School of Materials Engineering
West Lafayette, Indiana
May 2020

THE PURDUE UNIVERSITY GRADUATE SCHOOL
STATEMENT OF COMMITTEE APPROVAL

Dr. John Howarter, Chair

School of Materials Engineering

Dr. Jeffrey Youngblood, Chair

School of Materials Engineering

Dr. Kendra Erk

School of Materials Engineering

Dr. Andrew Whelton

Lyles School of Civil Engineering
Environmental and Ecological Engineering

Approved by:

Dr. David Bahr

Dedicated to my Parents, Wife and my Son

ACKNOWLEDGMENTS

First of all, I would like to thank my advisors Dr. Howarter and Dr. Youngblood for their continuous support and assistance over the course of my graduate studies at Purdue University. This work would not be possible without help of Dr. Erk and Dr. Whelton, who always expanded their helping hand to guide me in the right direction for my research work despite of their busy schedule.

Second, I would like to express my deepest gratitude to my lab mate Dr. Reaz Chowdhury, Dr. Gamini Mendis, Dr. Logan Kearney and Caitlyn Clarkson for keeping me motivated throughout my graduate studies through motivational speeches, helping hand and priceless guidelines.

Third, I am thankful to Seyedeh Sendesi, Kyungyeon Ra, Xianzhen Li, Hyungyung Jo, Dr. Francisco Montes, and Dr. Nelyan Lopez-Perez for technical assistance, support, and patience. They were always active to provide me their technical help to conduct my research work. Finally, I would like to thank my family for their love, support, and understanding during my graduate studies at Purdue University.

TABLE OF CONTENTS

LIST OF TABLES	9
LIST OF FIGURES	10
ABSTRACT	12
CHAPTER 1. INTRODUCTION	14
1.1 Background and Motivation	14
1.2 Research Objectives	15
1.3 Outline of the thesis	16
CHAPTER 2. EVALUATION OF THE PHYSICAL, CHEMICAL, MECHANICAL, AND THERMAL PROPERTIES OF STEAM-CURED PET/POLYESTER CURED-IN-PLACE PIPE	17
2.1 Introduction.....	17
2.2 Materials and Methods.....	20
2.2.1 Materials	20
2.2.2 Curing of uncured resin tube in the laboratory	20
2.2.3 Aging of onsite-cured CIPP samples	21
2.2.4 Thermogravimetric analysis (TGA)	21
2.2.5 Differential scanning calorimetry (DSC).....	21
2.2.6 Proton nuclear magnetic resonance (¹ HNMR) analysis	21
2.2.7 Chemical extraction and GC/MS analysis of CIPPs.....	22
2.2.8 Absorption and swelling test	23
2.2.9 Thickness measurement.....	23
2.2.10 Porosity measurement	23
2.2.11 Density measurement	24
2.2.12 Flexural testing	24
2.2.13 Fracture surface analysis	25
2.3 Results and Discussion	25
2.3.1 Physical and mechanical properties of the exhumed CIPP	25
2.3.2 Thermal Behavior: Exhumed CIPPs vs. Oven Cured CIPP Material.....	27
2.3.3 Chemical analysis of leaching organic compounds.....	31

2.3.4	Interaction of Water with CIPP Specimens	34
2.4	The effect of water conditioning on physical and mechanical properties	36
2.5	Summary	38
CHAPTER 3. INFLUENCE OF AGGRESSIVE ENVIRONMENTAL AGING ON MECHANICAL AND THERMO-MECHANICAL PROPERTIES OF UV-CURED CIPP LINERS		40
3.1	Introduction.....	40
3.2	Materials and Experiment	42
3.2.1	Materials	42
3.2.2	Differential scanning calorimetry (DSC).....	44
3.2.3	Thermogravimetric analysis (TGA)	44
3.2.4	Aging solution and experiments	45
3.2.5	Absorption and swelling tests	45
3.2.6	Energy dispersive spectroscopy (EDS)	46
3.2.7	Accelerated aging of onsite-cured CIPP samples	46
3.2.8	Headspace gas chromatography-mass spectroscopy (HS GC-MS).....	46
3.2.9	Inter-laminar shear strength (ILSS) characterization	47
3.2.10	Fracture surface analysis	48
3.2.11	Dynamic mechanical analysis (DMA)	48
3.3	Results and discussion	48
3.3.1	Thermal Behavior of CIPP Specimens	48
3.3.2	Solution Uptake and Diffusion Behavior of CIPP Liners	50
3.3.3	Role of Nature of Solution in Extracting Styrene from CIPPs into Water	55
3.3.4	Effect of Aging on Interlaminar Shear Strength of CIPP Liners	56
3.3.5	Effect of Aging on Viscoelastic Properties of CIPP Liners	58
3.4	Summary	62
CHAPTER 4. THE INFLUENCE OF FREE VOLUME DETERMINED BY POSITRON ANNIHILATION LIFETIME SPECTROSCOPY (PALS) ON GAS PERMEABILITY OF CELLULOSE NANOCRYSTALS FILMS		64
4.1	Introduction.....	64
4.2	Materials and Experiments	66

4.2.1	Materials	66
4.2.2	Preparation of CNC Film.....	66
4.2.3	Preparation of CNC coated Polypropylene (PP)	67
4.2.4	Herman's order parameter determination	68
4.2.5	Gas permeability measurement.....	69
4.2.6	Positron Annihilation Lifetime Spectroscopy	69
4.3	Results and Discussions.....	71
4.3.1	Alignment of CNCs within Films.....	71
4.3.2	Free volume of self-organized and shear-oriented CNC films.....	72
4.3.3	Effect of alignment on gas barrier performance of CNC films	74
4.3.4	Comparison of barrier performance of CNC films with other commercial polymers.....	75
4.3.5	Dil model for the prediction of gas permeability.....	77
4.3.6	Summary.....	80
CHAPTER 5. GAS AND WATER VAPOR BARRIER PERFORMANCE OF CELLULOSE NANOCRYSTALS-CITRIC ACID COATED POLYPROPYLENE FILM FOR FLEXIBLE PACKAGING		81
5.1	Introduction.....	81
5.2	Materials and Experiments	83
5.2.1	Materials	83
5.2.2	Preparation of coating.....	83
5.2.3	Application of Coating	84
5.2.4	Wet coating properties	84
5.2.5	Characterization of Coated Films	84
5.2.6	Barrier Properties of the Films	85
5.2.7	Contact Angle Measurement	86
5.3	Results and Discussions.....	87
5.3.1	Wet Coating Properties.....	87
5.3.2	Coating Characterization	89
5.3.3	Contact Angle	92
5.3.4	Barrier performance of coated films.....	93

5.3.5 Comparison of Barrier performance of CNC-CA coated PP with other commercial Polymers	97
5.4 Summary	100
CHAPTER 6. CONCLUSION AND FUTURE WORK	101
6.1 Thermal and UV-aging of CIPP liners.....	102
6.2 Barrier performance of CNC films at higher relative humidity.....	102
6.3 Improve the hydrophobicity of CNC Film.....	102
6.4 Investigate the solvent-free process to disperse the CNC into extrudable polymers.....	102
APPENDIX A	104
APPENDIX B	113
APPENDIX C	117
APPENDIX D	124
REFERENCES	134
VITA	154
PUBLICATIONS.....	155

LIST OF TABLES

Table 2.1 Thermal behavior of uncured, onsite-cured, and oven-cured CIPP liners.....	30
Table 2.2 Organic molecules detected from ¹ H-NMR spectra and GC-MS of leachate solutions of CIPP liners ^a	33
Table 3.1 Thermal properties of CIPP from installation site-1 and site-2.....	50
Table 3.2 Equilibrium sorption and Fickian diffusion coefficient of CIPP specimens from Site-1 and site-2 for water, salt and pore solution.	52
Table 3.3 Surface concentration of ions for the CIPP specimens.....	55
Table 3.4 Styrene concentration of samples detected and quantified by GC-MS.	56
Table 4.1 o-Ps Characteristics, Pore Radii, and fractional free volume for self-organized and shear-oriented CNC films.	73
Table 5.1 Chemical ingredients and amounts used to prepare barrier coatings.....	83
Table 5.2. Thickness, grammage and roughness of the CNC and CNC-CA coatings. Data are expressed as mean values \pm SD.	90
Table 5.3 . WVTR of CNC-CA coated PP films, compared with other commercially available polymer films.....	99

LIST OF FIGURES

Figure 2.1 Onsite installed CIPP in Indiana sites. The outer surface is in contact with the cold host pipe while the inner surface is in contact with hot steam during installation and curing.	19
Figure 2.2 Physical properties of the inner and outer layers of the exhumed CIPP.	26
Figure 2.3 DSC thermograms of uncured resin liner, inner layer of the onsite-cured CIPP, outer layer of the onsite-cured CIPP, and oven-cured CIPP liners. DSC performed in nitrogen atmosphere showing the heating portion of heat-cool-heat scan for each sample.....	28
Figure 2.4 (a) Thermogravimetric (TG) and (b) Derivative thermogravimetric (DTG) curves of uncured, onsite-cured, and oven-cured CIPP liners.....	30
Figure 2.5 TGA weight loss of uncured, onsite-cured, and oven-cured CIPP liners at 120 °C and 160 °C.	31
Figure 2.6 Weight (a) and thickness (b) change of inner and outer layers of CIPP as a function of immersion time.	35
Figure 2.7 Debonding between the coating layer and the composite layer of the CIPP before and after condition.	35
Figure 2.8. Porosity and density of the inner and outer layers of the non-conditioned and water-conditioned CIPP specimens.....	36
Figure 2.9 Flexural strength and modulus of the CIPP samples before and after conditioning. ..	37
Figure 2.10 Optical microscope images of fracture surface of as-received and conditioned CIPP.	37
Figure 2.11 SEM images of the fracture surface of non-conditioned, water-conditioned and chloroform-conditioned CIPP specimens.	38
Figure 3.1 UV-cured CIPP liners.....	43
Figure 3.2 DSC curves of CIPP specimens from site-1 and site-2.	49
Figure 3.3 Weight gain vs time curves of site-1 and site-2 CIPP samples for water, salt and pore solution aging.....	51
Figure 3.4 Morphology of as-received CIPP specimens from site-1 and after aging with water, salt and pore solution.....	53
Figure 3.5 Interlaminar shear strength (ILSS) of CIPP from site 1 and 2 at different environment conditions.....	56
Figure 3.6 Optical images and Scanning electron microscopic images of fracture surface of as-received and aged CIPP specimens.....	60
Figure 3.7 Glass transition temperature (T_g) and storage modulus of as-received and aged CIPP from 2 different installation sites.	61

Figure 4.1 Schematic of preparation of self-organized and shear-oriented CNC films.....	67
Figure 4.2 Schematic of preparation of CNC coated PP films.	68
Figure 4.3 Experimental setup for PALS measurement.	70
Figure 4.4 (a) self-organized, and (b) shear-oriented CNC films with light transmittance value and optical microscopy images.....	72
Figure 4.5 (a) O-Ps lifetime (τ_3) and pore radius (r), (b) O-Ps intensity (I ₃) and fractional free volume (FFV) of self-organized and shear-oriented CNC films.	73
Figure 4.6 Oxygen and carbon dioxide permeability of self-standing (chiral) and shear oriented (aligned) CNC films.....	75
Figure 4.7 Plot of oxygen permeability of cellulose films as a function of relative free volume and comparison with other engineering polymers. Details of quantitative data for this plot can be found in Table C2.....	76
Figure 4.8 Plot of carbon dioxide permeability of cellulose films as a function of relative free volume and comparison with other engineering polymers. Details of quantitative data for this plot can be found in Table C2.	77
Figure 4.9 Comparison of the modified Dil and modified Bharadwaj model with experimental permeability data for oxygen and carbon dioxide.....	80
Figure 5.1. Effect of citric acid on surface tension of CNC suspensions.	87
Figure 5.2 Steady-state viscosity vs shear rate for CNC and CNC-CA suspensions.	88
Figure 5.3 The shear stress and shear strain rate of CNC aqueous suspensions at different concentrations, (b) The relationship between the flow index (n) and CA concentration in CNC suspensions.	89
Figure 5.4 AFM 3D images (10 X 10 mm ²) of uncoated and coated polypropylene (PP).	91
Figure 5.5 Optical transparency of CNC and CNC-CA coated PP films.	92
Figure 5.6. Variation of contact angle with time for uncoated and coated PP.	93
Figure 5.7 Oxygen and carbon dioxide permeability of CNC film with varying amount of CA.	94
Figure 5.8 Schematic diagram of gas transmission through CNC and CNC-CA film.	95
Figure 5.9 Oxygen permeability of CNC and CNC-CA coated PP films.....	96
Figure 5.10 . Water vapor transmission rate (WVTR) of CNC and CNC-CA coated PP films. ..	97

ABSTRACT

Transport of gasses and liquids through polymers and composites is an important factor to be considered when designing a material for structure and packaging applications. For structural engineering applications, more focus has been given to the transportation of water, vapor and organic liquids rather than gases as diffusion of these liquids into the polymers and polymer-based composites can significantly lower service life. In addition, much attention has been given to the leaching of unreacted reactant molecules, solvents, additives, degradation products from the polymers and composites to the atmosphere (water, soil etc.). We studied the transport of volatile organic compounds and water in cured-in-place-pipe (CIPP) (a representative of FRPC) and gas permeability of highly engineered cellulose nanocrystals (CNC) films.

Cured-in-place-pipe (CIPP) is a popular technology which uses fiber reinforced polymer composite to repair sanitary sewer, stormwater, and drinking water pipe. The liner is installed in the field and exposed to flowing water immediately after installation (curing of the liner) is done. Curing conditions dictate liner properties as undercured liners can contain unreacted styrene monomers, additives, degradation products. These agents can leach out and enter the environment (soil, water, air). The objective of this work was to investigate the curing behavior, volatile content, thermal stability of steam-cured and UV-cured CIPP liners collected from Indiana and New York installation sites. The liner specimens were also exposed to water and other aggressive environmental conditions (saltwater, concrete pore solution at 50 °C) to explore the leaching of unreacted styrene and other organic chemicals from the liners. The influence of transportation of water, salt solution and pore solution through liners on mechanical and thermo-mechanical properties was also examined to study the durability of the liners. Study suggested that the durability of the liners depends on the curing condition and exposed environment conditions.

The function of polymer packaging materials is mainly to inhibit gas and moisture permeation through the films. Cellulose nanocrystals (CNCs) have drawn growing interest for the packaging due to their non-toxicity, abundance in nature, biodegradability and high barrier properties. The objective of this work was to correlate the alignment of CNC with free volume and barrier performance of the film. Furthermore, citric acid (CA) was added to the CNC suspensions with varying quantity to explore the effect of CA on coating quality and barrier performance of CNC coated polypropylene (PP) film. Study revealed that CA addition in CNC suspension can enhance

the hydrophobicity and gas barrier performance of coated PP films while retaining the high optical transparency.

CHAPTER 1. INTRODUCTION

1.1 Background and Motivation

The transportation of small molecules (gas, water, solvent) through polymers and composite has an important role in the development of economical industrial product for both structure and packaging applications. Polymer and composite materials which is in contact with water, vapors, or low molecular weight organics, can be affected significantly as those molecules can create a local strain in the polymers and can change the properties of the products, including loss of barrier properties, loss of adhesive strength, undesirable appearance of cracks, and leaching of polymer fragments, solvent or unreacted reactant molecules [1–3]. Furthermore, the permeability of gas and water vapors through packaging polymers plays a vital role as packaging polymers are designed to barrier performance for the passage of the gas and vapors. However, the transportation of small molecules through polymer and composites consists of three steps: (1) sorption of species (penetrant) on the surface of the polymers, (2) diffusion of the penetrant species through the materials, and (3) desorption of the penetrant species from the materials [4].

Cured-in-place pipe (CIPP), a trenchless technology has been used worldwide for the past 40 years in drinking water, sewerage and storm water pipe rehabilitation because of its ease of installation and the targeted service life has been considered as long as 50 years [5]. Recent studies reported that during and after CIPP installation, unreacted styrene monomers and some other chemicals leached to nearby water and threatened the environment [6–9]. Furthermore, water from pipeline may infiltrate into the liners which can change the mechanical and physical properties of the CIPP liners. No detailed studies have been performed on the effect of leaching of small organic molecules and exposed to aggressive environment on mechanical performance of CIPP liners.

As for packaging polymers, the barrier performance of the packaging materials is an important consideration. Petroleum based polymers are widely used for packaging applications because of their low cost, easy processability, and superior performance. However, much focus has been given to environmentally friendly biodegradable polymers to develop next generation packaging polymers because of gradual depletion of the petroleum-based resources and adverse environmental effects of petroleum-based polymers. Cellulose nanocrystals can be a promising alternative to traditional petroleum-based polymers to developing next generation packaging

materials because of their high crystallinity (around 85%), biodegradability, low cost , and high mechanical properties (the strength and axial modulus are 7.5–7.7 GPa and 110–220 GPa, respectively) [10,11]. Unfortunately, there is a great challenge for the application of cellulose nanocrystals as a packaging film as CNC films are highly brittle in nature. So, the alternative approach for utilizing CNC in barrier packaging applications is to utilize them as coating materials on traditional engineering polymers to improve the barrier performance.

1.2 Research Objectives

The aim of this study is to understand the effect of molecular transportation of small molecules from CIPP liners to the surrounding and from surrounding to the liners, on mechanical performance of the liners, and to investigate the molecular transportation of gas and vapor through cellulose nanocrystals-based packaging films. In particular, the specific objectives are listed below:

1. Investigate the physical and thermal properties of steam-cured and UV-cured CIPP liners collected from CIPP installation sites (Indiana and New York). Also, explore the effect of water and aggressive environmental aging on mechanical and viscoelastic properties of CIPP liners. DSC and TGA were used to investigate the volatile content, curing condition examination.
2. Examine the structure-property relationship of CNC as a coating material for packaging applications. In this process, investigate the effect of CNC alignment on free volume and barrier performance of CNC films. For measuring the barrier performance, we designed and built a gas permeability rig. The free volume of CNC with different structural arrangements were investigated by PALS instrument.
3. Investigate the coating quality of CNC/citric coating formulation for packaging applications. Explore the effect of addition of citric into CNC suspension on wet coating quality and barrier performance of coated film. Rod coating was used to apply uniform CNC coating on PP substrate.

1.3 Outline of the thesis

This thesis is categorized into four main ideas to investigate the molecular transportation in polymers and polymer-based composites. Chapter 2 demonstrated the physical properties (porosity, density) and thermal properties (residual curing, volatile content and thermal stability) of inner and outer layer of steam cured CIPP liners which is made of PET felt reinforced unsaturated polyester resin. The liners were immersed in water for a short-term to examine the leaching of organic chemicals and also observed influence of water on mechanical performance of the liners. Chapter 3 investigated the effect of aggressive environmental conditions such as water, salt solution and simulated concrete pore solution at moderate temperature on mechanical and thermo-mechanical performance of UV-cured CIPP liners made of fiber glass reinforced vinyl ester resin. Thermal properties of the liners from two different installation sites were investigated to observe the residual curing, volatile content and decomposition behavior of the liners. Chapter 4 demonstrated the free volume and barrier performance of CNC films with different structure arrangements of CNC domains (self-standing and shear-oriented CNC films). Modified conventional Bharadwaj model was proposed for a single component CNC films to predict the gas permeability with variation of CNC alignment. Chapter 5 demonstrated the CNC and CNC-citric acid coated polypropylene film to explore the barrier performance and coating quality of the coated films.

CHAPTER 2. EVALUATION OF THE PHYSICAL, CHEMICAL, MECHANICAL, AND THERMAL PROPERTIES OF STEAM-CURED PET/POLYESTER CURED-IN-PLACE PIPE

All research work except GC-MS and three-point bending was performed by Md Nuruddin. All analysis except GC-MS analysis was performed by Md Nuruddin with guidance by Prof. John Howarter and Jeffrey P. Youngblood. All writing was performed by Md Nuruddin with guidance and editing by Prof. John Howarter, Jeffrey P. Youngblood, and Andrew Whelton.

The following chapter contains content reproduced with permission from Md Nuruddin, Gamini Mendis, Kyungyeon Ra, Seyedeh Mahboobeh Teimouri Sendesi, Tyler Futch, Johnathan Goodsell, Andrew J. Whelton, Jeffrey P. Youngblood, John A. Howarter "Evaluation of the physical, chemical, mechanical, and thermal properties of steam-cured PET/Polyester cured-in-place pipe (CIPP)," *Journal of Composite Materials* 53 (19), 2687-2699, 2019.

2.1 Introduction

Cured-in-placed-pipe (CIPP) is a trenchless technology which has been used worldwide over the past 40 years to repair existing storm, sewer, and drinking water pipelines [12]. CIPP resin technology typically uses thermoset polymer matrices, reinforced by fiberglass mats or polyethylene terephthalate (PET) felts. Generally, a combination of vinyl ester or polyester resins are used with styrene monomers (30-50% by weight) and silica (1-5% by weight) [13–15]. The resin is typically blended with peroxide initiators, plasticizers, and solvents (i.e., styrene for unsaturated polymer). While styrene-free vinyl ester resin [16,17] and epoxy resins can be used to replace styrene-based vinyl ester or polyester resin [17], these technologies are considerably more expensive. Styrene is a low-cost monomer and serves multifunctional purposes in the resin formulation; styrene is used as a diluent to reduce resin viscosity and can also react during the curing process contributing to the final material network, after free radical polymerization is initiated by the thermal or photochemical decomposition of the peroxide initiators.

Hypothetically, proper curing procedures and the implementation of physical barrier layers should prevent chemicals from migrating from the resin into the environment, however improperly cured materials and poorly controlled processes can lead to contamination. Curing of the CIPP thermoset resin-impregnated felts is performed using hot water, pressurized steam, or ultraviolet (UV) light. The inner surface of the CIPP resin assembly (Figure 2.1) is typically exposed to hot water at $180 \pm 10^\circ\text{F}$ or steam at $210\text{--}250^\circ\text{F}$ during the curing process [18]. The curing time depends

upon the desired CIPP thickness, and can be 3-6 hours for hot water curing and 1.5-2.5 hours for steam curing [18]. The curing time should be chosen so that CIPP is able to fully cure through the entire thickness of the pipe (i.e. thicker pipe walls necessitate longer cure times). However, local conditions (e.g. cold outer surfaces) may inhibit complete curing. The inner surface of the presaturated felt or fiberglass is coated with a thermoplastic polymer such as polypropylene, polyethylene, etc. to restrict the resin ingredients from contacting the hot water or steam during curing [15,19]. However, a number of studies have demonstrated that various organic chemicals can migrate into the environment [5,15,19–21].

Deviations from the recommended curing conditions may deteriorate the expected mechanical performance as well as longevity of the liners. Non-uniform curing temperatures can lead to a low degree of crosslinking and weaker fiber reinforcement, which may ultimately reduce the service life of the finished liner because of lower mechanical (interlaminar shear strength) and thermal properties (glass transition temperature and storage modulus) [22,23]. In contrast, pressure is applied to squeeze out resin from the spaces between the individual fibers and from the space between adjacent plies [24]. Insufficient curing pressure can cause poor ply consolidation, entrapped air or excess residual volatiles within the composites [25]. Entrapped volatiles may leach out to the environment, contaminate the water and leave voids within the composite. The presence of voids can weaken the matrix-dominated mechanical properties (shear and compressive strength) as a result of induced localized stress concentration [25,26]. These voids can be elongated and create porosity at the fiber-matrix and ply interface [27]. Proper pressure during curing can squeeze out the entrapped volatiles or voids, giving finished composites with better service life. Composite structures with higher void content have lower mechanical properties [25–29]. Thus, CIPP liner with higher void content will not meet the expected service life.

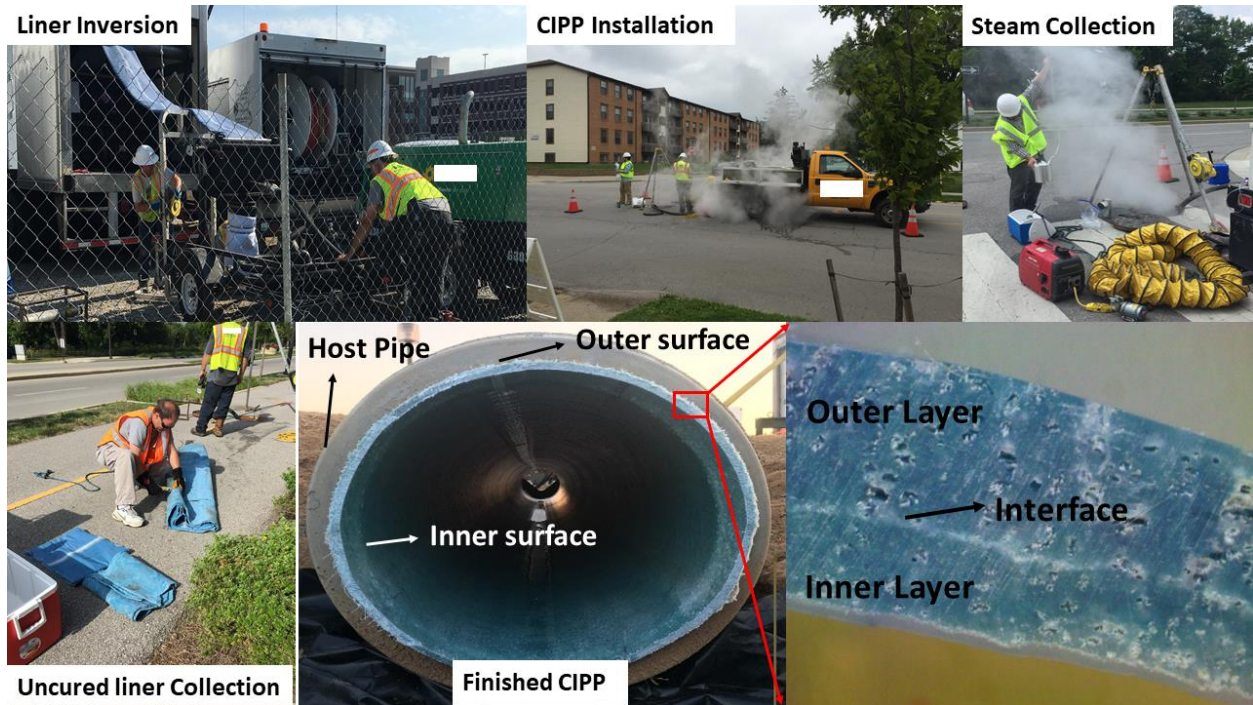


Figure 2.1 Onsite installed CIPP in Indiana sites. The outer surface is in contact with the cold host pipe while the inner surface is in contact with hot steam during installation and curing.

CIPP developers have claimed that CIPPs have a service lifetime of approximately 50 years [30]. To our knowledge, these claims have not been validated in the peer-reviewed literature, and CIPP technology was developed 40 years ago [31]. Likely, the structural lifetime of the CIPP largely depends upon (1) physical (length, diameter, type of reinforcing materials such as PET felts or fiberglass, type of resin, liner thickness) (2) functional (operating conditioned like temperature and pressure, regular maintenance strategies) and (3) surrounding (soil type, weather condition, ground water, aggressive chemicals etc.) factors. Some studies have reported on the mechanical and physical properties of onsite installed CIPP liners, but until now, no reports have investigated the effects of environmental conditioning on the mechanical and physical properties of CIPP.

The goal of this study was to better understand properties of newly installed CIPPs. Specific objectives were to: (1) to identify the physical, thermal and mechanical properties across the thickness of the onsite installed CIPP, (2) to compare the physical and thermal properties of the onsite-cured CIPP with laboratory, oven-cured CIPP (3) to identify the composition of organic chemicals which can be extracted from onsite-cured CIPP and compared with oven-cured CIPP,

and (4) to determine the effects of water conditioning on the physical and mechanical properties of CIPP.

2.2 Materials and Methods

2.2.1 Materials

In July 2016, CIPPs were installed using the steam curing process inside 45.7 cm diameter vitrified clay sanitary sewer pipes in Indiana. According to contractor provided materials, the resin-impregnated felt consisted of ITI 191024 CTD Felt 15 mil 69 (11% wt. to 29% wt.), high molecular weight isophthalic unsaturated polyester 102T/TA resin, (38% wt. to 47% wt.), amorphous fumed silica (0% wt. to 2% wt.), styrene (15% wt. to 31% wt.), various organic peroxides (0.5% wt. to 0.7% wt.), fiberglass (0% wt. to 20% wt.), and proprietary filler(s) (0% wt. to 22% wt.). The resin impregnated tube liner consisted of two layers of flexible PET felt which helped obtain the desired CIPP thickness [32].

While onsite, the authors collected uncured resin tube samples, and the contractors cut samples of newly installed CIPP (7-8 mm thick) from the end of the newly installed CIPP. Fabric was also obtained that had not been impregnated with resin. Resin containing materials were stored at 0 °C until analysis. The fabric (without resin) was stored at room temperature.

A variety of analytical standards were used for this study. Chloroform ($\geq 99.5\%$, containing 100-200 ppm amylenes as stabilizer), dichloromethane ($\geq 99.8\%$, containing 40-150 mg/L amylene as stabilizer), hexane ($\geq 97.0\%$), and deuterium oxide (for NMR, deuteration degree min. 99.9%) were purchased from Sigma Aldrich Inc. Chloroform-d, for NMR, (99.8+% atom D, contains 0.03 v/v% TMS) was purchased from Fisher Scientific. The lists of analytical standards for the quantitative gas chromatography/mass spectrometry (GC/MS) are given in Appendix A.

2.2.2 Curing of uncured resin tube in the laboratory

The maximum curing temperature of the uncured resin tube was determined by Differential Scanning Calorimetry (DSC) analysis [Appendix A, Figure A-1]. The collected uncured resin tube was cut into 10"×10" squares and heated in the oven at 110 °C for 2 hours. No pressure was applied.

2.2.3 Aging of onsite-cured CIPP samples

Onsite-cured CIPP samples were cut using a water jet cutting machine to 120 mm (length) \times 12.5 mm (width) \times 7.5 mm (thickness). The samples were polished to achieve a smooth surface using 2000 and 320 grit micro-fine sandpaper.

Sample immersion tests in distilled water were conducted according to the ASTM D543-14 standard. Ten samples were immersed in 500 ml solution in a 500 ml glass bottle with PTFE lined caps and kept in the oven at 40 °C for 7 days. At the end of test, the samples were taken out of the solution and kept at 23 °C and 50% relative humidity for 48 hours, according to the ASTM D618-13 standard.

2.2.4 Thermogravimetric analysis (TGA)

The thermal stability, and the volatile content of the onsite-cured CIPP (inner and outer layers), the uncured and oven-cured CIPP liner were studied using a Q-500 thermogravimetric analyzer and platinum pans, both from TA Instruments Inc. (Delaware, USA). Sample weight was maintained between 10-15 mg and a gas purge flow rate of 60 mL/min was used. Samples were heated at 10 °C/min to 160 °C in a nitrogen atmosphere and held for 120 minutes to examine the volatilization of organic compounds and the evaporation of styrene. Samples were further heated at 10 °C/min to 900 °C in air to examine the degradation of the composite material.

2.2.5 Differential scanning calorimetry (DSC)

Curing behavior and thermal analysis of the inner and outer layers of the onsite-cured CIPP, the uncured resin tube and the oven-cured resin tube were performed using a Q-2000 differential scanning calorimeter (TA Instruments Inc., Delaware, USA). Aluminum sealed pans were used with sample weight of approximately 10 mg and scans were performed at 20 °C/min from -25 to 200 °C. A heat-cool-heat cycle was used during the experiment to understand residual curing behavior and the emission of volatile chemicals.

2.2.6 Proton nuclear magnetic resonance (¹HNMR) analysis

150 mg of onsite-cured CIPP (inner and outer layers of CIPP), uncured resin tube, and oven-cured resin tube were immersed in 1.5 ml of deuterated chloroform in 20 ml glass vials with

PTFE caps and kept in the oven at 40 °C for 24 hours. At the end of the 24-hour period, the extracted chemicals were separated out from the residue using syringe filters with polypropylene housing (0.45 µm pore size and a polypropylene membrane) and was placed in a NMR tube. ¹H NMR spectra were collected using 64 scans on a 500 MHz Bruker spectrometer (Bruker BioSpin, Fremont, CA, USA) equipped with TopSpin software. The ¹H NMR peaks were analyzed using MestReNova software. Initially the tentative organic compounds were identified by using ChemOffice Professional 16 software. Finally, ¹H NMR was conducted on standards chemicals for the confirmation of the tentatively identified compounds.

2.2.7 Chemical extraction and GC/MS analysis of CIPPs

Subsamples of all CIPPs were obtained by cutting through the wall of the CIPP with a drill. Subsamples were cut into spirals to increase the contact surface area of the CIPP with the extraction solutions. Dichloromethane was used as the extraction solvent due to its non-polarity and prior use for uncured resin tubes for CIPP [5]. About 3 g of CIPP sample was added to a 20 mL amber glass vial with a PTFE cap and filled with an extraction solution. The experiments (uncured, onsite-cured and oven-cured CIPP) were performed in triplicate. Extractant solutions were stored in a dark at room temperature for 3-days, based on previous experimental results [5]. After 3-days extraction, solvents were filtered through a 0.2 µm PTFE filter to prevent any solids from entering the GC/MS. Filtered samples were analyzed using a Shimadzu GC/MS-TQ8040 (Shimadzu Scientific Instruments, MD, USA). Each extract was diluted by a factor of 10 except for the uncured resin. Uncured resin was diluted by a factor of 1000 to avoid saturation of the column by highly concentrated chemicals. 1,4-Dichlorobenzene-d₄ (1 mg/L) was the internal standard and was added to 1.5 mL samples. The helium carrier gas for the GC/MS was used at a 3.0 mL/min purge flow rate and a 1.5 mL/min column flow rate. Samples were injected in split mode with a 1:10 ratio at 280 °C. The cut time for the dichloromethane samples was 1.8 min to 27.50 min and was 2.5 min to 27.5 min for the hexane samples. Syringes were rinsed in methanol three times between each injection. Analytical standards for the confirmation and quantification of the organic compounds in the GC/MS are shown in the Appendix A.

2.2.8 Absorption and swelling test

Three specimens of 8 mm (width) \times 10 mm (length) were cut along the interface of the inner and outer layers of onsite-cured CIPP sample to separate the individual layers of onsite-cured CIPP. The specimens were polished to create smooth surfaces and were kept dry in an oven at 50 °C for 24 hours and were cooled to room temperature in a desiccator. The weight and dimension of the dry specimens were measured and recorded. The dried specimens were then immersed in distilled water and kept in an oven at 40 °C. The specimens were removed from the water periodically (at 24, 48, 72, 84, 96, 120, 144 hours) and wiped with filter paper to remove surface water. The sample was immediately weighed with a digital scale and the dimensions were measured with calipers. After measurement, the specimens were re-immersed in water and kept in the oven. The weight gain was measured using the following equation:

$$W (\%) = \frac{w(t) - w(0)}{w(0)} \times 100 \quad (2.1)$$

where $w(t)$ and $w(0)$ are the weight of the CIPP specimen at time t and before immersion, respectively.

2.2.9 Thickness measurement

The images of multiple location of onsite-cured liner was taken using an AmScope stereo microscope and the AmScope image capture software. The inner and outer layer thickness was measured by ImageJ software. At least sixty measurement was taken, and the average value was determined. Two unpaired independent samples t-test was performed to compare results with a probability (P value) of 0.05.

2.2.10 Porosity measurement

Onsite-cured CIPP samples (inner and outer layers) were further investigated to study the porosity of conditioned specimens using optical microscopy and compared with as-received CIPP specimens. Samples were imaged in multiple locations using an AmScope stereo microscope and the AmScope image capture software. At least twenty images were taken for each specimen. The selection tool in Adobe Photoshop was used to outline and select the pore regions in each image. ImageJ was used to apply a threshold to the copied pore-only images, distinguishing the pores

from the non-porous regions. Using the “analyze particles” feature in ImageJ, percent area (percent porosity) was calculated for each sample image. The average of the percent areas was used to determine the percent porosity of the sample [Appendix A, Figure A-2]. Two unpaired independent samples t-test was performed to compare the porosity of non-conditioned and water-conditioned specimens with a probability (p value) of 0.05.

2.2.11 Density measurement

The density of the inner and outer layers of the onsite-cured CIPP was measured according to ASTM D792-00, before and after the absorption and immersion tests. The samples were weighed in air and during submersion in water. Proper caution was taken so that no air bubbles were present on the sample surface during submersion in water. Two unpaired independent samples t-test was performed to compare the density of non-conditioned and water-conditioned specimens with a probability (p value) of 0.05.

2.2.12 Flexural testing

Flexural tests were performed of curved samples excised from the cylindrical pipe. Though the samples were curved, every attempt was made to follow the modified ASTM D790-17 standard for flexural testing of composite samples [33]. Samples of the material both before and after immersion in water were tested. The apparent flexural strength and modulus of the composite were determined using the three-point bending test method using an MTS 810 instrument (MTS Systems Corporation, MN, USA) with a 22 Kip load cell. Note that because of the gross curvature and local thickness variations in each sample, only an apparent flexural strength and modulus can be calculated. These are not to be interpreted as the true values of strength or modulus, as the stress state in the specimen was not actually determined, for the aforementioned reasons. However, these apparent values give an approximate means to compare the effects of immersion on the mechanical properties of the material. There was no significant change in sample dimensions for the mechanical testing for immersed and neat samples as all exposed samples were dried for 48 hours prior to testing. The tests were conducted using the displacement control mode with a crosshead speed of 1 mm/min. The nominal sample size was 100 mm (length) \times 12 mm (width) \times 7.5 mm (thickness). The span length to thickness ratio of 10:1 was maintained, thus the span was adjusted

accordingly based on the directly measured thickness for each sample, with a nominal span length of 75 mm. Seven non-conditioned samples and six water conditioned samples were tested at 23 °C and 50% humidity. The average value of flexural modulus and strength were taken and two unpaired independent samples t-test was performed to compare the mechanical properties of non-conditioned and water-conditioned specimens with a probability (p value) of 0.05.

2.2.13 Fracture surface analysis

The fracture surfaces of the conditioned and non-conditioned samples were investigated using an AmScope stereo microscope (Irvine CA) and the AmScope image capture software. In addition, a Phenom ProX desktop SEM (PHENOM WORLD, Netherlands) was also used to obtain images of the fracture surface of the specimens.

2.3 Results and Discussion

2.3.1 Physical and mechanical properties of the exhumed CIPP

Visual differences in the CIPP inner and outer layer led the authors to investigate each individual layer. The newly created CIPP removed from the field (onsite-cured) consisted of two resin-impregnated PET felt layers (Figure 2.1). Notably, the CIPP thickness and the physical properties differed between the CIPP's inner and outer layer (Figure 2.2). The thickness of inner and outer layers are 2.65 mm and 5.26 mm, respectively. Porosity of the inner layer (3.4 %) was less than that of outer layer (8.1 %). Interestingly, the CIPP bulk densities were not different. Allouche reported the density and porosity of five different installations sites in Denver, Colorado and Columbus, Ohio [34]. The range of density and porosity of CIPPs of those sites were 1.0731-1.174 and 8.16-17.75 %, respectively.

During steam curing, there is likely a temperature difference between the inner layer (in contact with steam) and the outer layer (in contact with the cold host pipe) as depicted in Figure 2.1 [35]. Therefore, the outer layer of the CIPP liner likely experienced a slower temperature increase than the inner layer because resin saturated fiber felts have low thermal conductivity. The complete consolidation of the outer layer could not be achieved prior to the resin viscosity rising beyond the processable range, which resulted in a non-uniform and poor consolidation region in

the outer layer of the liner [35]. Thus, the thickness of the outer layer is higher than that of the inner layer because of this consolidation effect.

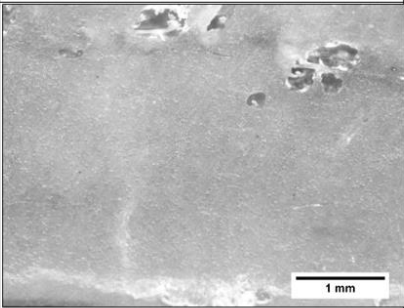
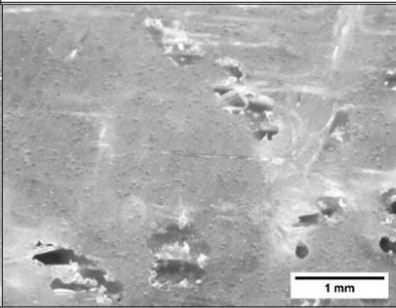
Properties	Inner Layer	Outer Layer
Surface Morphology		
Porosity, %	3.41 ± 0.89	8.07 ± 1.32
Density, g/cm ³	1.24 ± 0.02	1.23 ± 0.01
Thickness, mm	2.65 ± 0.05	5.26 ± 0.09

Figure 2.2 Physical properties of the inner and outer layers of the exhumed CIPP.

Porosity can be formed due to entrapped air during resin impregnation, the insertion of impregnated uncured resin liner into the culvert, and the liberation of volatiles formed during the curing cycle. The observed porosity difference between the inner and outer layer may have been caused by several phenomena. During CIPP manufacture, high pressure steam was applied to expand the liner, and this pressure may have forced entrapped air bubbles towards the edge of the CIPP. In addition, the porosity of the inner layer of the CIPP is smaller and spherical in shape, while large cylindrical pores were observed at the CIPP edges. The consolidation pressure (curing pressure) may vary across the thickness of the fiber reinforced composite laminate [35,36]. The consolidation pressure was applied from the inner layer during steam curing, and then the pressure was distributed across the thickness of the liners. When consolidation pressure was applied from the inner layer (comparatively high-pressure region), resin started to flow towards the edge of the liner (low pressure region). The voids (formed due to entrapped air or volatiles) may have migrated from the inner layer to the edge and coalesced to form large cylindrical pores. Liu and Chen reported that voids were small and spherical at a higher pressure while larger and elongated voids could be observed in lower pressure regions [37]. Another explanation of this behavior could be that the CIPP reached a cured state or sufficiently high viscosity prior to entrapped air or porosity

completely diffusing out of the CIPP, leaving large regions of porosity near the edge. Rubin and Jerina reported that insufficient curing pressure would form porosity in a composite laminate [38].

Mechanical properties could only be measured for the entire exhumed CIPP sample, not the individual layers. The flexural strength and modulus of the exhumed CIPP were 43.25 ± 2.13 MPa and $1,437 \pm 93.99$ MPa, respectively. Minimum standards for the flexural strength and flexural modulus of the approved polyester-saturated felt CIPP liners are 31 MPa and 1,720 MPa, respectively according to contractor records [33] and in some cases meeting a minimum mechanical performance threshold is used to determine if a CIPP installation has been “fully-cured”. The types of resin (polyester or vinyl ester), reinforcing materials (flexible felts or equivalent woven or non-woven materials) and most importantly, the curing condition (pressure and temperature) play a vital role to control the mechanical strength of the cured CIPP liners. The minimum and maximum flexural strength and flexural modulus of CIPP reported in the literature are 34.7-50.1 MPa and 1,259-3,379 MPa, respectively [34]. As we could not separate the two layers, it is unknown whether the extra porosity in the outer layer weakened it or the final composite, although this cannot be discounted.

2.3.2 Thermal Behavior: Exhumed CIPPs vs. Oven Cured CIPP Material

Calorimetry and thermogravimetry measurements identified differences between the uncured resin tube, inner and outer layers of onsite-cured CIPP, and oven cured CIPP material (Figure 2.3). The uncured resin shows a pronounced exotherm between 80 °C and 120 °C with a maximum peak temperature around 100 °C due to the thermal curing of the resin. In both the first and second heating scan of the uncured resin tube, two endothermic peaks were observed at around 120 °C and 160 °C, indicating the melting temperature (T_m) of polyethylene/polypropylene bilayer coating [Appendix A, Figure A-3]. In contrast, the onsite cured CIPP exhibited much different thermal behavior, even compared to the inner and outer layers. Neither the first or second heating scan revealed the presence of an exothermic response associated with curing, indicating no residual reactivity and that the resin was essentially “fully cured”. Both inner and outer layers had small endotherms between 25 °C and 120 °C on the first heating scan only, which may be indicative of volatilization. This lack of an endotherm on the second scan indicates that lack of detectable amount of volatile contents. Oven-cured CIPPs exhibited very similar thermal characteristics to onsite-cured CIPP, even though oven cured CIPP was not exposed to pressurized steam. Like

onsite-cured CIPP, an endotherm was detected for the first heating scan, but not the second scan, and the thermoplastic bilayer coating melting response was also found.

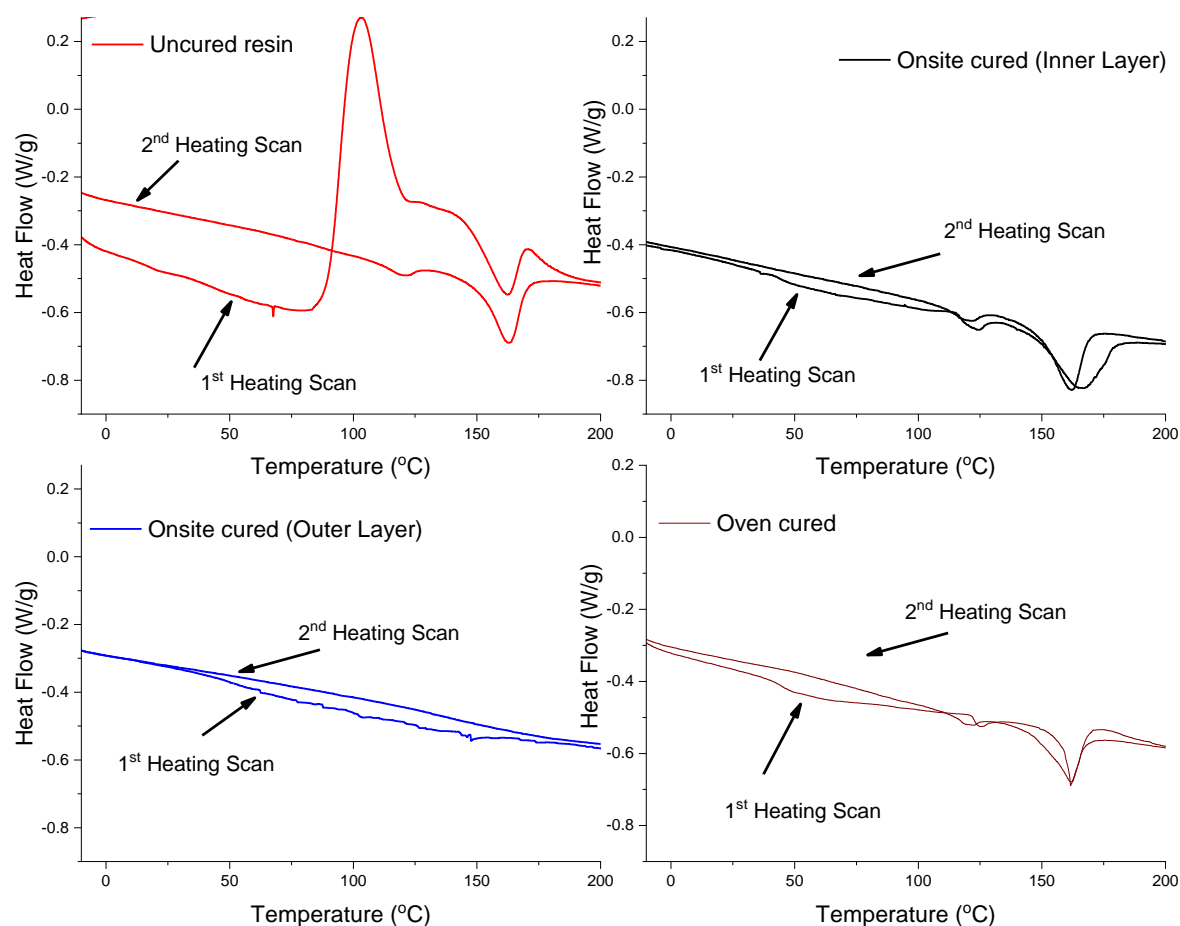


Figure 2.3 DSC thermograms of uncured resin liner, inner layer of the onsite-cured CIPP, outer layer of the onsite-cured CIPP, and oven-cured CIPP liners. DSC performed in nitrogen atmosphere showing the heating portion of heat-cool-heat scan for each sample.

Thermogravimetric analysis was applied using air and nitrogen atmospheres to further examine the thermal behavior of the uncured resin tube, onsite-cured CIPP (inner, middle and outer layers), and oven-cured resin tube (Figures 2.4 and 2.5, Table 2.1). The initial weight loss around 120 °C and was due to the evaporation of the residual volatile compounds, water and unreacted styrene. Since the boiling point of styrene is around 145 °C, the residual entrapped and unreacted styrene evaporated by around 160 °C [39]. As expected, the uncured resin tube contained the most volatile material (7.73 and 9.16 % at 120 and 160 °C, respectively). Interestingly, the oven-cured CIPP liner exhibited substantially less weight loss than onsite-cured CIPP samples,

indicating that the onsite-cured samples may not have the same level of process optimization which can be met under laboratory conditions. Furthermore, the volatile and styrene contents of the outer layer (0.53 and 1.63 %) of onsite-cured CIPP were higher than in the inner layer (0.40 and 0.80 %). During installation, the air pressure may have induced most of the residual volatiles and unreacted active styrene monomers to migrate from the inner layer to the outer layer. These volatile compounds entrapped in outer layer because of curing of the resin tube. Another possible explanation could be that the inner layer has a higher/longer temperature and so is more fully cured which reduced the volatile content. The absence of prior studies that examined CIPPs at this detail inhibited a more fundamental explanation of the factors that influenced result.

The uncured resin tube exhibited a first major decomposition temperature (373.6 °C) due to the decomposition of the unsaturated polyester crosslinked structure. The second decomposition temperature represented PET felt as the raw felt had a 436 °C decomposition temperature [Appendix A, Figure A.4]. The observed uncured resin tube decomposition temperature was different from raw felt (436 °C) because decomposition of the crosslinked resin and coating materials are all considered in the complex thermogram. Both oven-cured and onsite-cured CIPP liners exhibited similar decomposition behavior trends. For onsite-cured CIPP liners, the inner layer's thermal decomposition behavior is comparable to the outer layer, however, as shown in Figure 4, the inner layer shows two more decomposition events (around 323 °C) just before the 1st major decomposition. These two decompositions were caused by the decomposition of the PE/PP bilayer coating [Appendix, Figure A.4].

The third decomposition peak around 530 °C denoted the burn off for the carbon residue, which remained after the first and second decomposition temperatures. Mass remaining at 900 °C represented inorganic fillers (likely fumed silica according to the contractor's SDS) [32]. The PET felt with a PE/PP bilayer coating showed only 1-2% residue [Appendix, Figure A.4]. This result further confirms that some inorganic material originated from the resin itself. Interestingly, the outer layer contained the greatest amount of residue (26.4 %). One hypothesis could be that when high pressure steam was blown inside the CIPP, fumed silica may have been pushed towards the outer layer. Another possibility is that the inner layer sample collected for TGA analysis contained coating layer which yield lower residue coating whereas the outer layer sample only consisted of felt and resin. Independent compositional analysis of CIPP resins and uncured resin tubes were not found in the literature for comparison.

Table 2.1 Thermal behavior of uncured, onsite-cured, and oven-cured CIPP liners.

Sample	Weight loss at 120 °C (%)	Weight loss at 160 °C (%)	1st step Decomposition Temp (°C)	2nd step Decomposition Temp (°C)	3rd step Decomposition Temp (°C)	Residue Content at 900 °C (%)
Uncured liner	7.73±0.18	9.16±0.33	373.6 ± 0.8	412.44 ± 0.30	528.30±0.56	24.74±0.75
Oven-cured liner	0.42±0.11	1.41±0.29	381.8 ± 0.48	410.21 ± 2.52	532.29±0.51	25.44±0.82
Onsite-cured (Inner layer)	0.47±0.03	0.80±0.06	379.95 ± 0.47	403.11 ± 8.51	528.83±3.78	15.95±1.27
Onsite-cured (Outer Layer)	0.53±0.03	1.63±0.21	381.84±.48	420.6 ± 0.48	530.25±1.42	26.40±.82

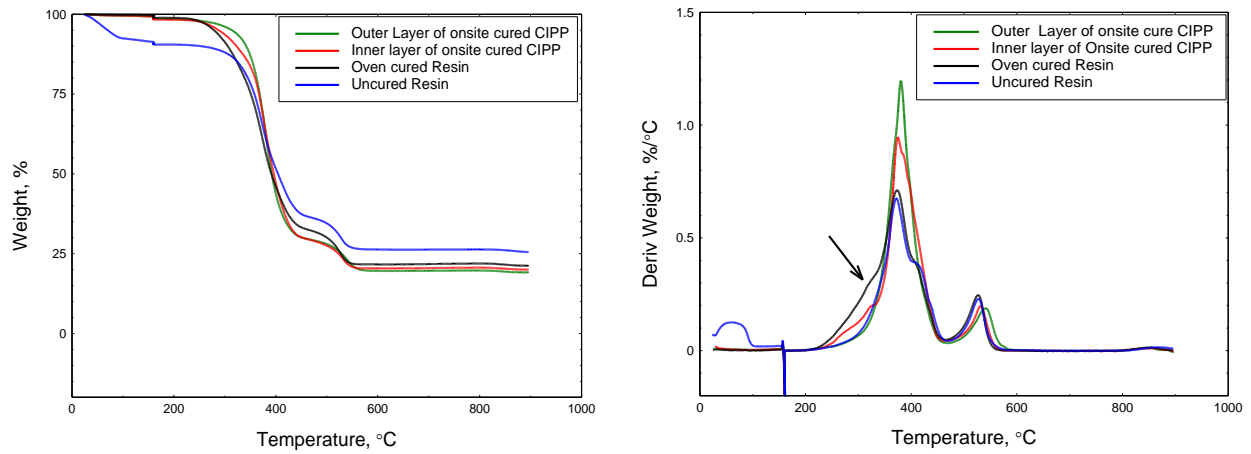


Figure 2.4 (a) Thermogravimetric (TG) and (b) Derivative thermogravimetric (DTG) curves of uncured, onsite-cured, and oven-cured CIPP liners.

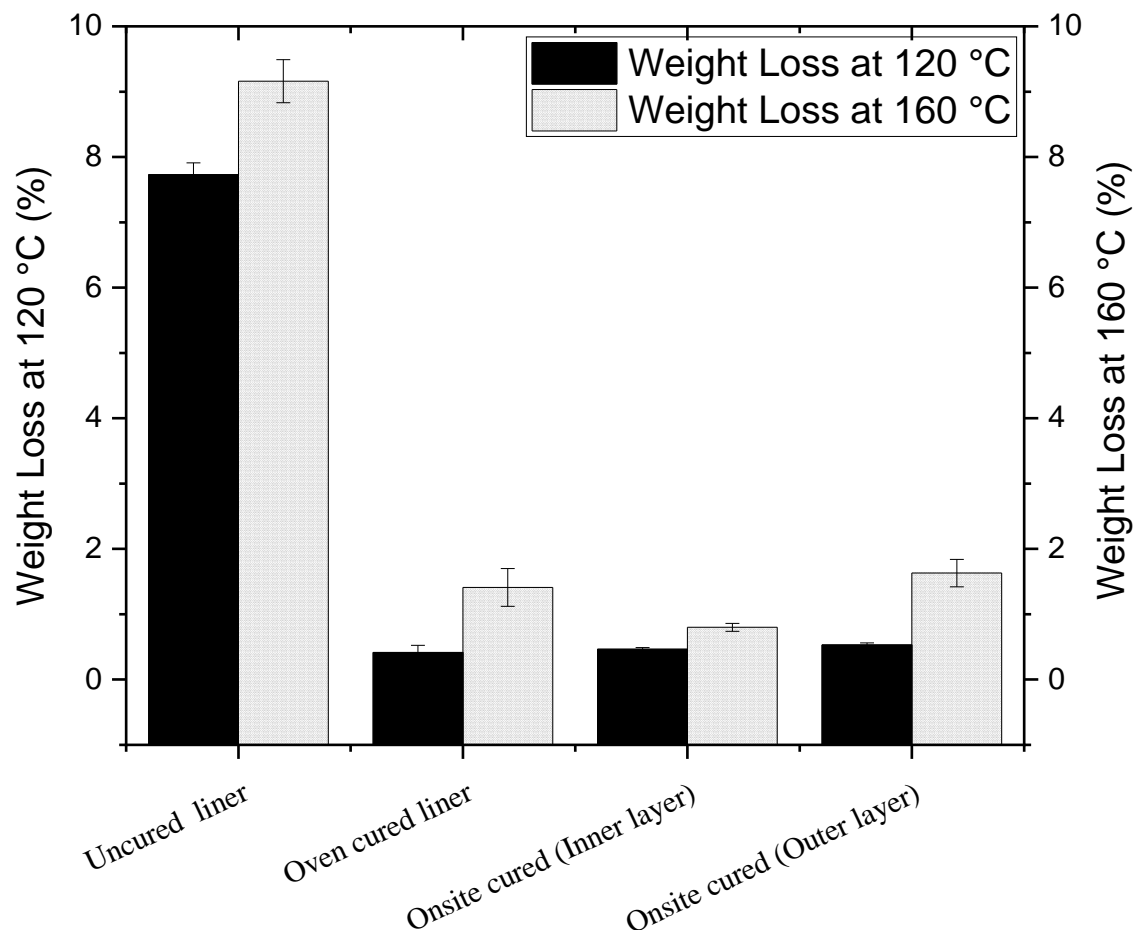


Figure 2.5 TGA weight loss of uncured, onsite-cured, and oven-cured CIPP liners at 120 °C and 160 °C.

2.3.3 Chemical analysis of leaching organic compounds

NMR analysis of the uncured resin tube revealed the presence of styrene as well as other compounds (Table 2.2, Figure A.5). Styrene was detected by the presence of peaks around 5.25, 5.76, 6.72, 7.33, and 7.41 ppm, and was used with the isophthalic-based, polyester resin-saturated PET felt liner. Other major compounds detected were benzaldehyde, phenol, and 1-tetradecanol. Benzaldehyde is a known oxidation product of styrene [40]. Resin initiators are thermally unstable and undergo self-decomposition to form decomposition products, such as 1-tetradecanol [41], while phenol may be a contaminant of the unsaturated polyester resin. These compounds likely volatilized from samples during TGA measurement.

An important observation of this study was that styrene dimers and trimers may be present in onsite-cured CIPPs (Table 2.2). Complicating analysis and interpretation of NMR results was

that limited information was found regarding the chemical NMR and library data for the styrene dimers and trimers. Evidence suggests that styrene undergoes free radical polymerization to form styrene dimers and trimers during curing temperatures and pressures in the presence of initiator [Appendix A, Figure A.6]. Steam can catalyze oligomerization reactions and a prior CIPP study reported that, during steam injection, water vapor can diffuse through uncured resin tubes to the liner's outer surface [Appendix A, Figure A.8]. Several potential styrene oxidation products were also found in the onsite-cured CIPP [42]. They included styrene oxide, benzaldehyde, benzoic acid, and 2-phenyl acetaldehyde [Appendix A, Figure A.7] [40].

GC-MS analysis results support NMR results and confirmed the presence of styrene, benzaldehyde, and 1-tetradecanol in the uncured resin tube. Onsite-cured CIPP samples also contained those three compounds but at much lower loadings [Appendix A, Table-A.1] The findings of this study suggested that the steam/water curing process may have leached significant amounts of benzaldehyde, 1-tetradecanol, and benzoic acid from the CIPP liners. Phenol and benzoic acid were also detected in the onsite-cured CIPP. For oven-cured CIPP, all chemicals were detected by NMR except benzaldehyde.

Interestingly, no styrene dimer or trimer compounds were detected for oven cured CIPPs but were detected for onsite-cured materials. This finding indicates that onsite-curing conditions may influence the styrene oligomerization process, and therefore the leachates and extractives of the CIPP. As these organic molecules may diffuse into the water flowing through the installed CIPP pipe and that hydrophobic polymers have moderate barrier properties towards organic molecules (permeability of small organic molecules depends upon the chemical structure of the permeant molecules) [43], research should investigate the effects of pressurized hot steam on styrene oligomerization and their transport behavior.

Table 2.2 Organic molecules detected from ¹H-NMR spectra and GC-MS of leachate solutions of CIPP liners^a.

Compounds	1H-NMR Analysis					GC-MS Analysis		
	Detected Regions ppm	uncured	Onsite-cured		Oven-cured	uncured	Onsite-cured	Oven-cured
			inner surface	Outer surface				
Styrene	5.25, 5.76, 6.72, 7.33, 7.41	Yes	Yes	Yes	Yes	Yes	Yes	Yes
2,4-diphenyl-1-butene (styrene dimer)	2.29,2.56,4.96,5.33,6.83,7.14, 7.19,7.22,7.28	No	Yes	Yes	No	No	No	No
1,2-diphenylcyclobutane (Styrene dimer)	1.81,2.06,3.61, 7.19,7.28	No	Yes	No	No	No	No	No
2,4,6-triphenyl-1-hexane (styrene trimer)	1.89,2.11,2.36,2.53,2.71, 4.96,5.33, 6.83,7.14,7.19, 7.22,7.24	No	Yes	Yes	No	No	No	No
1,3,5-triphenylcyclohexane (styrene trimer)	1.9,2.15,2.72,7.19,7.21,7.32	No	Yes	No	No	No	No	No
2-phenyl acetaldehyde (Minor Oxidation product of styrene)	10.03, 7.22,7.24,7.27,3.66	No	Yes	Yes	No	No	No	No
Benzaldehyde	7.53, 7.63, 7.88, 10.03	Yes	Yes	Yes	No	Yes	Yes	Yes
Phenol	8.7, 7.24,6.84,6.93	Yes	Yes	No	Yes	No	Yes	Yes
1-Tetradecanol	0.88, 1.26, 1.43,1.58,3.62, 4.7	Yes	Yes	Yes	Yes	Yes	Yes	Yes
Benzoic acid	7.48,7.81,8.13,12.71	No	No	No	No	No	Yes	Yes

^a CDCl₃ and DCM solvents were used for ¹H-NMR spectra and GC-MS analysis, respectively. "Yes" represents the presence of the depicted organic molecules in leaching solution.

2.3.4 Interaction of Water with CIPP Specimens

The swelling of the onsite-cured CIPP samples was investigated to examine the effect of water conditioning on the change of physical and mechanical properties (Figures 2.6). Water immersion results describe the Fickian behavior for CIPP's outer layer. In contrast, non-Fickian behavior was observed for the CIPP's inner layer. This difference is likely due to the coating layer delamination after 48 hours of immersion (Figure 2.7). Delamination likely introduced additional sorption sites which enabled further weight gain. The higher water sorption (3.8% wt) found in the outer layer compared to the inner layer (3.1% wt) was likely due to the outer layer's higher available porosity. The enhanced porosity of outer layer increases the possibility of having more sorption sites and suitable diffusion paths. Furthermore, the authors assumed that the sorption process achieved saturation within 7 days. No decrease in weight was observed during water immersion experiments.

Swelling curves indicated that initially the sample thickness swelled dramatically and reached a saturation point (constant value of thickness). Similar to weight gain data, the inner layer exhibited a two-step swelling phenomena after exposing to water which further indicate delamination of the coating layer. There was no observed difference in the swelling behavior of the inner and outer layers of CIPP once the material had reached swelling equilibrium.

Microscopy results revealed that the initiation of coating layer debonding was observed after samples were immersed for 7 days (Figure 2.7). This debonding was thought to be caused by swelling (and thus dimensional changes) of the composite. Furthermore, the thermal contraction of the matrix as it cooled down from its curing temperature may introduce residual stress [44]. During conditioning, the composites may swell and generate new residual stresses acting in opposition to the thermal stresses. Part of thermal residual stresses were relieved by the effects of swelling [44]. During conditioning, the swelling effect weakening the thermoplastic coating adhesion although no matrix crack could be observed.

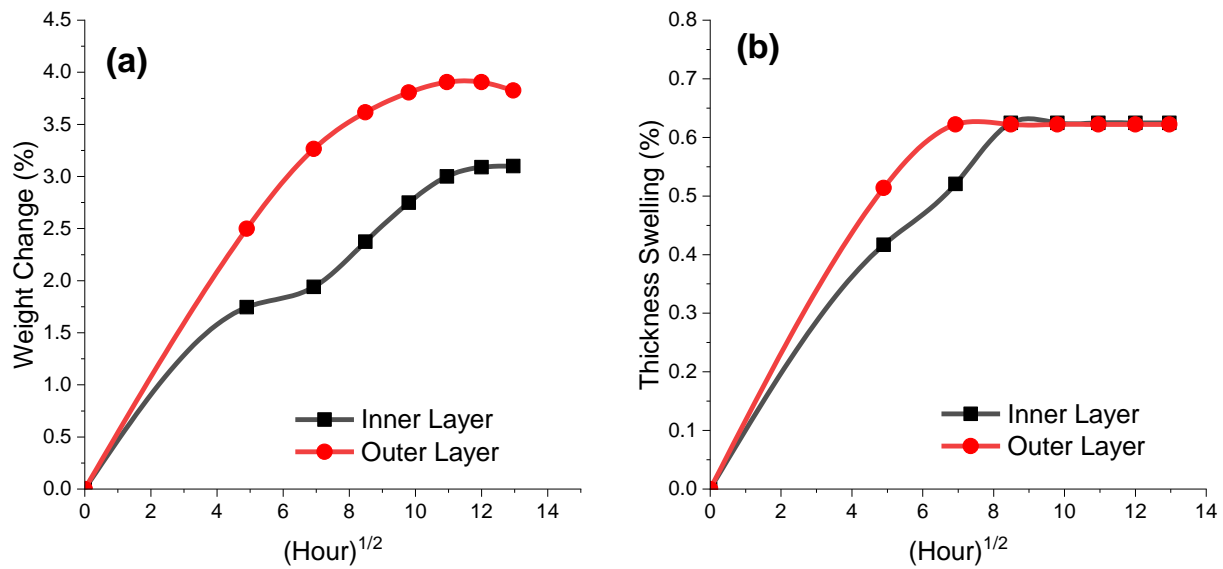


Figure 2.6 Weight (a) and thickness (b) change of inner and outer layers of CIPP as a function of immersion time.

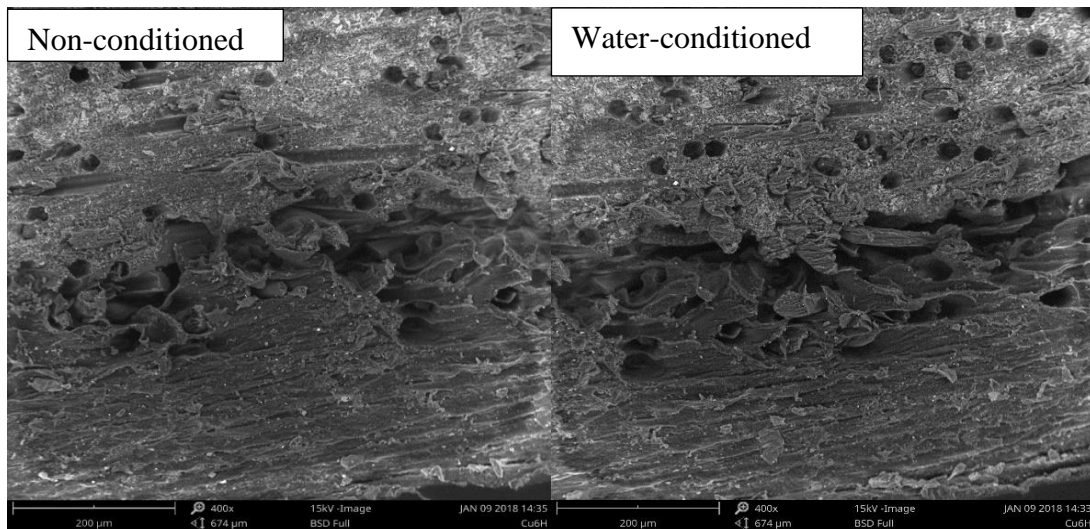


Figure 2.7 Debonding between the coating layer and the composite layer of the CIPP before and after condition.

2.4 The effect of water conditioning on physical and mechanical properties

In Figure 2.8 is shown the density and porosity measurements for the two materials. While no differences were detected for porosity and density for water conditioned oven cured CIPPs, water conditioning altered the mechanical behavior of the specimens as follow. To investigate the effects of conditioning on the mechanical properties of the CIPP, flexural tests were performed. The flexural modulus and strength of the specimens was measured before and after conditioning in water, as shown in Figure 2.9. Ductile behavior was observed in the flexure tests of non-conditioned specimens, while more brittle behavior was seen in the water-conditioned CIPP liners (Appendix A, Figure A.10-A.11). The flexural strength and modulus of the CIPP were 43 ± 2 MPa and $1,400 \pm 100$ MPa, respectively. Surprisingly, after water-conditioning the modulus value increased by 20%, although the difference in strength was statistically insignificant, indicating that, at least in the short term, water exposure (such as during use or during CIPP sample transport to a testing laboratory) may improve the mechanical performance of the CIPP. The non-conditioned samples contain unreacted monomers and other organic molecules which are expected to plasticize and increase the toughness of the composite materials. In contrast, after water conditioning, the synergistic effects of the thermal aging (post curing) and the leaching of the residual organic molecules caused the composite samples to behave like brittle materials.

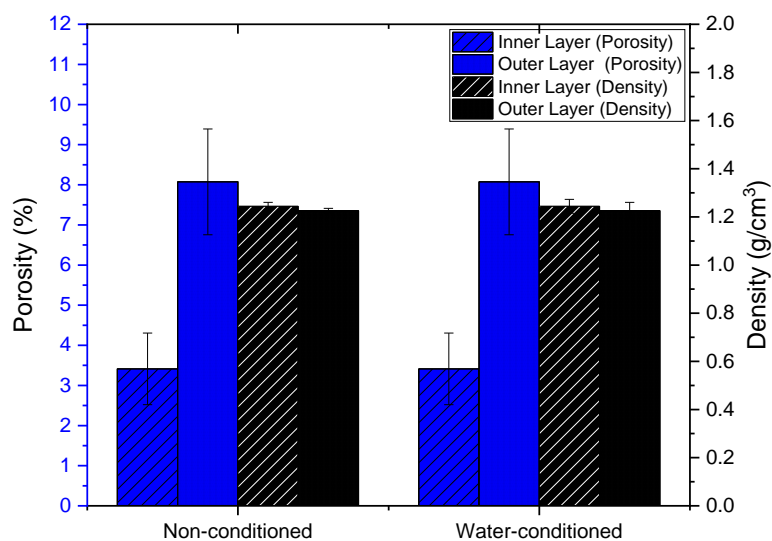


Figure 2.8. Porosity and density of the inner and outer layers of the non-conditioned and water-conditioned CIPP specimens.

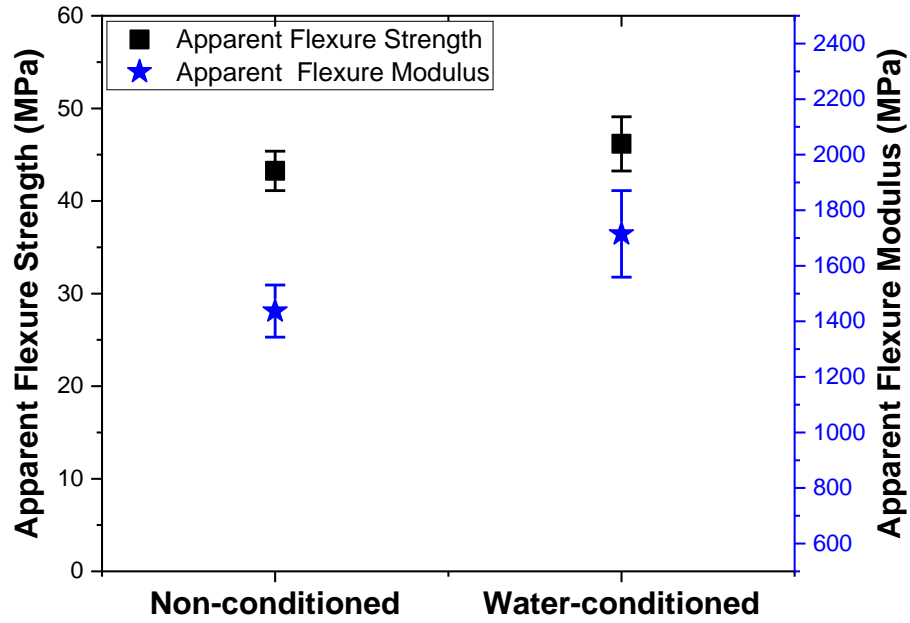


Figure 2.9 Flexural strength and modulus of the CIPP samples before and after conditioning.

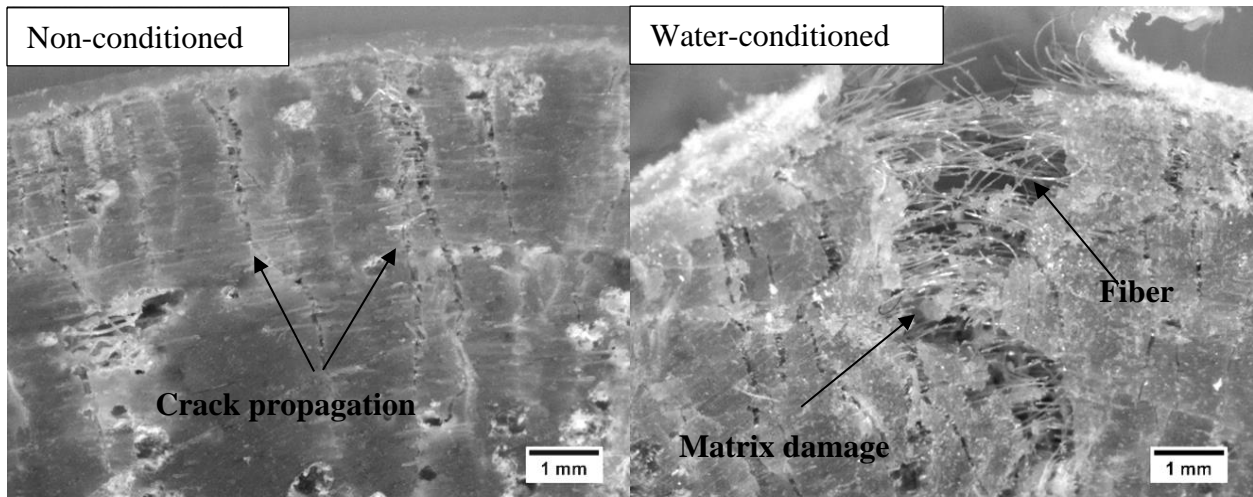


Figure 2.10 Optical microscope images of fracture surface of as-received and conditioned CIPP.

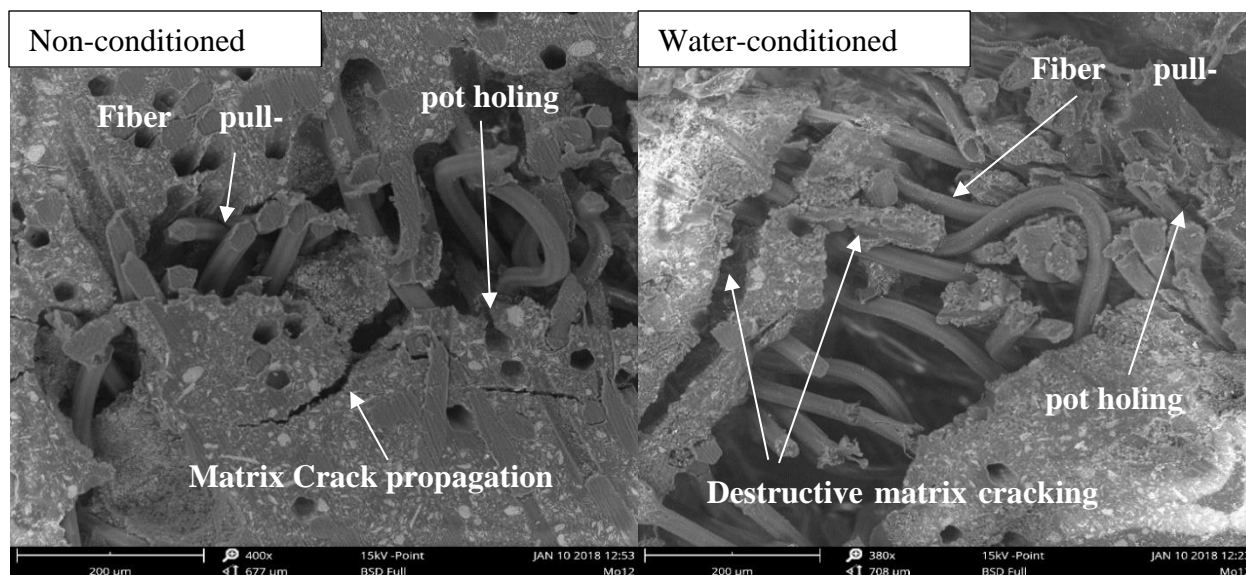


Figure 2.11 SEM images of the fracture surface of non-conditioned, water-conditioned and chloroform-conditioned CIPP specimens.

Fracture surface analysis of the non-conditioned specimens showed toughened behavior of the samples with little crack initiation and no fracture of coating layer (Figure 2.10 and 2.11). In contrast, the water-conditioned specimen exhibited destructive damage with brittle behavior after mechanical testing. This embrittlement was likely due to the removal of compounds (e.g. styrene) that had plasticized the CIPP liner. Furthermore, the mode of failure for both non-conditioned and water-conditioned specimens included matrix cracking, pot holing, and fiber pull-out.

2.5 Summary

The goal of this study was to investigate the CIPP liner in terms of physical properties, presence of unreacted volatile compounds and mechanical properties. The porosity and density of the inner layer differed from the outer layer as the inner layer may have been influenced by higher pressure and temperature during installation. Installation pressure and temperature also likely influenced the presence of unreacted volatile content. Volatiles present in the CIPPs included styrene, its oxidation products, and other possible carcinogens of varying amounts. TG analysis showed that the volatile content, of inner layers was lower than outer layer. Unique to this study was that styrene dimer and trimers were found in the onsite cured CIPP liner but were not detected when the same uncured resin tube was oven cured in the laboratory. The inner and outer layer

exhibited response differently to water conditioning, showing different porosities and uptake. Furthermore, water conditioning did not change strength of the liner significantly, although conditioning did show onset of cracks and debonding indicating that long-term mechanical performance may be compromised to some degree. Additional work is needed to document the characteristics of CIPPs being installed, elucidate the role of the temperature gradient down the length of the liner and through the pipe wall, and sensitivity of final properties to pressure, curing temperature, and exposure duration.

CHAPTER 3. INFLUENCE OF AGGRESSIVE ENVIRONMENTAL AGING ON MECHANICAL AND THERMO-MECHANICAL PROPERTIES OF UV-CURED CIPP LINERS

All research work except GC-MS experiment was performed by Md Nuruddin. All analysis except GC-MS analysis was performed by Md Nuruddin with guidance by Prof. John Howarter and Jeffrey P. Youngblood. All writing was performed by Md Nuruddin with guidance and editing by Prof. John Howarter, Jeffrey P. Youngblood, and Andrew Whelton.

The following chapter contains content reproduced with permission from Md Nuruddin, Kayli DeCocker, Seyedeh Mahboobeh Teimouri Sendesi, Andrew J. Whelton, Jeffrey P. Youngblood, John A. Howarter " Influence of aggressive environmental aging on mechanical and thermo-mechanical properties of Ultra Violet (UV) Cured in Place Pipe liners" Journal of Composite Materials.

3.1 Introduction

Cured-in-place pipe (CIPP) is a popular trenchless technology that was invented in the 1970s to rehabilitate the existing sewer and underground water pipe [45]. This *in-situ* process has gained wide attention in the U.S. because its use can help avoid open-trench excavation and roadway shutdowns. The process involves the insertion of felts (PET or fiber glass) saturated with thermoset resin (unsaturated polyester, vinyl ester or epoxy) into the existing deteriorated pipe. The resin is then polymerized using hot water, hot steam, or UV light [46]. Thermal curing processes (hot water and steam) are the most popular in the U.S. because of their low process cost and lower working time compared to UV light process [46]. However, concerns exist regarding chemical emissions into the environment by thermal curing processes. Teimouri et al. (2017) reported that a multiphase mixture was released during steam CIPP installation that contained carcinogenic styrene vapor, but also degradation products of styrene, other organic volatile organic compounds (VOC), uncured resin, particulates, and water vapor [6]. Ra et al. (2019) found a variety of VOC and semi-volatile organic compounds leaching from new steam-cured CIPP liners in California [8]. Compounds were mainly initiator degradation products (i.e., acetophenone, 4-tert-butylcyclohexanone, 1-tetradecanol, benzoic acid), monomers and oligomers (i.e., styrene, dimers, trimers, and other monomers), an oxidation product (i.e., benzaldehyde) [8,47]. Kobos et al. (2019) found that material discharged during steam-CIPP manufacture can be toxic to human and mouse lung cells [48].

Compared with the thermal CIPP manufacturing process, UV CIPP technology first entered into U.S. in 2007. The practice is reportedly claimed to have faster curing, lower chemical emissions, small carbon footprint, high strength reinforced materials, avoiding usage of hot water or steam, and no requirement for a cool-down phase [7,46,49]. As found by Ra et al. (2018) and Li et al. (2019), chemical leaching into water associated with UV-cured CIPP installation process is still a problem [7,9]. Ra et al. (2018) reported multiple prior studies showing that styrene leached from the UV-cured CIPPs into simulated storm-water that was flushed through the pipes [9]. Most recently, Li et al. (2019) collected the rinse water exiting each CIPP after installation followed by immediate flushing in New York and Virginia installation sites. Results showed that rinse water the styrene and dibutyl phthalate (DBP) levels exceeded state surface water limits[7].

Numerous studies have focused on the air emission and water quality due to leaching of carcinogenic styrene and other organic volatiles of the nearby area during CIPP installation [6–9,50]. Cured-in-place pipe is used for rehabilitation of underground or stormwater pipes, but a lack of knowledge of hygrothermal degradation mechanisms, durability of the material and potential property changes due to aging creates a challenge for long time usage. Few of the reported studies have dealt with the mechanical and physical properties of CIPP liners [51–55] but long term durability was not a focus. Nuruddin et al. (2019) investigated the physical and mechanical properties of steam cured CIPP liners after short time exposure to water for 7 days at 40°C[56]. They reported that the physical properties (porosity and density) were not influenced by water aging although flexure modulus was increased significantly because of leaching unreacted styrene and other volatiles compounds.

UV-cured CIPP liners made of fiber glass/PET felts reinforced polyester resin. Thus the mechanical and thermal properties of both polymer resin and reinforcing fibers can be degraded significantly after exposure to aqueous and aggressive environment especially salt and alkaline solutions [57–61]. When exposed to a humid environment, the transportation (sorption and diffusion) of water molecules into the molecular structure swells the matrix, and generating internal stresses that can crack and fail the resin [62]. Furthermore, the polymer matrix can undergo chain scission triggered by hydrolysis, and low molecular weight material leaching from the bulk resin could further degrade the matrix [63]. Thus, changes in the resin can be classified as reversible (plasticization and swelling) or as irreversible (hydrolysis, dissolution, and microcracking) [64]. These reversible and irreversible process causes microstructural defects, and

subsequently weakening the interfacial strength of fiber reinforced composite. On the other hand, glass fibers undergo corrosion induced damage due to the interaction of moisture with the metal oxides and thus results in reduced mechanical strength [65].

CIPP can be exposed to sea salts in hot-humid climates or marine environment, deicing salts in cold climates, and many other severe environments. Because CIPP liners are installed for damaged concrete sewerage pipe rehabilitation, CIPP may be exposed to concrete pore solution having pH values ranging from 12.4 to 13.7 [65]. Thus, the presence of elevated temperature, alkali, and salt in humid environment have synergistic effect on degradation mechanism of both polymer and fibers. The elevated temperature during aging of composites could play an important role in the degradation process of composite materials. Ray reported that at the same level of absorbed moisture, interlaminar shear strength of composite is decreased with increasing conditioning temperature [66]. High temperature imposes polymer chain scission, thermo-oxidation or lead to polymer post-curing. Salt molecules accelerate degradation mechanism by hydrolysis and scission of the chemical bonds. Moreover, salt crystals inhibit the moisture diffusion by blocking the paths through which water diffuses into the material. Furthermore, the alkaline environment damages glass fibers severely by chemical attack which reduces the toughness and strength of the fibers [67].

In this study, the mechanical and thermo-mechanical performance of newly manufactured CIPP liners from two different storm sewer installation sites were investigated. Characterization of volatile material inside the new CIPPs and residual curing were conducted. Furthermore, the samples were exposed to distilled water, saltwater and concrete pore solution to investigate the combined effect of temperature, humidity, saltwater and alkaline environment on the interlaminar shear strength and viscoelastic properties of CIPP liners.

3.2 Materials and Experiment

3.2.1 Materials

All the materials examined in this study were obtained from two installation sites of a CIPP storm-water culvert liner, in Syracuse, NY (Figure 3.1). The contractor for both sites used a SAERTEX®-S-LINER. This liner composition was reported in Li et al (2019) [7]. The main liner material contained two layers of unidirectional stitch-bonded fiber glass (comprises 45% of the

total liner weight) and vinyl ester resin, and a thin layer of PET fleece. The liner was covered by multiple layers of foils. During installation, the inside of the liner was protected by a laminated foil (PA/PE). This foil was removed after installation. There were two outside foils, one preventing the escape of styrene and resin, and the second providing protection against UV light and any damages while handling the liner [68].

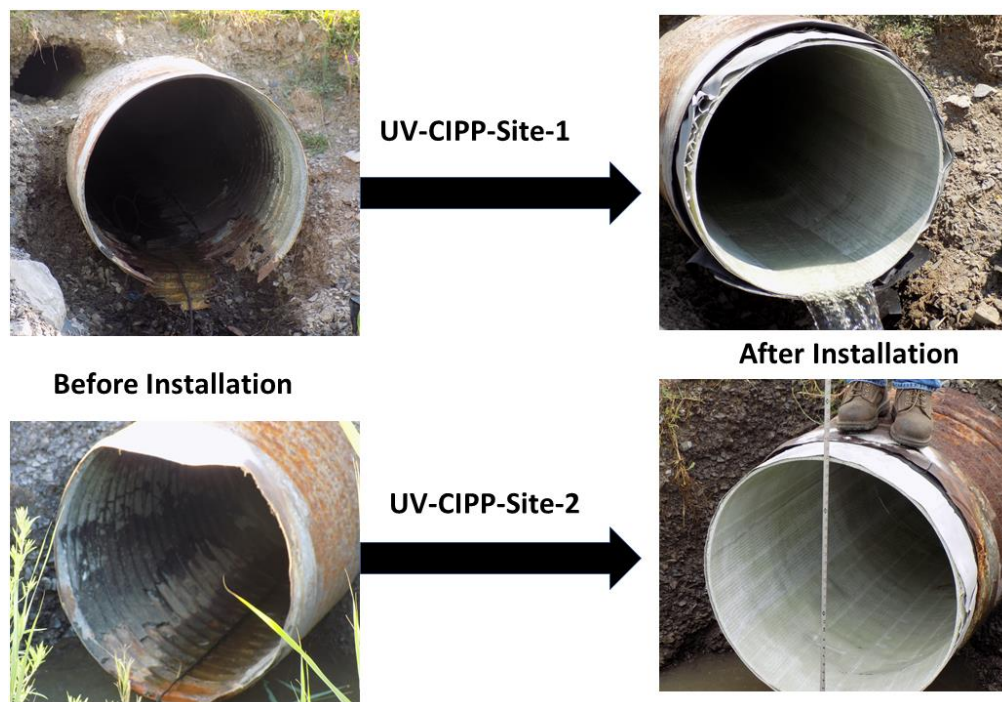


Figure 3.1 UV-cured CIPP liners.

The material SDS provided by CIPP contractor, indicated the resin used was ATLAC[®] E-Nova RE 3475. The composition of the resin included 35-50% styrene, 0.1-25% phenyl bis(2,4,6-trimethylbenzoyl)-phosphine oxide (Irgacure[®] 819), less than 0.25% 2,2-dimethoxy-1,2-diphenylethan-1-one (Irgacure[®] 651) [69]. The resin MSDS also indicated that it was an epoxy bisphenol A vinyl ester urethane especially modified for thickening with magnesium oxide, dissolved in styrene [70]. A 4×1000 W light bulb UV light train was used for the curing process. The wavelengths of highest intensity were between 400 and 450 nm.

The CIPP liners from NY were installed in corroded corrugated metal pipes. These pipes were pre-cleaned by contractors prior to installation. For both sites, standing water existed at both

culvert inlet and/or outlet locations. Liners from site-1 and site-2 were installed on August 8-10, 2017, both having a diameter of 61.0 cm and length of 30.5 m. Once the CIPP liner was manufactured and the ends were cut off, wall thickness was measured at culvert inlet using a tape measure.

The authors were present onsite during setup, CIPP manufacture, and cleanup. The authors collected uncured resin tube samples from the contactors, who also cut samples from the end of the newly installed CIPP liner (7-8 mm thickness) using a razorblade. The cured and uncured samples were immediately covered with black bag and stored in a cooler separately with dry ice during shipment. Once at the author's laboratory, the sample was stored in a freezer at -20 °C until analysis was performed.

For wet chemistry, solid liquid extraction experiments and gas chromatography-mass spectrometry (GC-MS) analysis, the following analytical standards were purchased from Sigma Aldrich, Inc.: Calcium Hydroxide ($\geq 96\%$, 2.24 g/mL), sodium hydroxide ($\geq 97\%$, ACS reagent), Calcium sulfate (4 mesh particle size), potassium hydroxide (2.04 g/cm³), styrene $\geq 99\%$ that contained 4-*tert*-butylcatechol as stabilizer (CAS# 100-42-5). Styrene was confirmed and quantified in the solutions because it was the most abundant and consistently detected compound. Other contaminants leached from the composites at lesser levels, were only detected in some replicate aging solutions, and were not quantified.

3.2.2 Differential scanning calorimetry (DSC)

Curing behavior and thermal analysis was conducted for CIPP liners. A Q-2000 differential scanning calorimetry (DSC) was applied (TA Instruments, Inc., Delaware, USA). Approximately 10 mg samples were added to aluminum sealed pans for testing. Heat-cool-heat cycle scans were performed at a ramp rate of 20 °C/min from -25 °C to 200 °C in nitrogen environment. Heating and cooling curves were examined to understand residual curing behavior and emission of volatile compounds.

3.2.3 Thermogravimetric analysis (TGA)

The thermal stability and volatile content of CIPP liners was determined using a Q-500 thermogravimetric analyzer (TGA) (TA Instruments, Inc., Delaware, USA). A sample weight of

10 to 15 mg was used for testing. A gas purge rate of 60 mL/min was used. Samples were heated to 160 °C at a rate of 10 °C/min in nitrogen atmosphere. The volatilization of organic compounds and evaporation of styrene was examined by holding samples at 160 °C for 120 min. Samples were then headed to 900 °C at a rate of 10 °C/min to determine the composite degradation behavior. This approach was previously applied by Li et al. and Ra et al. for CIPP specimens exhumed from the field [7,8].

3.2.4 Aging solution and experiments

A salt solution and a concrete pore solution were prepared for the CIPP exposure experiments. Deionized water (>18.0 MOhm-cm) was obtained from a Barnstead™ system. A 10% NaCl salt solution was made by dissolving 100 gm of NaCl in 900 mg of water. The simulated concrete pore solution with a pH of 13.5, was made by dissolving analytical grade 0.1 M calcium hydroxide (Ca(OH)₂), 0.1 M sodium hydroxide (NaOH), 0.2 M potassium hydroxide (KOH) and 0.003 M calcium sulfate (CaSO₄), according to Ghords et al. [71].

3.2.5 Absorption and swelling tests

Three CIPP liner samples from site-1 and site-2 were cut using a water jet cutter into squares of 10 mm wide by 10 mm long. These cut samples were then polished to smooth the cut surfaces. Samples were then kept dry at room temperature for 48 hr, which were then weighed. Three specimens from each site were immersed in distilled water, a salt solution, or a pore solution. These solutions were stored in a 50 °C oven for the duration of the experiment. The specimens were removed from the aging solutions periodically (at 24, 48, 72, 84, 96, 120, 144, 168, 192, 216, 240, 264, 288, 312, 336 hr) and wiped with Kim wipes to remove surface water. The dry specimens were immediately weighed and then returned to the solutions. Weight gain was calculated using the following equation:

$$W (\%) = \frac{w(t) - w(0)}{w(0)} \times 100 \quad (3.1)$$

where $w(t)$ and $w(0)$ are the weight of the CIPP specimen at time t and before immersion, respectively.

3.2.6 Energy dispersive spectroscopy (EDS)

Energy dispersive spectroscopy (EDS) was applied to determine what metal ions were ingresses into the interior of the liners from the solutions. After 15 days of the absorption and swelling test, the specimens were sampled by cutting sections across the plys, and EDS analysis was performed within 150 μm of the exposed end using Hitachi S-4800 cold-cathode field-emission scanning electron microscope (FE-SEM) to determine the existence of any penetrated metal ions.

3.2.7 Accelerated aging of onsite-cured CIPP samples

CIPP liners from the field were prepared for viscoelastic and inter-laminar shear strength (ILSS) investigation by first cutting with a water jet cutter. Cut samples were polished starting with 320 grid sandpaper and increasing grit until reaching 2000 grit sandpaper. Ten samples were prepared for ILSS testing and four samples prepared for viscoelastic measurements. After polishing, all samples were immersed in solutions in individual 1000 mL glass bottles with PTFE-lined caps. Immersed samples were kept in an oven at 50 °C for 15 days according to ASTM D543-14 standard [72]. At the end of their aging period, samples were then taken out of the solutions and kept at 23 °C and 50% relative humidity for 48 hr, following standard ASTM D618-13 [73]. The dry specimens were tested to investigate the irreversible change in mechanical and viscoelastic properties of the CIPP liners.

3.2.8 Headspace gas chromatography-mass spectroscopy (HS GC-MS)

At the end of aging period, the solution containing extracted chemical compounds was investigated to identify the styrene that leached into aging solution using a HS GC-MS method. A Shimadzu GC-MS instrument equipped with a HP-5MS capillary column with a length of 30 m, diameter of 0.25 mm, and film thickness of 0.25 μm (Agilent Technologies, Inc.), and a headspace syringe (2.5 mL) from PAL system (Lake Elmo, MN, USA), was used to identify and quantify any volatile organic compounds (VOCs). Due to high concentrations of compounds extracted by solvent and also variation of chemical concentration from each CIPP liner, extracted samples from site-1 were diluted 10 times and extracted samples from site-2 were diluted 100 times to avoid contamination in GC-MS. Freshly prepared aging solutions were used for dilution i.e., freshly

prepared pore solution was used to dilute the pore solution containing extracted chemicals. Three replicates of the diluted samples, of 10 mL volume containing 1,4-dichlorobenzene-d₄ dissolved in methanol as internal standard (IS), were analyzed by GC-MS. For that, the samples were first placed in autosampler agitator with 250 rpm speed and then incubated at 55 °C for 20 min. Next, the syringe collected 1 mL of the headspace which was immediately injected to GC-MS. IS concentration for samples expected to have higher and lower chemical level was 6.27 mg/L and 57 µg/L, respectively. The oven temperature was initially set at 50 °C and held for 3 min, then ramped to 120 °C at 10°C/min. The purge flow used was 3.0 mL/min and column flow was 1.48 mL/min. Split injection was performed with a hold at 220 °C with a set ratio of 10. Total time for each run was 10 min. Calibration curves were produced for styrene in the range of 50 µg/L to 1.36 µg/L ($R^2 = 0.994$) for the site 1 samples and styrene in the range of 290 µg/L to 3.43 µg/L ($R^2 = 0.999$) for site 2 samples. Analysis of variance (ANOVA, two factors with replication) was conducted to identify variation between type of solution and CIPP sites in liquid-solid extraction experiments by considering 5% level of significance.

3.2.9 Inter-laminar shear strength (ILSS) characterization

The inter-laminar shear strength (ILSS) of the as-received and the aged CIPP liners was determined using a short beam shear test, following standard ASTM D-2344-00 [74]. The short beam shear test was considered to find inter-laminar shear strength of the fiber reinforced composites by generating an inter-laminar shear by bending the sample. The test was performed using a ADAMET Expert 7603 universal testing Machine (Massachusetts, USA). 3-point bending mode was used to study the ILSS [Appendix B Figure B.1]. Displacement mode was used with a cross-head speed of 1.0 mm/min. Load was applied at the center until first failure was observed. The load at the first fracture was used to calculate the inter-laminar shear strength using a relation derived from classical beam theory as shown in the equation 2. Eight or more of each sample type was tested and used to determine the average ILSS value for each sample type.

$$\tau = \frac{0.75 \times F}{W \times t} \quad (2)$$

Where, τ - Shear strength in MPa, F - Maximum applied load in KN, W - Width of Specimen in mm, t - Thickness in mm.

The dimensions of the specimens used in the test were 12 mm wide by 40 mm long. The thickness was the original thickness of the liner around 6.5 mm. The span length in the set up was 19.5 mm and width of each beam was 12 mm, as required by standard ASTM D2344-00. To compare the ILSS properties between site-1 and site-2 and different aging effect, the results were analyzed by using two-way analysis of variance (ANOVA) to check for significance (at 0.05 level).

3.2.10 Fracture surface analysis

The surface and cross-section images of as-received and aged CIPP specimens were investigated using Hitachi S-4800 cold-cathode field-emission scanning electron microscope (FE-SEM). A thin layer of gold was sputtered on the surface of the specimens. Surface images were taken at two different magnifications with accelerating voltages of 10 and 30KV.

3.2.11 Dynamic mechanical analysis (DMA)

A DMA 800 ((TA Instruments, Inc., Delaware, USA) was used for the thermo-mechanical testing. The samples tested were 13 mm wide by 50 mm long. Both as-received and aged specimens were mounted in a 3-point bending set-up. A static load of 1N was applied to the samples while also dynamically oscillating with a deflection maximum of 40 μm amplitude. The temperature ramped at 5 $^{\circ}\text{C}/\text{min}$ from 30 $^{\circ}\text{C}$ to 200 $^{\circ}\text{C}$. Storage and glass transition temperature (T_g) were obtained from the data. To compare the storage modulus and T_g between site-1 and site-2, and different aging effect, the results were analyzed by using two-way analysis of variance (ANOVA) to check for significance (at 0.05 level).

3.3 Results and discussion

3.3.1 Thermal Behavior of CIPP Specimens

Proper curing (crosslinking of polymer resin) of the CIPP liner is important since it strongly influences the mechanical properties and resistance to aggressive environment. Thus, the curing behavior of CIPP from installation sites-1 and site-2 investigated using differential scanning calorimetry with heating-cooling-heating scan. The residual cure of monomer styrene indicates the unreacted resin and this generally correlates with crosslinking. The unreacted monomers of not

fully cured resin undergo further crosslinking at high temperature which shows the exothermic peaks in DSC analysis.

As shown in Figure 3.2, first heating scan shows wide range endotherm attributed to the evaporation of volatile chemicals present in the specimens. In contrast, the second heating scan shows a flat line indicating the absence of volatile components. The broad endothermic peak is more prominent for site-2, indicating the presence of a greater amount of volatile chemicals. Furthermore, the site-2 CIPP liner had a pronounced exotherm with a maximum peak at about 160 °C arising due to the thermal curing of the resin (Appendix B, Figure B.2). This exothermic peak is absent in second heating scan indicated that after first heating scan, the specimens are fully cured, and no volatile chemicals present.

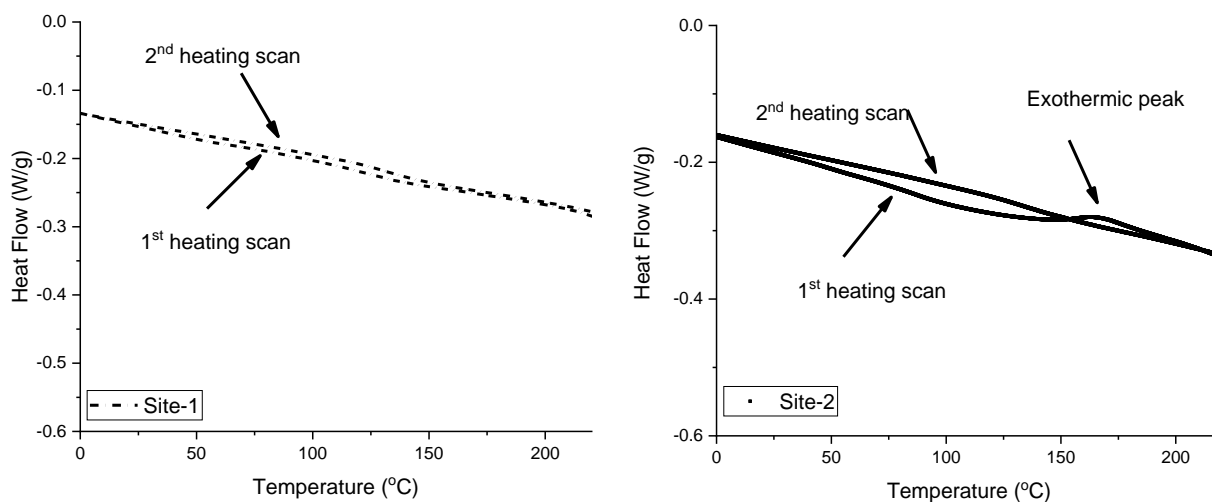


Figure 3.2 DSC curves of CIPP specimens from site-1 and site-2.

Further thermal behavior of CIPP was analyzed using thermogravimetric analysis under air and nitrogen atmosphere as shown in Figure B-3 (Appendix B) and Table 3.1. Volatile content was significantly much greater in site-2's CIPP liner compared site-1's liner. Both site-1 and site-2 liners exhibited 0.5 wt% to 1.7 wt% weight loss at around 120 °C. This was likely due to the evaporation of volatile compounds including styrene [56]. A greater weight loss (1.3 wt% to 3.3 wt%) was found at 160 °C, and is likely attributed to the further evaporation of styrene, oligomeric products of styrene, and other volatile materials. Similar observation for volatile content was reported for steam cured and UV-cured CIPP [7,8,56]. Nuruddin et al. (2019) found 0.8 wt% to

1.6 wt% weight loss of steam cured CIPPs at 160 °C while Li et al. (2019) reported 2.7 wt% to 9.3 wt% weight loss due to emission of volatile compounds for four UV-cured CIPPs [7,56].

Table 3.1 Thermal properties of CIPP from installation site-1 and site-2.

Sample	Weight loss at 120 °C %	Weight loss at 160 °C %	1st step Decomposition Temp °C	2nd step Decomposition Temp °C	Residue Content at 800 °C %
Site-1	0.58 ± 0.47	1.37 ± 1.14	396.17 ± 2.69	534.50 ± 12.61	57.68 ± 1.71
Site-2	1.74 ± 0.50	3.26 ± 0.57	384.20 ± 10.20	522.85 ± 8.10	52.54 ± 7.01

CIPP from both installation sites show two major decompositions. First major decomposition at around 385°C was due to the decomposition of crosslinked structure of unsaturated polyesters while second major decomposition represents the burn off carbon residue remained after first decomposition. CIPP from site-2 exhibits earlier first major decomposition (around 384 °C) than that of site-1 (396 °C), because of improper crosslinking network and uncured residue.

As discussed above, the presence of volatile organic compounds and thermal stability extensively depends on whether the composite was properly cured, with too low of a cure leading to residual. Additives such as plasticizers, degradation products of initiators, as well as unreacted compounds such as styrene and it's oligomeric products may leach into the water during service life. [6–8,56]. So, Fully curing of the CIPP liners during installation can minimize the unwanted leaching of organic chemicals into the environment.

3.3.2 Solution Uptake and Diffusion Behavior of CIPP Liners

CIPP liners made of glass fiber reinforced polymer composite, are viscoelastic materials, and their mechanical and physical properties are strongly time and temperature dependent [75–77]. Therefore, hygrothermal aging at elevated temperatures were used as accelerating factor in order to conduct the durability study of CIPP liners in a limited time. Furthermore, the lifetime prediction and resistance to aggressive environmental conditions like water, saltwater and alkaline conditions, are ongoing concern for fiber reinforced industry. Based on aforementioned reasons and the fact that stormwater liners would experience similar conditions during their service-life, CIPP specimens were aged in water, salt solution and pore solution (simulated aggressive alkaline

condition). Aging involved solution exposure at 50 °C for 15 days which could predict the durability of CIPP after 96 days [Equation B-1].

For both CIPP liners, pore solution exposure caused the greatest weight gain (1.56 wt% to 1.65 wt%) compared to salt (0.57 wt% to 0.64 wt%) and deionized water solutions (0.69-0.74 wt%). As shown in Figure 3.3, weight gain versus time curves for water, salt and concrete pore solution showed an initial linear region, followed by a region concave to the abscissa, although evidence of weight loss due to degradation could be observed for pore solution of site-1 and for all three solution of site-2. Thus, it can be concluded that weight gain behavior of CIPP specimens depended upon the type of solution, and on the curing behavior of the composite materials. Pore solution causes catastrophic damage and created much more new sorption sites. Thus, pore solution aging shows significantly higher uptake rate and equilibrium mass uptake while those values were lower for salt solution.

Hygrothermal aging of the CIPP samples was conducted at elevated temperature (at 50 °C). Damage in the form of crazing, microcracking, and hydrolysis of vinyl ester resin was observed. Leaching of unreacted styrene and other volatile additives out of the samples also occurred. These phenomena likely resulted in additional sorption sites [78].

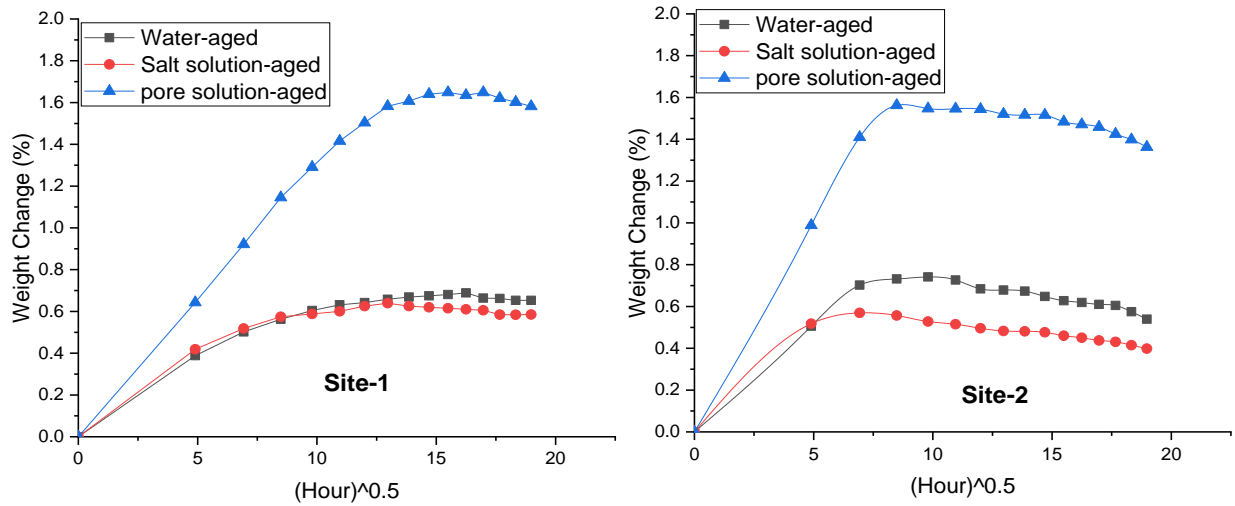


Figure 3.3 Weight gain vs time curves of site-1 and site-2 CIPP samples for water, salt and pore solution aging.

Interestingly, site-1 and site-2 CIPP liner's solution uptake behavior differed. Specimens from site-1 take longer time to reach equilibrium, although both installation sites used the same resin (vinyl ester resin) and fibers (fiber glass) for lining. For site-2, there are some uncured region, which causes leaching of unreacted styrene and initiators out of the specimens, and susceptible to be more damaged and resulted in reaching equilibrium solution uptake within a short period of time. In contrast, site-1 is fully cured, thus allowing much less sorption and diffusion sites, which resulted in longer time to reach equilibrium uptake.

Table 3.2 Equilibrium sorption and Fickian diffusion coefficient of CIPP specimens from Site-1 and site-2 for water, salt and pore solution.

Samples	Aging solution	pH of the Solution	Equilibrium sorption %	Diffusivity, $\times 10^{-7}$ cm ² /s
Site-1	Water	7.45	0.69	2.93
	Salt solution	8.25	0.64	4.77
	Pore solution	13.5	1.65
Site-2	Water	7.45	0.74
	Salt solution	8.25	0.57
	Pore solution	13.5	1.56

The equilibrium sorption and diffusion coefficient depended on the aging condition and residual curing of the liners as shown in Table 3.2. Furthermore, the equilibrium uptake and diffusion of CIPP specimens in DI water and salt solution showed opposite trends. Salt solution aging showed lower moisture sorption in compared to water aging. Soulier et al. (1988) studied the interaction of salt solution with fiber reinforced epoxy composite and reported lower equilibrium weight gain in sodium chloride solution [79]. Interestingly, the salt solution diffusivity ($4.77 \text{ cm}^2\text{s}^{-1}$) is higher than pure water ($2.93 \text{ cm}^2\text{s}^{-1}$). It can be anticipated that the salt solution weakening the fiber-matrix interface and degrading the matrix, which creates more free volume for the water molecules for the movement. In contrast, the equilibrium sorption of pore solution of CIPP specimens from both sites are higher than water and salt solution. The higher equilibrium sorption is associated with the penetration of pore solution and the occupation in the interlaminar space, voids and microcracks in the liners followed by deposition of Ca(OH)_2 . Thus, the added weight because of the nucleation and deposition of Ca(OH)_2 inside the CIPP liners may mislead the calculation of equilibrium water uptake [64].

As shown in Table 3.2, the equilibrium water uptake of CIPP specimens for site-1 and site-2 are 0.69 % and 0.57 % respectively. Similar water uptake behavior reported in the literature [80–83]. The lower uptake behavior of site-2 is due to leaching of the unreacted styrene and the degradation of the specimens. Furthermore, presence of uncured regions makes them easier for breaking the polymeric network and weakening the interface, which causes degradation after immersion in water, salt and pore solution. The actual equilibrium sorption could not be obtained because of the degradation [84,85]. Therefore, this data could not be used to calculate diffusion coefficients for CIPP from site-2. As penetrant sorption and desorption of degraded material occurred simultaneously, the equilibrium sorption data will make the estimated diffusion coefficient questionable.

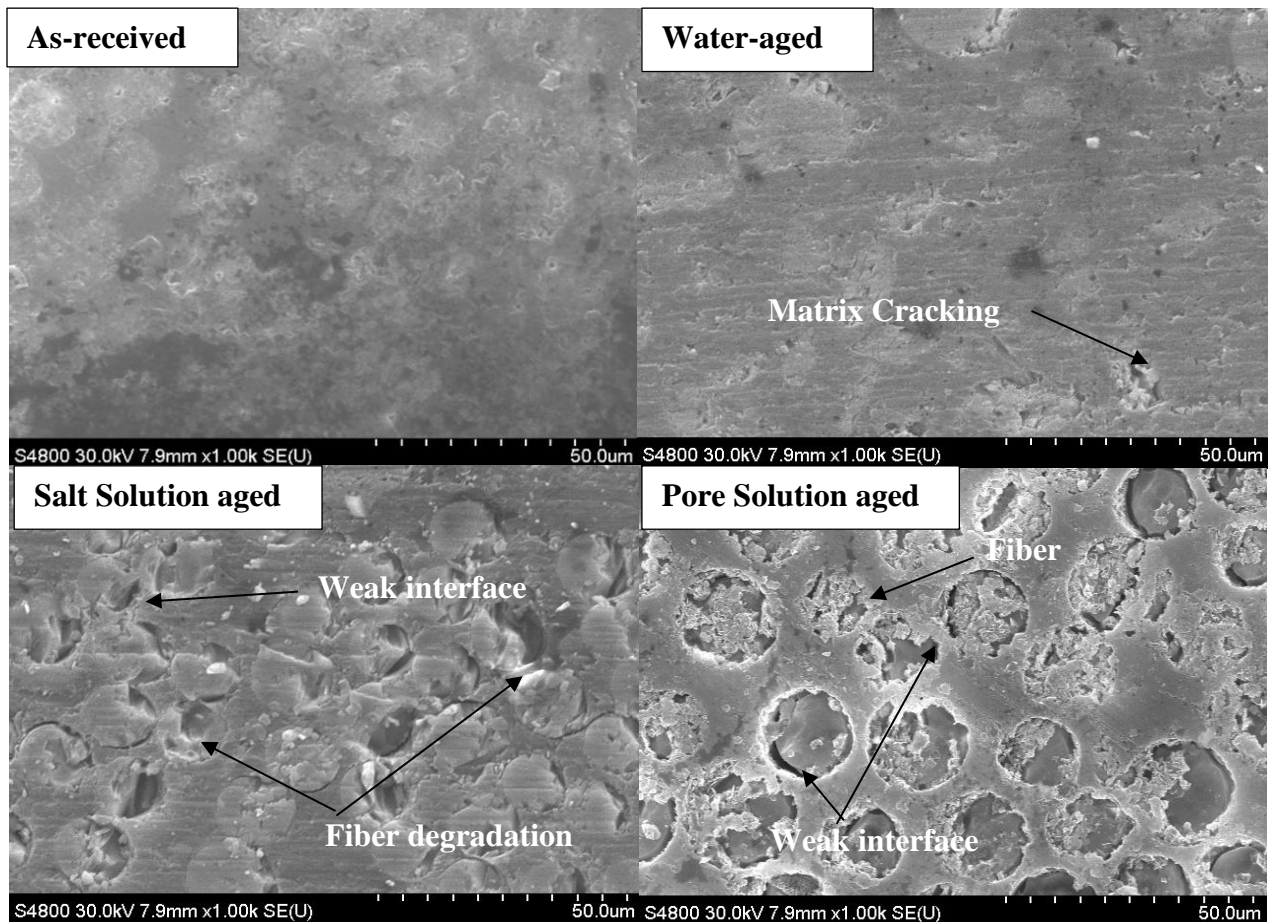


Figure 3.4 Morphology of as-received CIPP specimens from site-1 and after aging with water, salt and pore solution.

As shown in Figure 3.4, the microscopy images of the aged specimens indicate that the water, salt and pore solutions each cause matrix cracking. The pore solution damages both the matrix and fibers severely, and weakens the interfacial adhesion by degrading the matrix at the interface. There was no notable morphological difference in the images from site-1 and site-2, which indicates that visual inspection, is not the best method for determining whether a material is fully cured or not. From our data TGA and DSC are better discriminators to assess the degree of curing. The material morphology is visibly different because of aging in the various solutions, and therefore microscopy is valuable in assessing physical material degradation post-curing.

Differences between the amount of sodium (Na), potassium (K) or calcium (Ca) were found of interior of the as-received, water-conditioned, salt-conditioned, and pore solution conditioned specimens, (Table 3.3). Potassium and calcium were found in all specimens. Tap water and DI water contained calcium and potassium ions [Table B.1]. We are expecting that the potassium and calcium ingressed into the specimens during polishing the sample before conducting the experiment. The concentration of potassium, sodium, and calcium cations in salt and pore solutions was significantly greater. Significantly greater amounts of cations were found on salt and pore solution exposed specimens compared to those exposed to tap water and DI water solutions. As shown in Table 3.3, the concentration of calcium (8.72 wt%) was higher in compared to potassium (0.26 wt%) and sodium (0.26 wt%) although sodium has higher ionic mobility [86]. Chakraverty et al. (2015) reported that sodium ion has higher affinity for chloride ion as compared to that of calcium ion with chloride ion [86]. Therefore, less sodium ions penetrate into composite body in compared to calcium ions. Chin et al. (2001) reported that sodium ions did not transported into the vinyl ester and polyester polymer after immersion in salt solution [2]. Nevertheless, the ingress of these ions into the CIPP specimens impart visible physical degradation of the specimens through matrix micro-cracking and weakening the matrix-fiber interface and provide additional pathway for ions transportation into the specimens.

Table 3.3 Surface concentration of ions for the CIPP specimens.

Samples	Concentration (wt.%)							
	C	O	Si	Ca	K	Na	Cl	S
As-received	57.5	26.25	7.5	3.75	1.25	0	1.25	2.5
Water-aged	70.13	18.18	4.76	4.76	0.43	0	0.44	1.3
Salt solution-aged	67.9	19.1	3.3	2.5	0.3	0.1	6.8	0
Pore solution-aged	53.3	25.68	11.26	8.72	0.26	0.26	0.26	0.26

3.3.3 Role of Nature of Solution in Extracting Styrene from CIPPs into Water

The influence of ionic strength on the styrene extraction efficiency was investigated because the ionic strength can influence the partition coefficient between the gas and the liquid phases. Notably, the authors compared the styrene extraction ability of three solutions (deionized water, salt solution and pore solution) for material from site-1 and site-2 (i.e. “fully cured” and “under-cured” respectively based on DSC results). Results showed that greater amounts of styrene were always extracted from CIPP of site-2 samples compared to site-1 samples (Table 3.4). This result is supported by chemical characterization of those same CIPPs by Li et al. (2019) [7]. Li et al. (2019) found that when tap water was used to flush each CIPP, styrene in site-2 rinse water (446 µg styrene/L) was greater than styrene in site-1 rinse water (3.2 µg styrene/L) [7]. Results presented in Table 3.4 indicate that for both CIPP liners, composite exposure to saltwater resulted in the least amount of styrene release, but no difference was found between DI water and pore solution water. The liners exposed to saltwater gained the least water weight (Table 3.2) indicating a minimal amount of mass transport in and out of the material relative to the other solutions. The pore solution caused the greatest amount of styrene release for the material from site-1. In contrast, deionized water caused greatest styrene leaching for site-2. For both site-1 and site-2, salt solution leached least amount of styrene. Most importantly, the degree of curing dictates the total amount of styrene available to be released when exposed to any of the three test solutions, as the styrene measured from site-2 is an order of magnitude greater than the site-1 styrene levels.

Table 3.4 Styrene concentration of samples detected and quantified by GC-MS.

Sample	Ionic strength	Concentration, mg/L	
		Site 1	Site 2
Deionized water	$<10^{-6}$	8.48 ± 3.46	279.93 ± 6.39
Salt solution	2.21	4.30 ± 0.07	152.69 ± 1.06
Pore Solution	0.61	11.21 ± 1.42	272.40 ± 7.03

3.3.4 Effect of Aging on Interlaminar Shear Strength of CIPP Liners

The interlaminar shear strength of the fiber reinforced composite can be deduced from the force at rupture, which indicates the adhesion strength of fiber-matrix. ILSS was expected to change depending on the curing condition and hygrothermal aging. As shown in Figure 3.5, the interlaminar shear strength of site-1 and site-2 before aging were 18.15 and 16.09 MPa, respectively. The lower value of ILSS property of site-2 is due to the presence of improper curing. Improper crosslinking weakens the fiber/matrix adhesion. Furthermore, the unreacted styrene can weaken the strength of fiber/matrix bonding in CIPP liners.

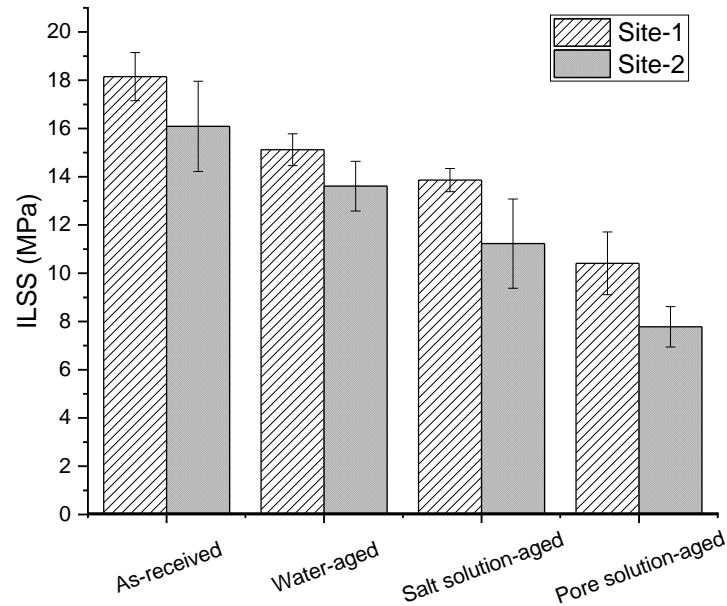


Figure 3.5 Interlaminar shear strength (ILSS) of CIPP from site 1 and 2 at different environment conditions.

The overall decrease in ILSS property of CIPP specimens of both sites was observed for all environmental (water, salt and pore solution) aging. Water aging at elevated temperature (50 °C) for 15 days decreased the ILSS by 16.7 and 15.4% for both CIPP specimens of site-1 and site-2, respectively. Environmental aging at elevated temperature induced thermal oxidation, environmental stress cracking (ESC), and chemical scissioning of polymer matrix [87], which can create free radicals, which in the presence of oxygen form peroxides, which can later form radicals during heating. During hygrothermal aging at elevated temperature, these radicals from chain scission or peroxides can further breakdown polymer chains. In addition, difference in thermal expansion of matrix and fibers may cause thermo-mechanical degradation during hygrothermal aging [87]. Similar to differential thermal expansion, a mismatch of the hygroscopic swelling property of resin matrix and fibers leads to matrix cracking [88]. Furthermore, environmental stress promotes crazing and cracking in the matrix which weakens the adhesion strength of the fiber-matrix interface [87]. Most importantly, the ester group at the chain ends of the polymer matrix are susceptible to undergo hydrolysis reaction which cause chain scission of cross-linked network of the polymers, resulting in poor load transferring efficiency between the matrix and the fiber [3]. In addition, glass fibers also undergo degradation during hygrothermal aging due to the leaching of alkali oxides from glass fiber surface and may lead to the formation of surface micro-cracks which can act as stress concentrators, thus weakening the fiber strength [86].

The influence of salt and pore solution was more destructive as compared to water aging. Salt solution decreased the ILSS of CIPP samples from site-1 and site-2 by 24 and 34%, respectively. Chin et al. (1999) reported that salt solution accelerated the degradation mechanism by hydrolysis of ester group of polymer chain [84]. Furthermore, some salt solution may diffuse into the matrix and creates flaws at the fiber/matrix interface, which will nucleate the matrix crack and weaken the fiber/matrix interfacial bonding. It is also important to note that the decreased of ILSS value was maximum for both site-1 and site-2. About 43 and 54% decreased in ILSS of site-1 and site-2 were observed after aging with pore solution. Pore solution catalyzes the hydrolysis reaction of ester linkage to form carboxylic ions which further react with alkali to form salts [89]. The newly formed salts and alkali remain in the matrix system or matrix/fibers interface, and thus, they crystallize and grow over the surface of the fibers, reducing the cross-sectional area of the fibers and resistance to the applied load. Glass fibers also deteriorates in pore solution aging due to the dissolution of silica network of fibers [90,91]. The synergistic effect of both hydrolysis of

matrix and dissolution of fibers weakens the strength of fiber/matrix interface. The ILSS property of pore solution aged CIPP specimens are lower because of detrimental damage of both fibers and matrix.

The fracture surface of the as-received and aged specimens were investigated by optical and scanning electron microscopy. As shown in Figure 3.6, the typical brittle failure could be observed for all specimens, indicating matrix cracking, crack propagation and delamination. Similar to the prior microscopy images in Figure 3.4, there was no difference in the site-1 and site-2 morphology; site-1 data is presented as representative data. The longitudinal section of fracture surface of unconditioned samples was relatively smooth, and the fibers are well imbedded in the matrix. However, after aging especially salt and pore solution aging, most of the fibers are observed to have exfoliated from the matrix, demonstrating the poor matrix/fiber interfacial bonding. It is interesting to notice that the failure of the salt solution and pore solution aged CIPP specimens is the result of fiber pullout rather than the failure of the fibers themselves. Fiber pullout indicates weak fiber-matrix interface bonding, and most of the single fibers could not take up their potential maximum load before the initiation of failure. A similar failure mechanism (e.g. fiber pull-out, matrix cracking, fiber breaking, delaminating, etc.) was reported in literature for aging of fiber reinforced polymer composites [92–96].

3.3.5 Effect of Aging on Viscoelastic Properties of CIPP Liners

The visco-elastic properties of as-received and aged CIPP specimens were investigated to evaluate the effect of water, salt solution and pore solution aging on storage modulus and glass transition temperature (T_g). As shown in Figure 3.7, the storage modulus and glass transition temperature of as-received CIPP from site-1, were 4,935 MPa and 148 °C, respectively. Water aging improved the storage modulus and T_g of site-1 by 37% and 3 °C, respectively. The most likely causes of increased visco-elastic property for water aging, are leaching of low molecular weight flexibilizing segments of the matrix such as styrene, unreacted initiators, additives, etc., and additional crosslinking, which leads to network embrittlement [1]. Salt solution increased the embrittlement, and in the same time degrade the specimens by chain scissioning, swelling, environmental stress cracking and thermal aging which may lower the property [86,97]. Therefore, no significant change in storage modulus and T_g values was observed because of this competing behavior for salt solution aging. In contrast, pore solution aging decreased the storage modulus by

29% but increased the glass transition temperature by 3°C. Significant increase in T_g value was attributed to the penetration of metal ions such as Ca, K, and Na into the CIPP composite body which occupy the free volume and restricts the movement of polymer chain segment. Furthermore, the decrease in modulus for pore solution aging is due to the combined action of the elevated temperature and pore solution, which causes chemical degradation of polymer chains and poor fiber-matrix interactions. Yao and Ziegmann (2007) investigated the accelerated water aging for pipe made of glass fiber reinforced epoxy and polyvinyl ester resins, and found decreased in glass transition temperature and storage modulus of the pipe [98]. Overall these aging results for water, saltwater and pore solution indicate that the mechanical integrity remains consistent for water and saltwater exposure, which are the most common application environments for CIPP. However, as mechanical performance of the pipe depends on the viscoelastic properties of the materials, the CIPP liners are apparently susceptible to undergo catastrophic failure in extremely alkaline environments such as the model pore solution tested here.

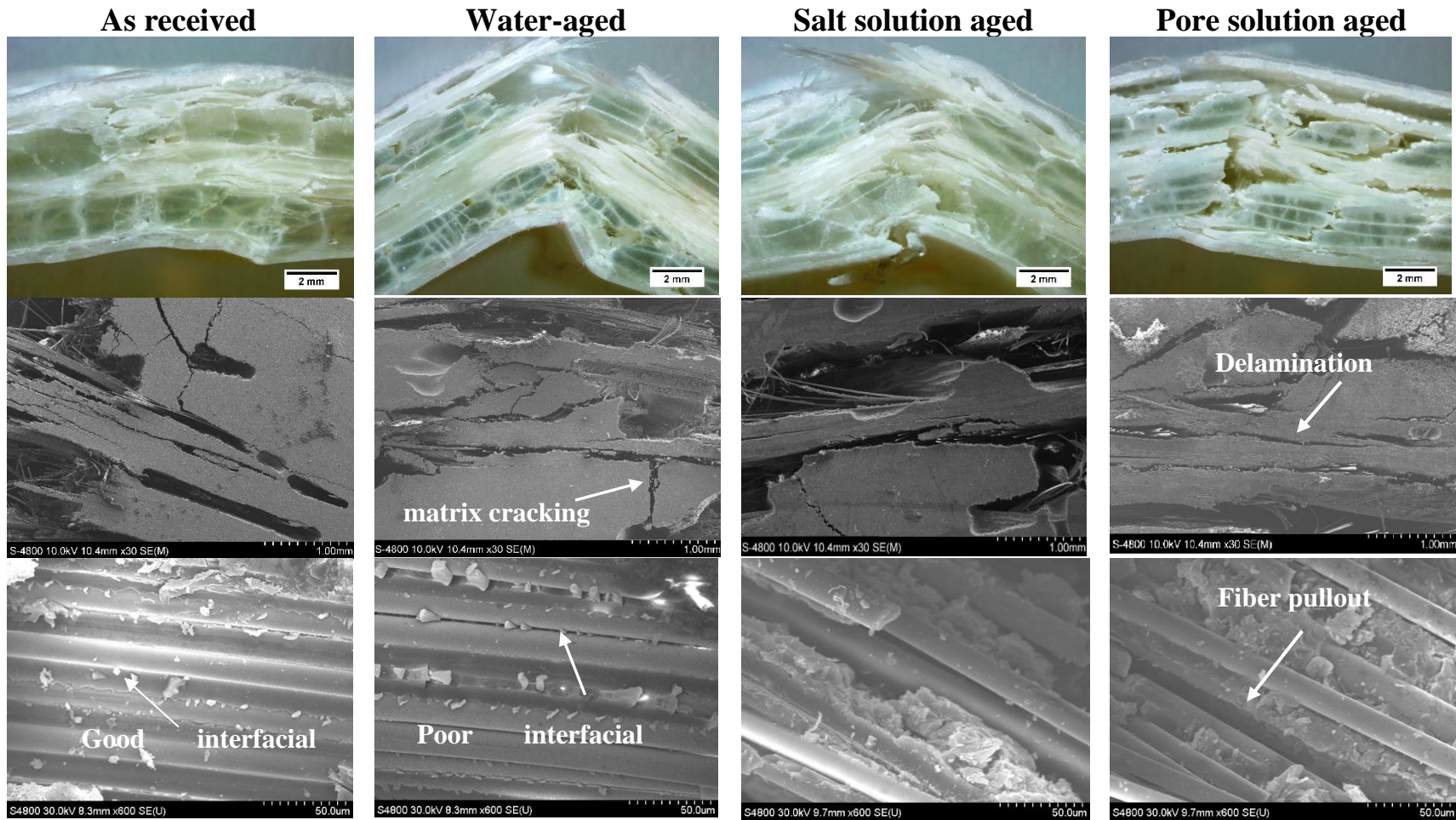


Figure 3.6 Optical images and Scanning electron microscopic images of fracture surface of as-received and aged CIPP specimens.

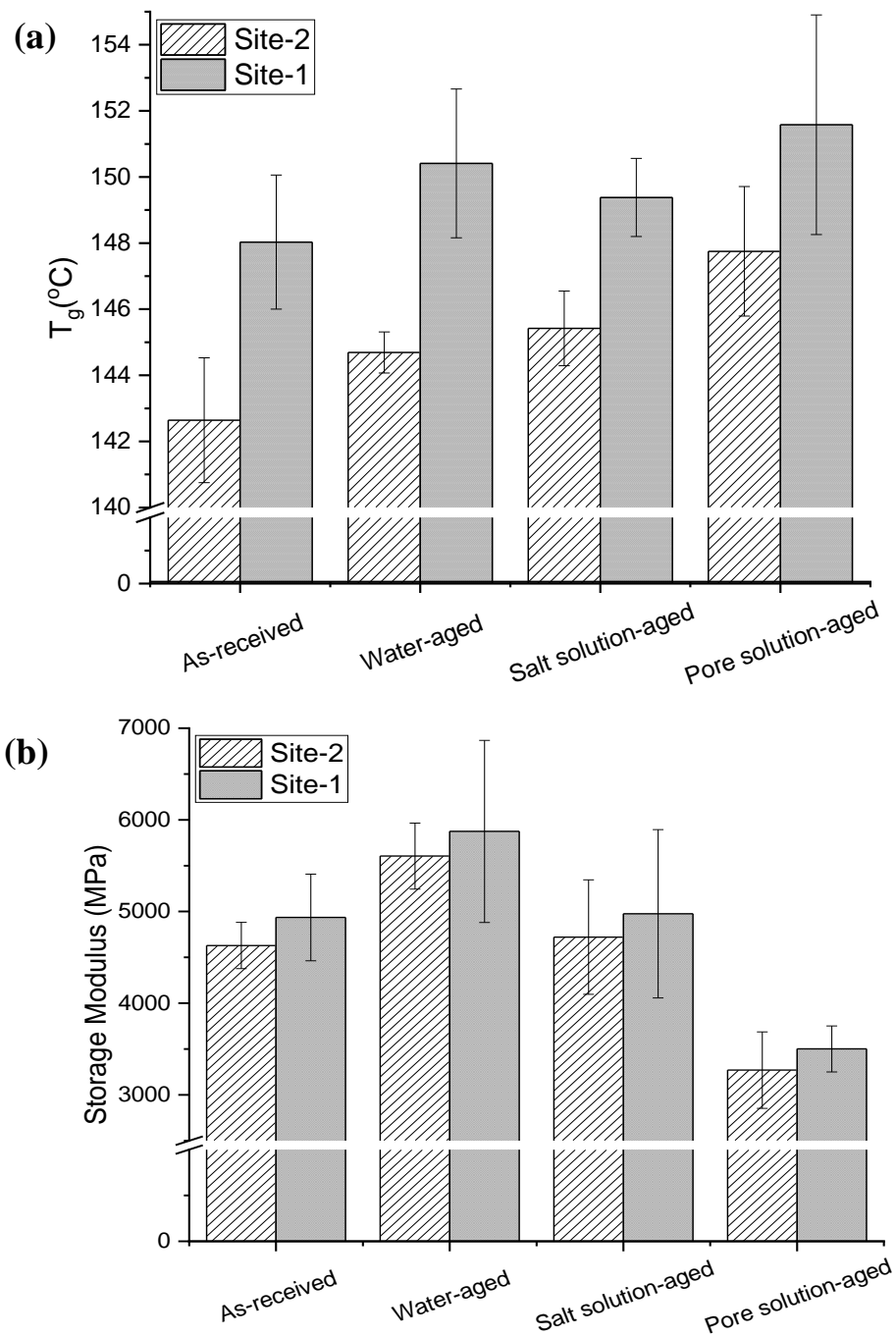


Figure 3.7 Glass transition temperature (T_g) and storage modulus of as-received and aged CIPP from 2 different installation sites.

It is interesting to note that site-2 has lower storage modulus (4,629 MPa) and glass transition temperature (142 °C) as compared to site-1. As discussed earlier that CIPP from installation site-2 is under-cured, the presence of unreacted styrene molecule, initiators, and partially cross-linked polymer molecules causes the chain segment of polymer matrix to be more flexible as compared to fully cured CIPP. Water aging of the specimen induced residual crosslinking and resulted in increased storage modulus and T_g value by 21% and 2 °C, respectively. Furthermore, no significant change in storage modulus could be observed for salt aging although T_g value was increased by 3 °C. On the other hand, similar to site 1, the storage modulus of pore solution aged specimens was decreased by 29% while T_g value increased by 5 °C. Garland (2000) studied the water aging of pultruded vinyl ester/glass composites for 3,000 hr at different elevated temperatures (25, 50 and 85 °C) to understand the effect of accelerated aging on mechanical performance and the extent of curing of the composite [99]. Garland (2000) reported that water aging at elevated temperature increased both storage modulus and T_g as aging process increased the crosslinked density due to further curing of the composite. For CIPP system, the increase in both stiffness and T_g means the suitability of the liners for stormwater rehabilitation as the liners become more stiffer within their service. In contrast, lowering storage modulus in pore solution indicated that CIPP for rehabilitation will be a poor choice in aggressive environments like alkali environments.

The mechanical performance of a CIPP depends strongly on its T_g , as above this temperature the mechanical properties decrease rapidly. Furthermore, the storage modulus is similar to Young's modulus which indicates the inherent stiffness of the material [99]. Thus, in order to properly predict the service lives of the CIPP liners, one must consider the role of aggressive environment, temperature, exposure time, and presence of residual curing.

3.4 Summary

The durability of UV-cured CIPPs from two different storm sewer installation sites was investigated to understand the effect of water, salt solution, and pore solution aging. Installation site-1 specimens were found to be fully cured (fully crosslinked) while site-2 CIPP specimens were not fully cured (presence of residual curing). CIPP durability and chemical leaching was influenced by the curing and aging conditions. Site-2 specimens have higher volatile contents and lower thermal stability as compared to site-1. The greater amount of volatile content and under curing condition caused site-2 specimens to have a lower T_g . CIPP specimens exhibited different

moisture uptake behavior in the different chemical environments. Moisture uptake behavior of cured CIPP specimens (site-1) in water and salt solutions follow Fickian behavior although non-fickian behavior was observed for the pore solution condition. This is likely because of matrix cracking and Ca(OH)_2 deposition in the liners. Furthermore, undercured CIPP specimens (site-2) also follow non-Fickian behavior for aging with all three types of solutions because of matrix chain scissioning and hydrolysis. During CIPP aging, unreacted styrene monomer diffuses out into the solution. GC-MS results suggested that the aging operations leached out a significant quantity of styrene for the site-2 undercured material; for site-1 “fully cured” pipes leaching was significant but an order of magnitude lower. The interlaminar shear strength and storage modulus of CIPP from site-1 was higher than that of site-2. Results show that CIPP aging can increase the T_g due to the post curing of the specimens and leaching of unreacted monomers and volatiles. Water, salt, and pore solution aging significantly reduced the interlaminar shear strength. Long-term exposure to salt and alkaline environments may have detrimental effect on performance of CIPP liners.

CHAPTER 4. THE INFLUENCE OF FREE VOLUME DETERMINED BY POSITRON ANNIHILATION LIFETIME SPECTROSCOPY (PALS) ON GAS PERMEABILITY OF CELLULOSE NANOCRYSTALS FILMS

All research work except Herman's order parameter determination experiment was performed by Md Nuruddin. All analysis except free volume analysis was performed by Md Nuruddin with guidance by Prof. John Howarter and Jeffrey P. Youngblood. All writing was performed by Md Nuruddin with guidance and editing by Prof. John Howarter and Jeffrey P. Youngblood.

4.1 Introduction

Over the past few decades, polymeric materials have become the dominant materials for development of packaging because of their light weight, flexibility, crack-resistance and low cost [100]. Unfortunately, unlike glass and metal-based packaging materials, a major drawback of common polymer-based packaging materials is their relatively high permeability to gas and moisture, which limits their industrial usage as single component packaging materials. The main concern for polymer-based packaging materials in food, pharmaceutical, electronics and microelectronics is oxygen and moisture barrier performance. The ingress of moisture and oxygen from the environment to the packaged products leads to oxidation and corrosion of electronic devices and food/pharmaceutical products and drastically decreases lifetime [100–102]. Unfortunately, a polymer with high oxygen barrier property may be moisture sensitive and vice versa [103,104]. To overcome this drawback, flexible packaging films are coated, laminated or co-extruded with high oxygen barrier polymers like EVOH or PVDC, or coated with inorganics such as silica or aluminum to enhance barrier performance [105–107]. However, these multilayer approaches lack sustainability as they make it impossible to recycle the finished product and most of these materials are non-biodegradable [103]. Therefore, the packaging industry has drawn attention towards high barrier alternative packaging materials for coatings in terms of biodegradability, recyclability, easy separation from surface, and ecological friendliness [108,109].

Cellulose nanomaterials (CNs) have drawn wide attention as renewable and sustainable nanomaterials and offer a promising alternative to traditional petroleum-based materials in the field of food packaging polymers [110–112], barrier coating [113–117], electronic packaging [118] and structural applications [119–124]. CNs can be extracted in the form of cellulose nanocrystals (CNCs) and cellulose nanofibers (CNFs) from various cellulose sources (e.g. wood, plant,

agricultural residues, trees, tunicate, algae and bacterial) [125–128]. CNCs have a rod-like shape (i.e., 3-5 nm wide by 100-200 nm long) and have been explored for packaging applications because of their high crystallinity (about 85%) and mechanical properties (the strength and axial modulus are 7.5–7.7 GPa and 110–220 GPa, respectively) [10,11].

CNCs are highly crystalline and, therefore, gas molecules and moisture are impermeable through individual CNCs. However, as multiple CNCs stack to form nanostructured films when drying CNC suspensions free volume is left between the CNCs which gas molecules can use for diffusion throughout the film. The available free volume is thus the governing parameter to control the gas diffusion and is dependent upon the CNC-CNC interspacing. During CNC composite processing at ambient conditions, CNCs can arrange in a chiral nematic arrangement [129]. However, CNCs can be oriented in a given direction by using an external force which can be achieved by several methods such as magnetic [130,131], electric [132,133] or shear-based alignment [134,135]. It has been shown that the mechanical, thermal, and hygroscopic swelling properties are dependent upon the structure of the finished dried CNCs film (chiral or aligned) [118,123,129,136]. Chowdhury et al. (2019) investigated the effect of shear induced orientation in CNC films on gas permeability. They inferred that alignment of individual CNCs in the shear directions can reduce the interfacial spaces (free volume) between CNCs and thereby, decrease the gas permeability [137].

Several techniques, such as x-ray or neutron scattering, Fourier transform infra-red (FTIR) spectroscopy, differential scanning calorimetry (DSC), electron microscopy, and dynamic mechanical analysis (DMA) can be employed in an indirect way to give an idea about the free volume in polymers and nanocomposites [138]. However, few direct methods for free volume measurement exist. Positron annihilation lifetime spectroscopy (PALS) is a well-established technique for measuring the free volume size, density and size distribution in polymers and polymer nanocomposites [139,140]. To the best of our knowledge, to date neither PALS nor free volume of CNC films has been measured quantitatively. Previous studies predicted free volume of shear oriented (aligned) and self-organized CNC (chiral) films qualitatively by measuring density and Herman's order parameter [129,137,141]. Recently, Torstensen *et al.* developed a new pathway to measure the free volume of TEMPO-oxidized CNF film by PALS [142], however, they did not measure CNCs nor consider any structural orientation of the cellulose nanomaterials.

In the current study, the relation of free volume as measured by PALS, Herman's order parameter and the gas barrier performance in CNC films (aligned and chiral) was investigated. Self-organized and shear-oriented CNC films were prepared and free volume size and density of the CNC films were measured. Additional insight into free volume of CNC films was obtained by investigating oxygen and carbon dioxide gas permeability of the films and comparing with other engineering polymers. Finally, the Dil model [143], which was originally developed for nanocomposite system, was modified for this single component CNC system to predict the effect CNC alignment in the finished film on permeability of oxygen and carbon dioxide.

4.2 Materials and Experiments

4.2.1 Materials

11.9 wt% cellulose nanocrystal aqueous suspension containing 0.99 wt% sulfur on dry CNC (Batch# 014-FPL-065) were purchased from the University of Maine (Orono, Maine, USA). Based on TEM analysis (Appendix C, Figure C1), the average particle length and width were 100 ± 25 nm and 5 ± 1.5 nm respectively. The zeta potential and crystallinity of the CNCs were -47 ± 2 mV and 85.5%, respectively (Appendix C, Figure C2 and C3).

4.2.2 Preparation of CNC Film

Self-organized and shear-oriented CNC films were prepared according to the method reported by Shrestha *et al.* (2017) and Diaz *et al.* (2013) [129,141].

For preparation of self-organized CNC films, an aqueous suspension of 2 wt% CNC was poured into polystyrene Petri dishes of 100 mm in diameter (Figure 4.1) and kept at room temperature and 50% RH for 7 days to allow water to evaporate slowly. At the end of the drying, the dried self-organized films were peeled from the Petri dish.

For preparation of shear-oriented CNC films, 10 ml of 11.9 wt% CNC suspensions were cast on a clean glass substrate containing two 0.6 mm thick polyethylene terephthalate (PET) strips at the edges as shown in Figure 4.1. A regular razor blade of 4 cm wide was used to apply shear to align the CNC crystals in the shear direction. After shearing, the films were kept at room temperature and 50% RH for 7 days to evaporate the water slowly. At the end of their drying period, the shear-oriented films were peeled from the substrate.

Preparation of Self-organized CNC films

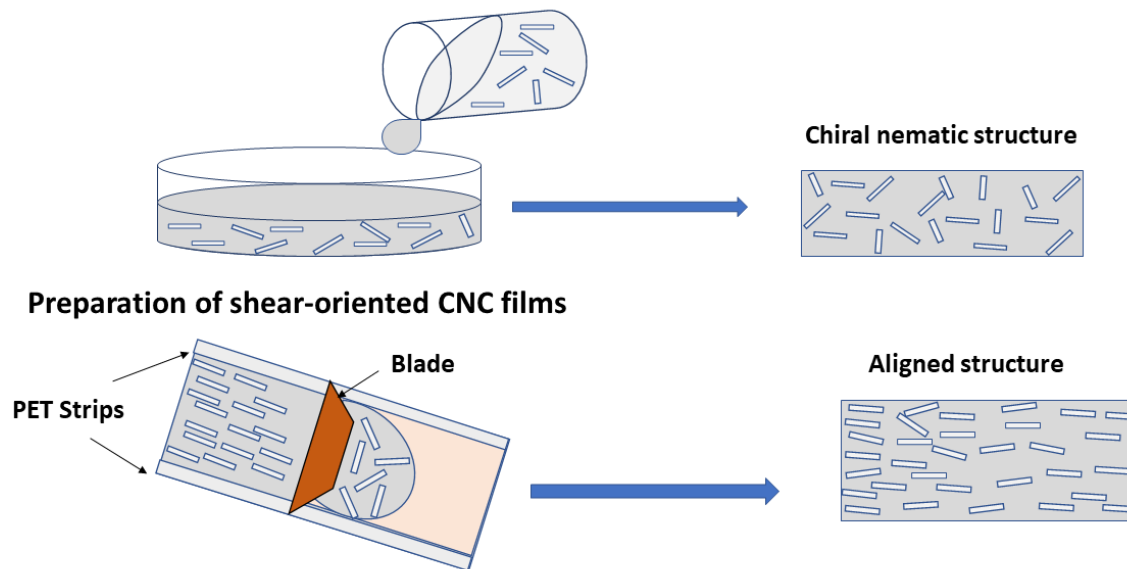


Figure 4.1 Schematic of preparation of self-organized and shear-oriented CNC films.

4.2.3 Preparation of CNC coated Polypropylene (PP)

The shear-oriented and self-organized CNC films are highly brittle in nature which prevent crack-free sealing in the gas permeation film holder. Hence, CNC coated PP films were prepared for measuring the barrier performance of shear-oriented CNC films as PP has a high relative permeability. The surface tension of the CNC suspension was 70 dynes/cm, as measured by pendant drop tensiometer while the surface energy of the polypropylene film was 28 dynes/cm (measured by goniometer) [Appendix C]. The polypropylene surface was corona treated 5-6 times to compatibilized the substrate and coating system, using BD-20AC Laboratory Corona Treater (Electro-Technic Products, Chicago, USA). As shown in Figure 4.2, immediately after the corona treatment, CNC coatings were applied on polypropylene thin films using a K Hand coater (Bar No. 2, wet film thickness 12 micron) from Testing Machines Inc. (New Castle, DE, USA). The coated films were immediately placed in an oven maintained at 60 °C for 5 mins to dry. In contrast, for self-organized CNC films coated PP, corona treated PP film was fixed inside the petri dish of 100 mm in diameter. An aqueous suspension of 2 wt% CNC was poured into the polystyrene Petri dishes containing PP films and kept at room temperature and 50% RH for 7 days to allow water to evaporate slowly. At the end of the drying, the dried self-organized films coated PP films were

peeled off from the petri dish. All dried coated films were stored in desiccator at <5% RH until gas permeability measurement was conducted.

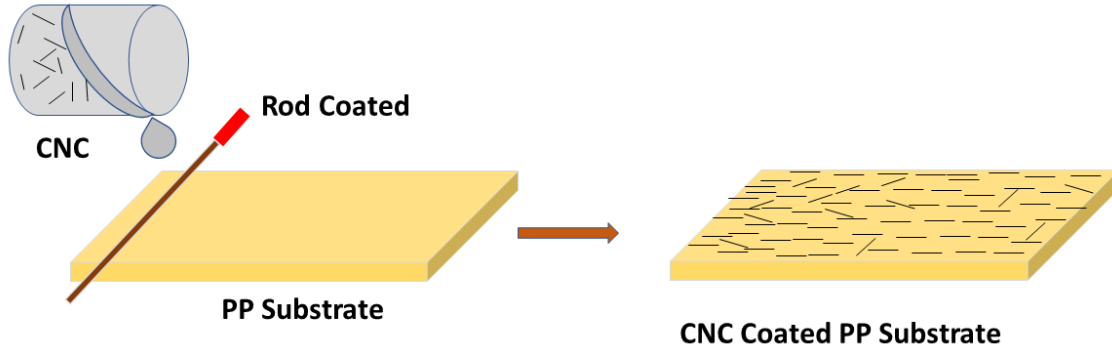


Figure 4.2 Schematic of preparation of CNC coated PP films.

4.2.4 Herman's order parameter determination

A Carl Zeiss (Axio observer A1) inverted polarized light microscope in transmission mode was used for imaging the samples at 45° and 90° to the linear polarized light in bright field. Herman's order parameter for self-organized and shear-oriented CNC films were calculated using a conventional UV-Vis spectrophotometer (Spectra max Plus 384, Molecular devices Corp. Sunnyvale, CA) with a method according to Chowdhury *et al.* (2017) [144]. Briefly, a sample (chiral or aligned) was placed between a cross-polarizer. The transmitted light intensity in the wavelength regions 400-750 nm was measured at 45° and 90° configurations. The Herman's order parameter (S) was calculated from the following equations:

$$I_{\theta} = I_0 \sin^2 2\theta \sin^2 \left(\frac{\pi \Delta n d}{\lambda} \right) \quad (4.1)$$

$$\text{And, } \frac{I_{45}}{I_{90}} = D^* = D, g = \frac{(2S+1)}{1-S} \quad (4.2)$$

where, I_0 , θ , Δn , d , λ , I_{45} , I_{90} , g and D represent the amplitude of the incident light, sample angle regarding incident light, refractive index difference, film thickness, wavelength, transmitted light intensity for the 45° configuration, transmitted light intensity for the 90° configuration, correction factor and dichroic ratio, respectively. The material is considered random if $S=0$ while $S=1$ for perfectly aligned arrangement.

4.2.5 Gas permeability measurement

The pure gas permeability (O₂, CO₂) of self-organized (chiral nematic) and shear-oriented CNC coated PP films were measured by a custom made constant-volume/variable-pressure permeation system [Appendix C]. A detailed description of the instrumentation was reported by Chowdhury *et al.* (2019) [137]. Briefly, the CNC coated films of 25 mm diameter were cut precisely with high precision scissors. The film was enclosed inside a sample holder with an exposed area of 2.7 cm² for gas transportation. After degassing the entire system by vacuum, the downstream side of the instrument was closed and the feed gas (O₂, CO₂) was introduced to the upstream side at a fixed pressure. The pressure rise in the downstream volume as a function of time was measured. The gas permeability of the film was calculated using the following expression [145]:

$$P = \frac{V_d l}{P_2 A R T} \left[\left(\frac{dp}{dT} \right)_{ss} - \left(\frac{dp}{dT} \right)_{leak} \right] \quad (4.3)$$

where, V_d (cm³) is the downstream volume (volume of tank and tube), l is the film thickness (cm), P_2 is the upstream absolute pressure (cmHg), A is the film's exposed area for gas transportation (cm²), R is the gas constant (0.278 cmHg cm³/[cm³(STP)K], and T is absolute temperature (K). Furthermore, $\left(\frac{dp}{dt} \right)_{ss}$ and $\left(\frac{dp}{dt} \right)_{leak}$ are the steady state pressure rise in the downstream volume during gas permeation through the films and leak testing, respectively. The gas permeability of the CNC coated layer was calculated using the following expression [146]:

$$P_c = \frac{h_c}{\frac{h_1}{P_1} + \frac{h_2}{P_2}} \quad (4.4)$$

where P_c , h_c , P_1 , P_2 , h_1 , h_2 are permeability of CNC coated PP, thickness of CNC-coated PP, thickness of PP substrate, thickness of CNC coated layer, and permeability PP substrate, respectively.

4.2.6 Positron Annihilation Lifetime Spectroscopy

The PALS measurements of self-organized and shear oriented CNCs were performed according to Torstensen *et al.* (2018) [142]. Briefly, brittle CNC films (self-organized or shear oriented) were broken into pieces and stored in a desiccator maintaining 0-10% RH for 7 days. Approximately half of a 20 ml glass vial was filled with ground CNC film pieces (totaling of

around 2 gm). A 20 μCi ^{22}Na positron source encapsulated by Kapton[®] films was placed among the pieces of CNCs so that the source was roughly in the middle of the vial. The rest of the vial was then filled with CNC pieces. A spacer made of aluminium sheet, was used to keep pressure on the samples to minimize the spurious signals from air. The vial containing samples and positron source was then capped tightly with a predrilled hole in the vial cap to allow equilibration with the surrounding environment. The vial was kept inside a sealed Ziploc bag containing desiccant during the entire experiment period as shown in Figure 4.3.

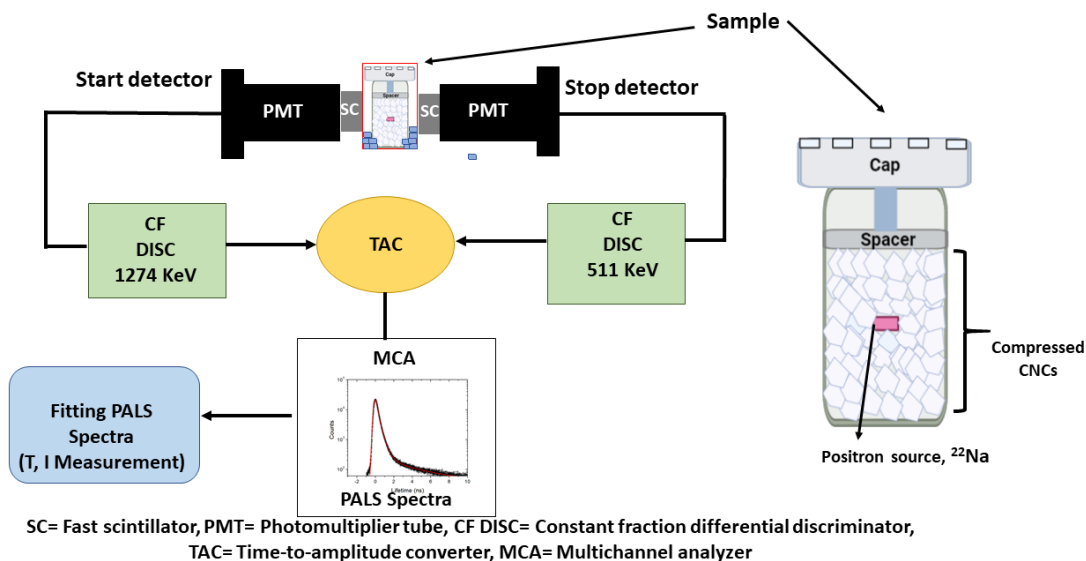


Figure 4.3 Experimental setup for PALS measurement.

Positron annihilation studies were performed on an ORTEC fast-fast coincidence system. The vial containing CNC samples and positron source, was placed between the two detectors to acquire a lifetime spectrum. Each spectrum was collected to 1 million counts of annihilation events. The resolution function was determined to be 331 ns and was obtained using a copper standard. The spectrum was fitted to three exponential components for their respective lifetimes and relative intensities, using the PALSFIT program. The first (τ_1) and second (τ_2) components are associated with *para*-positronium (p-Ps) and bulk positron annihilations, respectively. The long-lived third (τ_3) component and its relative intensity (I_3), were associated with the annihilation of *ortho*-Positronium (oPs) trapped in the holes and was sensitive to the structural changes induced by

alignment of the CNCs. The lifetime (τ_3) of the positronium can be correlated to the size of the pore or free volume cavity using the Tao-Eldrup model expressed as:

$$\tau_3 = 0.5 \left[1 - \frac{r}{r + \Delta r} + \frac{1}{2\pi} \sin \left(\frac{2\pi r}{r + \Delta r} \right) \right]^{-1} \quad (4.5)$$

where r represents the radius of a spherical free-volume pore and $\Delta r = 0.166$ nm [140]. I_3 represents the relative number density of free volume. The fractional free volume (FFV) of the system can be calculated as [147]:

$$FFV = C \times I_3 \times \frac{4}{3} \pi r^3 \quad (4.6)$$

where, C is an arbitrarily scaling factor, and considered as $C = 1.5$ for a spherical cavity.

4.3 Results and Discussions

4.3.1 Alignment of CNCs within Films

As shown in Figure 4.4, the self-organized CNC film exhibited the typical iridescence which is associated with chiral nematic organization of CNCs. In contrast, the shear-oriented CNC film is transparent without having any light interference. The degree of order of CNC alignment within self-organized (chiral) and shear-oriented (aligned) CNC films was measured via UV-Vis spectroscopy with birefringence used to determine Herman's order parameter. As shown in Figure 4.4, the optical images of self-organized CNC film for both 90° and 45° configurations exhibited similar dark and bright speckled regions due to the chiral nematic domains. Hence, both directions showed similar transmitted light intensity and the Herman's order parameter for chiral nematic films was nearly zero ($S=0.08$), which confirms the random distribution of the chiral nematic domains. A similar observation was reported in Diaz *et al.* (2013) [129]. As the CNCs domain in the films are organized in a random fashion, the in-plane properties of the films should be isotropic [129,144].

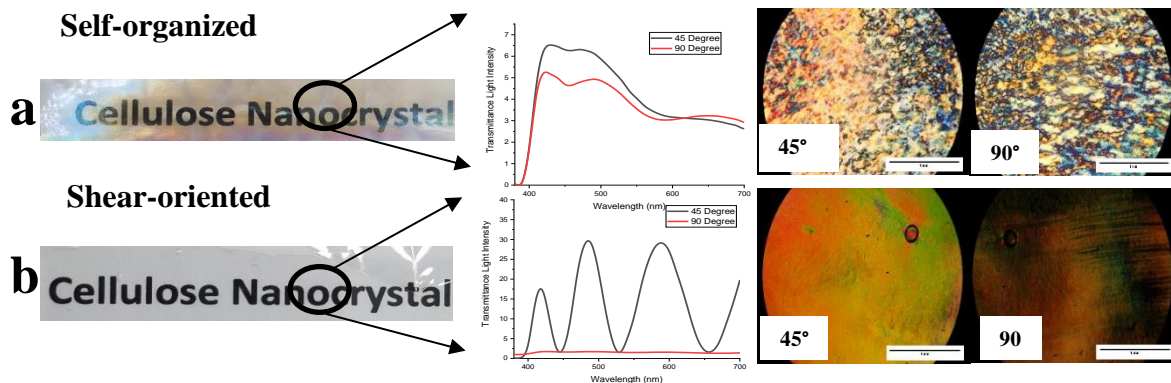


Figure 4.4 (a) self-organized, and (b) shear-oriented CNC films with light transmittance value and optical microscopy images.

In contrast, shear-oriented CNC films exhibited significant difference in peak intensity of transmitted light for the 90° and 45° configurations. The Herman's order parameter (S) value of shear-oriented films was 0.75. This is because when a shear was applied on the CNC suspensions, the CNCs flow in the shear direction and order into an anisotropic film with a higher Herman's order parameter.

4.3.2 Free volume of self-organized and shear-oriented CNC films

PALS is an established technique to determine the free volume structure of a polymer matrix. Recently, this technique has been successfully employed for the investigation of free volume structure of interfacial layers in polymer nanocomposites [138,139,148]. These studies have reported that o-Ps is efficiently trapped in the free volume nanoholes at interfacial layers of polymer nanocomposites. The oPs pickoff lifetime (τ_3), and its intensity (I_3) can be well correlated with the size and density of nanoholes in polymer nanocomposites. The pickoff lifetime provides an indication of the mean free volume cavity radius and the corresponding intensity (I_3) parameter is a measure of the relative number of free volume cavities.

Table 4.1 o-Ps Characteristics, Pore Radii, and fractional free volume for self-organized and shear-oriented CNC films.

Sample	o-Ps lifetime (τ_3) ns	Radius of pore (r) nm	I ₃ %	Fractional Free Volume (FFV) %
Self-organized	1.763±0.039	0.264±0.0044	10.705±0.017	1.234±0.06
Shear-oriented	1.644±0.0272	0.252±0.000028	10.330±0.025	1.041±0.03

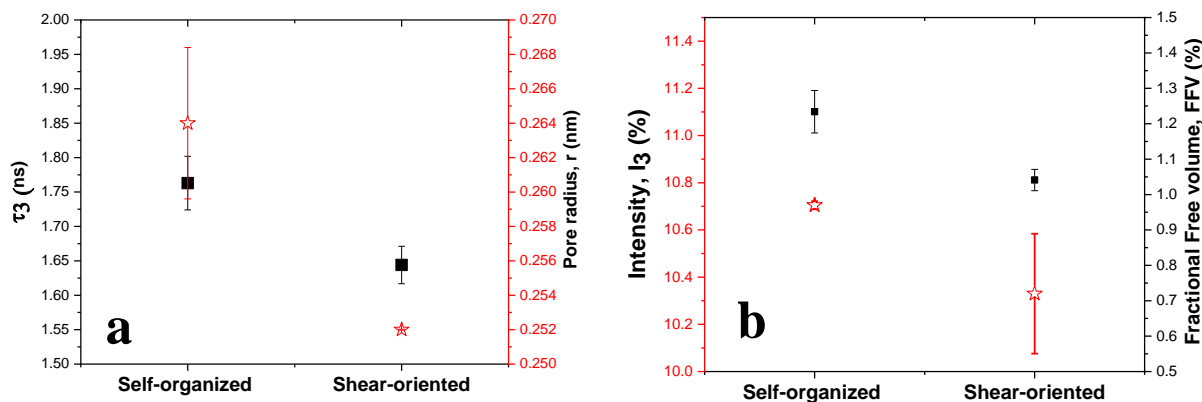


Figure 4.5 (a) O-Ps lifetime (τ_3) and pore radius (r), (b) O-Ps intensity (I₃) and fractional free volume (FFV) of self-organized and shear-oriented CNC films.

In this study, the PALS spectra were analyzed by PALSFit software to calculate the o-Ps lifetime (τ_3), pore radius and relative fractional free volume of self-organized and shear-oriented CNC films. In self-organized CNC film, the CNC crystalline domains are in a cholesteric phase where each plane (local order) is rotated by a phase angle, which makes them lower packing density ($\rho = 1.45 \text{ g/cm}^3$) with higher free volume [137,141]. In contrast, individual CNC oriented in the shear direction maintaining minimum intra- and inter crystals distance for shear-oriented CNC film resulted in higher packing density ($\rho = 1.55 \text{ g/cm}^3$) [137,141]. As shown in Table 4.1 and Figure 4.5, o-Ps lifetime for self-organized CNC films (1.763 ns) is significantly higher than that of shear-oriented CNC films (1.644 ns), suggesting that shearing the CNC suspensions increased the alignment of CNC domains which reduced the free volume within the films. Furthermore, the pore radius (r) of self-organized films is 0.264 nm while for shear-oriented films is 0.252 nm. Applying shear on CNC suspensions not only influenced the pore radius but also significantly reduced the population of pore and overall free volume of the films. Figure 4.5 shows

the variation of number of free volume sites (I_3) and fractional free volume (FFV) of self-organized and shear-oriented CNC films. Population of available free volume for self-organized and shear-oriented CNC films are 10.71% and 10.33%, respectively. In addition, shear-oriented CNC film (1.041%) has 16% lower fractional free volume as compared to chiral nematic CNC film (1.234 %).

4.3.3 Effect of alignment on gas barrier performance of CNC films

The transportation of gas molecules through polymeric systems follows the solution-diffusion mechanism which consists of three steps: 1. the absorption or adsorption of gas molecules at the upstream (high pressure) region; 2. diffusion of gas molecules through the membrane; and 3. desorption or evaporation from downstream (low pressure) regions. These solution-diffusion mechanisms are mostly controlled by the difference in thermodynamic activity at the upstream and downstream faces of the polymer films as well as the interaction between the polymers and gas molecules. Thus, the gas barrier performance of a polymeric system depends upon the solubility and diffusivity of the gas molecules. The diffusivity of the gas is the kinetic part of the solution-diffusion model and depends on the size of the gas molecules, degree of crystallinity, axial ratio of nanomaterials, and importantly in this case, existing free volume of the system. [10,149–151]. Free volume in a system is the main diffusion path for the transportation of the gas molecules. Furthermore, gas molecules having higher kinetic diameter need higher activation energies for the formation of transient holes in polymers for the diffusion process [152]. Typically, oxygen gas has lower permeability than carbon dioxide as the kinetic diameter of oxygen and carbon dioxide are 0.346 and 0.33 nm, respectively [153].

As shown in Figure 4.6, the oxygen permeability (P_{O_2}) of shear-oriented CNC film ($1.48 \times 10^{-16} \text{ cm}^3 \cdot \text{cm} / \text{cm}^2 \cdot \text{s} \cdot \text{Pa}$) with an order parameter of 0.75 was 95% lower than that of self-organized chiral nematic CNC films ($2.91 \times 10^{-15} \text{ cm}^3 \cdot \text{cm} / \text{cm}^2 \cdot \text{s} \cdot \text{Pa}$). Furthermore, the P_{CO_2} for self-organized and shear-oriented CNC films are 1.07×10^{-14} and $4.21 \times 10^{-16} \text{ cm}^3 \cdot \text{cm} / \text{cm}^2 \cdot \text{s} \cdot \text{Pa}$, respectively. Similar to oxygen permeability, the carbon dioxide permeability was also reduced by 96% after increasing the alignment of the CNCs, although overall at a higher level. As explained by Chowdhury *et al.* (2019), generally P_{CO_2} will be higher as compared to P_{O_2} for both types of CNC films due to the stronger interaction between CO_2 and CNCs and smaller kinetic diameter of CO_2 over O_2 [137].

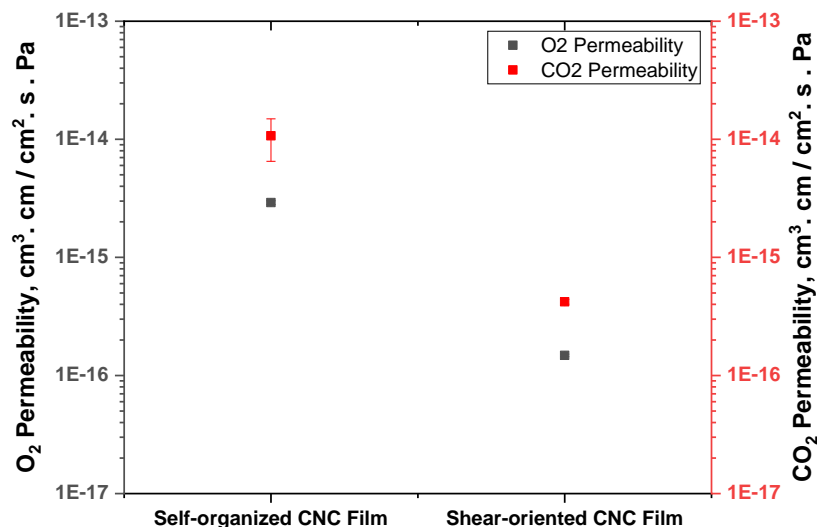


Figure 4.6 Oxygen and carbon dioxide permeability of self-standing (chiral) and shear oriented (aligned) CNC films.

Overall, while the O₂ and CO₂ permeabilities of aligned CNC films were similar to that reported by Chowdhury *et al.* (2019), the permeability of chiral nematic (self-organized) films of this study was found to be lower than previously reported [137]. One of the possible reasons for higher permeability of chiral nematic CNC films reported by Chowdhury *et al.* may be the presence of invisible micro-cracks. As Chowdhury *et al.* used self-standing films for measuring the permeability, it is believed that cutting the brittle chiral nematic CNC films to size and applying high pressure to seal the permeation cell induced micro-crack that were not clearly visible. In contrast, here, chiral nematic CNCs were coated onto PP polymer film which increases flexibility and reduces the possibility of inducing micro-cracks.

4.3.4 Comparison of barrier performance of CNC films with other commercial polymers

As shown in Figure 4.7 and 4.8, the fractional free volume significantly influences the gas barrier performance of polymers. It is expected that polymers with high free volume density and size will have higher gas permeability due to the enhanced gas diffusion through the free volume holes. The fractional free volume in polymers largely depends on polymer chemistry, crystallinity, rigid amorphous fraction (the amorphous component that is restricted between crystalline lamella), and mobile amorphous fraction (the bulk amorphous component that separates the lamella stacks)

[147]. Free volume and density of holes in the rigid amorphous fraction is higher than that of the mobile amorphous fraction. The dominant hole size controls the diffusion process, whereas the density of free volume controls the solubility of gaseous molecules [154]. As shown in Figure 4.7, the PVOH and EVOH have lowest free volume and higher barrier performance as compared to other engineering polymers like HDPE, PP, polymethyl methacrylate, PVC etc.

Both self-organized and shear-oriented CNC films have lower free volume although their barrier performance differs significantly. Self-organized chiral nematic CNC film belongs to the moderate barrier region while shear-oriented CNC film is categorized as excellent barrier films. Shear-oriented CNC film has 15- and 5-fold higher oxygen barrier performance as compared to PET and EVOH polymer films. Due to higher barrier performance, shear-oriented CNC can be coated on low barrier commercial polymer films like PE, PP, and PLA to improve the barrier performance.

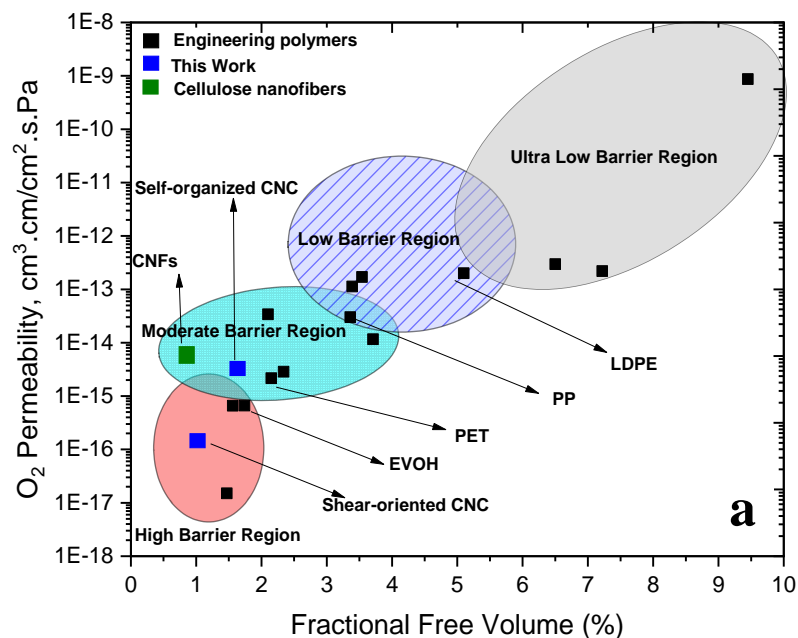


Figure 4.7 Plot of oxygen permeability of cellulose films as a function of relative free volume and comparison with other engineering polymers. Details of quantitative data for this plot can be found in Table C2.

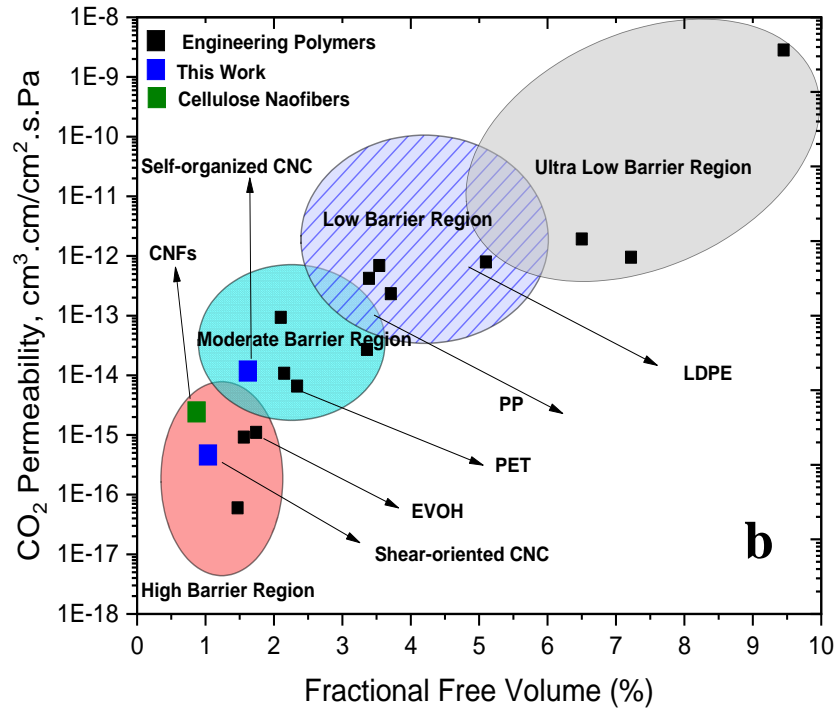


Figure 4.8 Plot of carbon dioxide permeability of cellulose films as a function of relative free volume and comparison with other engineering polymers. Details of quantitative data for this plot can be found in Table C2.

4.3.5 Dil model for the prediction of gas permeability

The Bharadwaj model was developed to fit gas permeability through nanocomposites of impermeable anisotropic nanomaterials in a permeable polymer matrix and does a good job of modelling order induced diffusivity changes [Equation 4.7] [151]. Based on this model, the relative permeability of a polymer nanocomposite (P_c) and its corresponding polymer matrix (P_m) is given by:

$$\frac{P_c}{P_m} = \frac{1 - \phi_s}{1 + \frac{L}{2W} \phi_s \left(\frac{2}{3}\right) \left(S + \frac{1}{2}\right)} \quad (4.7)$$

where ϕ_s , L , W , and S represent the volume fraction, length and width of the filler materials, and Herman's order parameter, respectively.

In a previous study by the authors here, the Bharadwaj model was modified for application towards a single component CNC system by assuming the CNCs themselves were impermeable and the “matrix” was free volume between the CNCs [137]. The “concentration” of nanoparticles (CNCs) in the matrix (free volume) was estimated based on density of the films as related to the theoretical density of crystalline cellulose and was dependent upon the order parameter of the system. However, this approach has some limitations for predicting the permeability of gas molecules through CNCs films. Among the several limitations, one of the most important flaws was that the model considers the anisotropic material to be a perfect rod-shaped particle. However, generally the shape of anisotropic nanomaterials ranges from perfect rod shape to nanoplatelet. Hence, experimental data can show significant deviation from the Bharadwaj model. To overcome this limitation, Dil *et al.* modified the Bharadwaj model by considering the particle shape of the nanomaterials for the model [143] as:

$$\frac{P_c}{P_m} = \frac{1 - \phi_s}{1 + \frac{L\phi_s}{2W} \left(1 - \sqrt{\frac{2}{3}(1 - S)} \right)} \quad (4.8)$$

Cellulose nanomaterials can have different aspect ratios based on the source of materials and chemistry of the extraction process [155]. In this work, CNCs with high aspect ratio was used for the film fabrication. The shape of the anisotropic nanomaterials is not a perfectly rod-like structure (see Supporting Information for TEM image). Moreover, nonuniformity in the width was observed in individual crystalline domains as these materials have significant dispersity. Therefore, the experimental data is expected to have some deviation in any modified Dil model due to the base Bharadwaj model from which it is derived. Thus, in a similar manner as before, the Dil model was modified for the single component CNC system by considering CNCs as the impermeable nanoparticle and interstitial free volume as the matrix, with the effective loading fraction determined by the relative density as compared to the theoretical crystalline cellulose density (Equation 4.9 and 4.10). The length and width of the CNC was considered as 100 and 5 nm for predicting the relative gas permeability. The experimental data was then compared to both the modified Bharadwaj model and modified Dil model.

$$\frac{P_{anisotropic}}{P_{chiral}} = \frac{1 - \phi_{anisotropic}}{1 + \frac{L\phi_{anisotropic}}{2W} \left(1 - \sqrt{\frac{2}{3}(1 - S)} \right)} \quad (4.9)$$

$$\phi_{anisotropic} = \frac{X(m/d_{anisotropic})}{(X(m/d_{anisotropic})) + Y(m/d_{chiral})} \quad (4.10)$$

where, $\phi_{anisotropic}$, L and W represent the volume fraction of anisotropic phase of the CNC film, length of CNCs and width of CNCs.

The relative permeability data for the CNC films here (along with some previously published data to fill in gaps) is shown in Figure 4.9 plotted as a function of their respective Herman's order parameters. The modified Dil model and modified Bharadwaj model are fitted to the data. For our modified Dil model system, the experimental data was calculated based on the chiral nematic CNC ($S=0.08$) system considered as a totally isotropic system ($S=0$), although there is local alignment as discussed earlier. In the previous work by the authors, aligned CNC film data fit the modified Bharadwaj model reasonably well if the $S=0$ state (the unity criterion) was regressed from the aligned data rather than using the chiral nematic as the initial state. However, if the chiral nematic state was taken as the "isotropic" state, the fits were much poorer. This was attributed to the microscopic structural differences between aligned and chiral nematic – that is, while chiral nematic is globally isotropic, it is not disordered. However, as stated earlier, the anomalously high permeability for the chiral nematic free standing films may be in fact due to unobservable microcracks due to stresses in the films. Thus, the data was replotted and fit using the chiral nematic film as the initial state.

With the new chiral nematic data, the prediction of relative permeability data of the modified Bharadwaj model fit much better to experimental data although some deviation was observed for CO_2 gas system, likely due to the complex quadrupolar nature of CO_2 . Further, the modified Dil model also fits the data reasonably well. Of course, in this case, the models differ only slightly with the modified Dil model predicting a very small higher relative permeability than the modified Bharadwaj model. The predicted relative permeability value (Table C3 in Appendix C) for oxygen gas from modified Bharadwaj model has 27-47% error when compared with experimental value. In contrast, only 3-6% error was observed for modified Dil model with the exception of high Herman's order parameter, although neither model predicted well there with both ~50% off of the actual value. On the other hand, both models did a poor job of predicting carbon dioxide permeability value with high accuracy. This being the case, overall, it seems in the absence of specific chemical interaction knowledge, that the modified Dil model fits O_2

permeability better while the modified Bharadwaj model fits the CO₂ permeability better, and both do an excellent job of relative performance prediction.

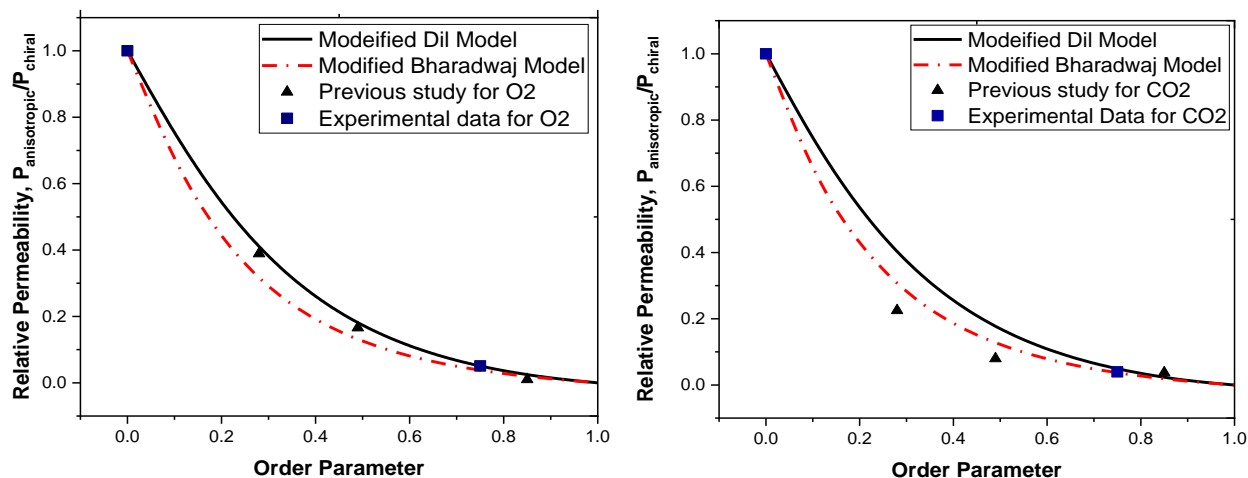


Figure 4.9 Comparison of the modified Dil and modified Bharadwaj model with experimental permeability data for oxygen and carbon dioxide.

4.3.6 Summary

The main objective of this study was to measure the free volume of CNC films and correlate this data with order parameter and gas barrier performance. The study showed that shear-aligned CNC films have lower free volume size and density as compared to self-organized CNC film (chiral nematic) due to the alignment of individual CNCs in shear direction. As free volume dictates the transportation of gas molecules and alignment enhance the path tortuosity, the aligned CNC film exhibits excellent barrier performance. Furthermore, compared to chiral nematic CNC film, aligned CNC film has 95% and 96% higher O₂, and CO₂ barrier performance, respectively. The Bharadwaj model as modified by Dil can further be modified for a single component CNC film and was utilized successfully to predict gas permeability with variation in order parameter of the film. Overall, the supported film permeability data better fit models than previously due to sample quality in the chiral nematic film. The modified Dil model is more accurate to actual data for O₂, but less accurate than CO₂ as compared to a modified Bharadwaj model, although both models do a good job of relative performance fitting.

CHAPTER 5. GAS AND WATER VAPOR BARRIER PERFORMANCE OF CELLULOSE NANOCRYSTALS-CITRIC ACID COATED POLYPROPYLENE FILM FOR FLEXIBLE PACKAGING

All research work except AFM experiment was performed by Md Nuruddin. All analysis was performed by Md Nuruddin with guidance by Prof. John Howarter and Jeffrey P. Youngblood. All writing was performed by Md Nuruddin with guidance and editing by Prof. John Howarter and Jeffrey P. Youngblood.

5.1 Introduction

Barrier properties represent the ability to restrict the transport of gases, vapors, and liquids from the outside environment into the packaging system or vice versa. The polymers used for food packaging, directly or indirectly, has severe requirements as the quality, odor, and taste of the food can be affected because of the transportation of gases, liquids, and vapors (water or organic). Further, transportation of vapor or liquid either from the interior (e.g. food) or the outside environment can cause plasticization of a polymer barrier material, which in turn may lead to increased permeability of gases and vapors [156]. Loss of water from the food causes an undesirable drying of the products while gaining moisture from surroundings may lead to microbial activity which results in the spoiling of the food. Oxygen accelerates lipid oxidation and stimulates rancidity of the foods [157]. For carbonated drinks, the loss of CO₂ has a detrimental effect on the shelf life of products. Thus the packaging materials should have excellent barrier properties for CO₂ transportation [158].

Polymers have drawn widespread attention as an alternative to traditional materials like metals and glass for packaging applications due to their desirable properties such as flexibility, toughness, chemical resistance, low density, formability and low cost. A key difference between polymers and other materials like glass and metals, is that metals and glass are excellent barriers to the transportation of small molecules like gases, water vapors, organic vapors, in addition to aromas, additives, and flavors, while polymers are generally permeable to gases and vapors to a much larger degree [156,159].

Generally, while a variety of polymers are utilized as packaging materials, polyolefins, such as polypropylene (PP), are most widely used for packaging applications because of their low-cost, high clarity, chemical inertness and excellent water barrier properties [105]. However, PP is

limited in its application as a single layer film for food packaging because of inherent poor oxygen and carbon dioxide barrier properties [160]. In general, PP films are coated with high oxygen barrier polymers like EVOH, PVDC and aluminum to enhance barrier performance or laminated or co-extrude with high barrier polymers [105–107]. However, these multilayer approaches lack sustainability as they make it impossible to recycle the finished product and these materials do not biodegrade.

Much attention has been given to cellulose nanocrystal (CNC) based films and coatings because of their renewability, low toxicity, biodegradability, and excellent barrier properties [161]. CNCs, rod-like cellulose nanoparticles, can be prepared by acid hydrolysis treatment of microcrystalline cellulose (MCC), micro-fibrillated cellulose (MFC), cellulose nanofibrils (CNF) or delignified cellulosic biomass [161–165]. Due to the high aspect ratio (3-5 nm wide and 50-500 nm in length) and crystallinity (54-88% crystalline depending upon source and reaction conditions), they have been utilized for polymer nanocomposites by solvent casting, melt extrusion or coated on other polymer substrate for packaging applications [163]. Recently, reports have shown that alignment of CNC films can increase film density by removing free volume between the CNC crystals, which leads to increased modulus, thermal transport, decreased expansion, and importantly here, extremely high oxygen and CO₂ barrier properties (superior to PVOH) [118,134,136,166,167]. Unfortunately, CNC films can be very brittle leading to cracking, which destroys the barrier behavior, and are very humidity sensitive, which limits applicability in packaging systems [168].

In this work, the food additive, citric acid (CA) is used as an additive to CNC films to induce plasticization and to improve hydrophobicity. It is hoped that this will prevent cracking and limit humidity-induced changes. Varying ratios of CA to CNC were coated as films on a polypropylene substrate and investigations were conducted to understand the effect of the CA on physical properties and barrier performance of CNC coating. The coated polypropylene films were characterized for oxygen, carbon dioxide and water vapor barrier performance, coated film's morphology and surface roughness.

5.2 Materials and Experiments

5.2.1 Materials

CNC aqueous suspension, 11.9 wt% containing 0.99 wt% sulfur on dry CNC (Batch# 014-FPL-065) was purchased from the University of Maine (Orono, Maine, USA), and manufactured by the US Department of Agriculture Forest Service-Forest product laboratory (Madison, Wisconsin, USA). The average particle length and width (based on TEM image) were 100 ± 25 nm and 5 ± 1.5 nm, respectively [Appendix D, Figure D2]. The average zeta potential and crystallinity index for CNC suspensions was -47 ± 2 mV and 85.5 %, respectively [Appendix D, Figure D3-D4 and Table D1]. Polypropylene flexible film of 18-micron thickness (trade name: Bicolor™ 70 HSH) was supplied by Jindal Film (LaGrange, GA, USA), used as a substrate for anisotropic CNC coatings. Citric Acid (ACS reagent, $\geq 99.5\%$) was purchased from Sigma Aldrich.

5.2.2 Preparation of coating

The 10 wt% CNC suspension was prepared by diluting the 11.9 wt% CNC suspension with ultrapure water. Ultrapure water (>18.0 MOhm-cm) was obtained from a Barnstead™ system. A 10 wt% citric acid solution (dissolved in water as before) was then added to the 10 wt% CNC suspensions with varying quantities of 5%, 10%, 15%, 20% and 25% respectively, as shown in Table 5.1 to achieve the final suspension of 10% solid content. After addition of the CA, all coating formulations were ultrasonicated (Branson Ultrasonics, Danbury, CT, USA) for 3 min (at 10% amplitude with a 10s plus and 10s rest at 60 Hz frequency) to uniformly disperse the CNCs suspension and homogenize solution.

Table 5.1 Chemical ingredients and amounts used to prepare barrier coatings

Sample Name	CNC (%)	Citric Acid (%)
100CNC	100	0
95CN-5CA	95	5
90CN-10CA	90	10
85CN-15CA	85	15
80CN-20CA	80	20
75CN-25CA	75	25

5.2.3 Application of Coating

The surface tension of the CNC and CNC-CA suspension (was higher than surface energy of the polypropylene film substrate [Appendix D, Table D2]). To compatibilize the substrate and coating system, the polypropylene surface was corona treated for 5-6 times using BD-20AC Laboratory Corona Treater (Electro-Technic Products, Chicago, USA). Immediately after the corona treatment, CNC and CNC-CA coatings were applied on polypropylene thin films using a K Hand coater (Bar No. 2, wet film thickness 12 micron) from Testing Machines Inc. (New Castle, DE, USA) (Appendix D, Figure D5). The coated films were immediately transferred to the oven maintained at 60 °C and kept for 20 min to complete the drying process. The dried coated films were kept in a desiccator at 0-5%RH until required for further characterization.

5.2.4 Wet coating properties

Surface tension of the CNC-CA coating formulations was measured by pendant drop tensiometer, using a Ramé-Hart contact angle goniometer (Ramé-Hart Inc., NJ, USA) with DROP Image Advanced software. A small drop of liquid (10-15 μ l) was suspended from a teflon tip (volume 30 μ l) into the air under room temperature. Ten measurement of the surface tension was taken with 30 seconds per measurement, and the average value was reported as a final measurement of the surface tension.

Rheology measurements of the CNC and CNC-CA formulations were carried out using a Malvern Bohlin Gemini HR Nano rheometer according to the standards specified in DIN 53019-1. A cup and bob fixture with a vertical gap of 150 μ m was used. Before starting the measurement, the samples were pre-sheared at 100 s⁻¹ for 60 s and then left to equilibrate for 120 s. Shear flow behavior measured with a shear rate ramp of 0.1–500 s⁻¹ with 30 s per data point.

5.2.5 Characterization of Coated Films

The cross-sectional images of the coated PP were obtained using a Phenom ProX desktop SEM (PHENOM WORLD, Netherlands). The samples were sputter-coated with a thin layer of gold. The images were investigated using ImageJ software to measure the thickness of the coating layers. About 20 measurements from five images were investigated for each coated film, and average value was reported as the thickness of the coated films.

Samples of dimension 10 mm × 10 mm (length× width) were immersed in the 20 ml glass vials containing water and kept in the oven at 80 °C for 3 hours. Then, the samples were taken out of the vials, and wash with distilled water to remove residual coating materials from the PP substrate. The samples were then dried in the oven at 80°C for 6 hours. Weights of the dried samples were measured. The coat weight of the coating was calculated by Equation 5.1:

$$\text{Coat weight} = \frac{W_{\text{coated}} - W_{\text{uncoated}}}{\text{Area of the sample}} \quad (5.1)$$

The transparency of the CNC and CNC_CA coated PP films were investigated using a conventional UV–Vis spectrophotometer (Spectramax Plus 384, Molecular devices Corp., 133 Sunnyvale, CA) in the wavelength ranges from 200 to 750 nm with air as the background.

5.2.6 Barrier Properties of the Films

The permeability of O₂ and CO₂ gas were investigated at room temperature using a constant-volume/variable-pressure permeation system [Appendix D]. Polymer films with 25 mm diameter were cut precisely with high precision scissors. The film was inserted inside a Millipore stainless steel high-pressure sample holder (Millipore Sigma, MA, USA) with an exposed transportation area of 2.7 cm². The entire permeation system was maintained at vacuum for 12 hours to remove entrapped air and moisture from the films and then the valves connecting the film holder were closed to prevent entering air during the entire experiment. The slow increments in pressure over time in the downstream volume due to leakage of the system (the leak rate) was measured. For measuring the permeability, the feed gas (O₂, CO₂) was introduced to the upstream side at a fixed pressure and the pressure rise in the downstream volume as a function of time was measured.

The gas permeability (P_{O₂}, P_{CO₂}) of the films was calculated using the following expression [169]:

$$P = \frac{V_d l}{P_2 A R T} \left[\left(\frac{dp}{dT} \right)_{ss} - \left(\frac{dp}{dT} \right)_{leak} \right] \quad (5.2)$$

Where, V_d(cm³) is the downstream volume (volume of tank and tube), l is the film thickness (cm), P₂ is the upstream absolute pressure (cmHg), A is the film's exposed area for gas transportation (cm²), R is the gas constant (0.278 cmHg cm³/[cm³(STP)K], and T is absolute temperature (K).

Furthermore, $(\frac{dp}{dt})_{ss}$ and $(\frac{dp}{dt})_{leak}$ are the steady state pressure rise in the downstream volume during leak testing and gas permeation through the films.

The gas permeability of the CNC coated layer was calculated using the following expression:

$$P_c = \frac{h_c}{\frac{h_1}{P_1} + \frac{h_2}{P_2}} \quad (5.3)$$

Where P_c , h_c , P_1 , P_2 , h_1 , h_2 are permeability of CNC coated PP, thickness of CNC-coated PP, thickness of PP substrate, thickness of CNC coated layer, and permeability PP substrate, respectively.

The water vapor transmission rate (WVTR) for CNC and CNC–CA coatings on PP substrate was measured according to ASTM-D1653 by a Gardco permeability cup of 10 cm² exposed area (Paul N. Gardner Company, Inc., FL). The test specimens were precisely cut into circular shape of 32 mm diameter with a precise scissor. The desiccant method was used for the WVTR measurement where a fixed amount of anhydrous CaCl₂ was placed in a dish covered with the test specimen. The edge of the disk was sealed with Neoprene and Teflon Gasket, and the assembly was placed in a climate-controlled chamber (23 °C, 90% RH). Water vapor transmission rate (WVTR) through the specimen into the desiccant was calculated by measuring the increase in the weight of the cup over the duration of the experiment. Every 24 hrs time period, the assembly was taken out of the controlled chamber and weighted. Water vapor transmission rate (WVTR) through the specimen into the desiccant was calculated by measuring the increase in weight of the cup over the duration of the experiment. The average value of three parallel measurements for each specimen was reported in g/m² day.

5.2.7 Contact Angle Measurement

Contact angle analyses were performed using a Ramé-Hart Goniometer equipped with a video measuring system with a high-resolution CCD camera. Drop Image Advanced software was used for data acquisition. 60 X 20 mm² sized rectangular coated and non-coated PP films were fixed and kept flat throughout the analysis by a special type of sample holder. The contact angle between water and films was measured by the sessile drop method by gently placing a droplet of 4μL onto the surface of the films. The experiment was conducted at RT and 50% RH. The evolution of the contact angle was monitored starting from t=0 s to up to 10 min (t=600s) with an

interval of 10s. The images of water droplets onto films surface was captured at 10s, 5 min and 10 min, using a software-assisted image-processing system. A minimum of 5 droplets were examined for each film, and the data which is near the average value was presented graphically.

5.3 Results and Discussions

5.3.1 Wet Coating Properties

Surface tension plays a pivotal role in coating industry as the surface energy compatibility of ink and substrate is the main requirement for uniform and defect free coating. As shown in Figure 5.1, the surface tension of CNC suspension was 70.54 mN/m. With the addition of citric acid, surface tension decreased. The surface tension of the citric acid solution was 68.7 mN/m. For the CNC/CA mixture, the lower value of surface tension might be due to the tendency of lower surface tension component, in this case citric acid, to migrate towards the surface. As the PP substrate has a surface energy of 30 mN/m, there are only two options to compatibilize the substrate-ink system: (1) increase the surface energy of the substrate and (2) lower the surface tension of the formulations, such as through additive. As any additive may interfere with data analysis, increase of the surface energy of the substrate by conducting corona treatment was performed.

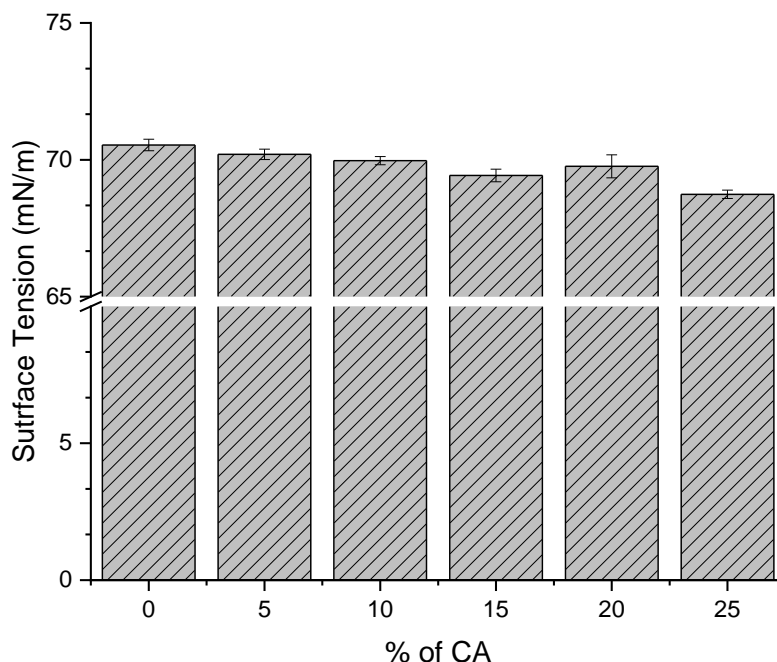


Figure 5.1. Effect of citric acid on surface tension of CNC suspensions.

Figure 5.2 shows the viscosity vs shear rate curves for CNC and CA coating formulations. The rheological behavior is important for coating procedures, as generally shear thinning behavior is desired [170,171]. However, for CNCs, a high zero shear viscosity or yield is also needed to prevent disorientation of aligned CNC film [172]. All solutions were shear thinning with multi-region behavior. The pure CNC suspension was higher in viscosity than CNC-CA formulations and showed a yield followed by a uniform linear decrease in viscosity indicating alignment of the CNC suspension after gel breakage. CA addition causes a change in phenomenology where overall viscosity is decreased at 10% CA and beyond, appearance of a small hump indicating a yield at low shear rate followed by two linear regions of power-law behavior. Interestingly, after a transition amount of CA at 5%, 10%, 15%, and 20% CA are essentially the same rheological behavior, and 25% CA decreases in viscosity. It is thought that CA act as a kind of “lubricant”, causing the surfaces of the CNCs to slip past each other more easily and is due to the CA preferentially interacting with the CNCs to interrupt CNC-CNC networking. This would lower yield and viscosity and likely happen at low contents, but once saturation of CNC surfaces occurs, little effect would be noticed until enough CA accumulates to affect the bulk liquid properties of the interstitial fluid. Importantly, this also indicates that both small amounts of CA may be needed and that the proper amount is likely in the 10-20% range, where the behavior is similar.

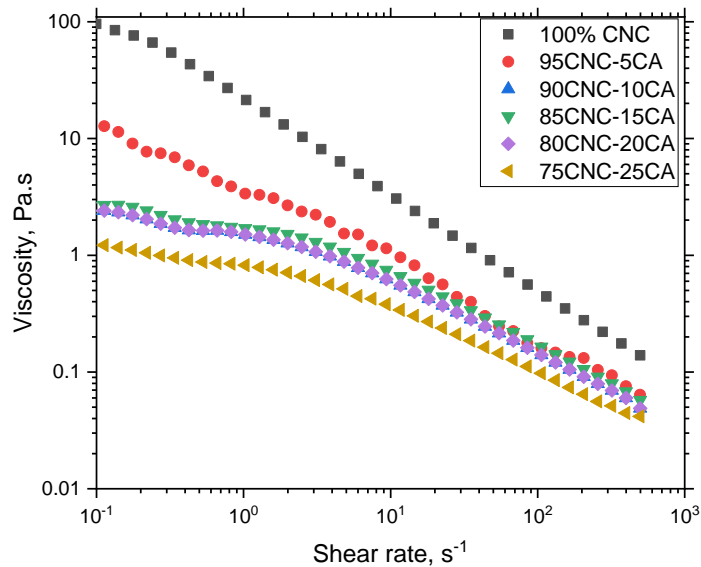


Figure 5.2 Steady-state viscosity vs shear rate for CNC and CNC-CA suspensions.

Furthermore, shear stress decreases at all ranges of the shear strain rate with increasing CA concentrations, indicating the lubricating effect of CA [Figure 5.3(a)]. The shear stress to shear strain rate relationship of the CNC and CNC-CA suspensions shows a typical shear thinning behavior, which is typically described in the Herschel–Bulkley model [equation 5.3] [173].

$$\tau = \tau_0 + K\dot{\gamma}^n \quad (5.3)$$

where τ is the shear stress, τ_0 the yield stress, $\dot{\gamma}$ the shear strain rate, K the consistency, and n the flow index. The flow index n is directly related with the shear thinning ($n < 1$) or thickening ($n > 1$) behavior of non-Newtonian fluid [174]. By fitting the shear stress-shear strain curve with the Herschel–Bulkley equation, the value of flow index can be obtained. As shown in Figure 5.3(b), the flow index value of pure CNC was 0.24 which is typical non-Newtonian fluid showing shear thinning behavior. As discussed earlier, the origin of shear thinning behavior is thought to occur as a result of alignment of CNC nanocrystals to flow direction. Addition of CA to the CNC suspensions increased the flow index value which further proved that CA lubricating the CNC surfaces, causing the surfaces of the CNCs to slip past each other more easily.

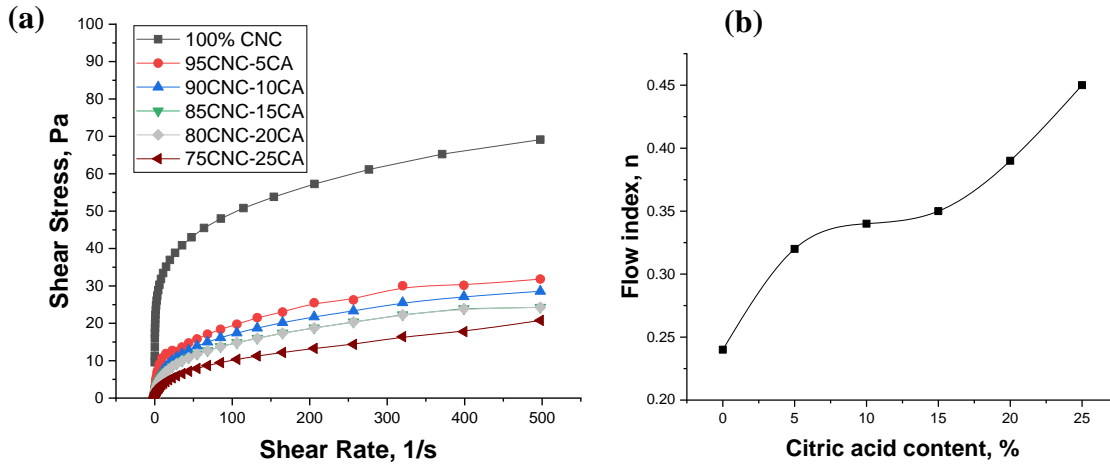


Figure 5.3 The shear stress and shear strain rate of CNC aqueous suspensions at different concentrations, (b) The relationship between the flow index (n) and CA concentration in CNC suspensions.

5.3.2 Coating Characterization

As coating all formulations had a constant (10wt%) solid loading, therefore, it is expected to have similar coating thickness and coating weight for each sample. However, theoretically the thickness of CNC-CA coated layer was supposed to be decreased, as the density of CNC

suspension (1.60 g/cm^3) is lower than CA (1.66 gm/cm^3) [175]. Furthermore, the addition of citric acid on the CNC suspension can significantly reduce the overall viscosity of the suspension that may influence the coating thickness by reducing the capillary number of the compositions [115]. Based on Figure 5.2, coating formulation with the highest citric acid must have the lowest capillary number. It is worth to mention that surface tension values were very close to each other for any coating formulations; hence, the capillary number should be independent of the surface tension. Therefore, coating thickness from the pristine CNC suspension should have higher coating thickness compared to any other coating formulations. As shown in Table 5.2, the coating thickness was decreased with the addition of CA into the coating formulations. Furthermore, no significant difference in coat weight was observed for all coating formulations, which is expected as solid content for all coating formulation was maintained as 10 wt%.

Table 5.2. Thickness, grammage and roughness of the CNC and CNC-CA coatings. Data are expressed as mean values \pm SD.

Sample	Thickness μm	Coat Weight g/m^2	Roughness nm
non-coated PP	-----	-----	7.23 ± 1.15
CNC-CA (100-0)	1.51 ± 0.14	1.33 ± 0.09	4.92 ± 0.77
CNC-CA (95-5)	1.33 ± 0.03	1.25 ± 0.10	6.21 ± 0.62
CNC-CA (90-10)	1.23 ± 0.05	1.32 ± 0.21	6.39 ± 0.58
CNC-CA (85-15)	1.12 ± 0.04	1.31 ± 0.15	6.40 ± 0.61
CNC-CA (80-20)	1.0 ± 0.06	1.26 ± 0.34	6.67 ± 0.32
CNC-CA (75-25)	0.88 ± 0.09	1.34 ± 0.48	6.69 ± 1.91

As shown in Figure 5.4, the surface roughness of the coated PP films was investigated using AFM images, and the root mean square values (Rq) are shown in Table 5.2. Coating of the PP with CNC reduced the overall roughness from 7.23 nm to 4.9 nm likely due to the aligned nature of the CNC film and strong self-association upon drying leaving few defects. Addition of CA exhibits higher roughness than pure CNC, although all CA-CNC coatings were similar. A possible reason for increased roughness after addition of CA into CNC suspension is the formation and aggregation of elliptical, spherical or spindle-shaped tactoids of CNCs at the surface of the film [172,176]. Alternatively, the aforementioned interaction of CA with the CNC surface shielding CNC-CNC interactions may be leading to less self-aggregation and defect formation.

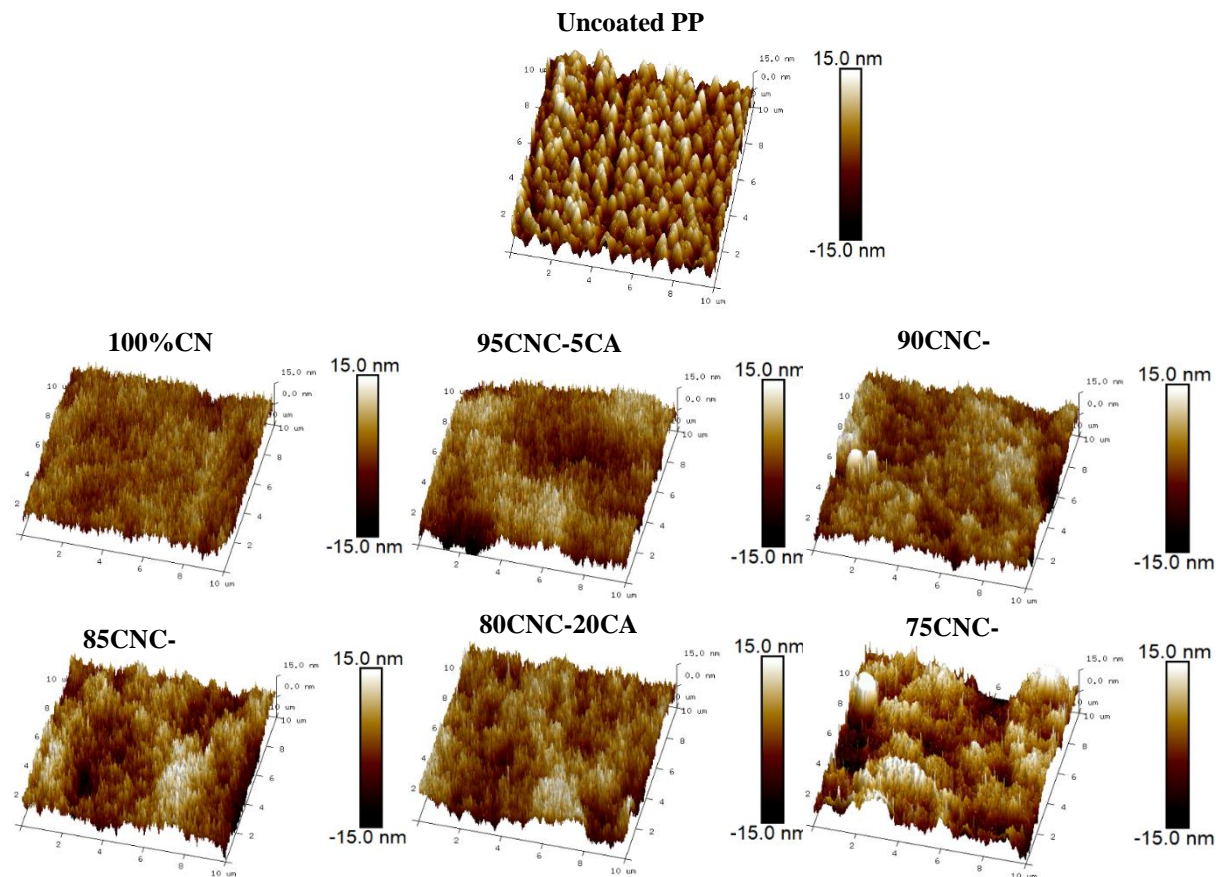


Figure 5.4 AFM 3D images (10 X 10 mm²) of uncoated and coated polypropylene (PP).

The optical transparency of uncoated and coated polypropylene films were investigated using UV-vis spectroscopy and shown in Figure 5.5. The uncoated PP films show excellent transparency of 94% in the visible region. Only ~2% transparency reduction could be observed for CNC coated PP films with CNC-CA coatings similar, which is likely due to the higher refractive index of the CNC coatings leading to more reflective losses [113]. Chowdhury et al. reported similar transparency loss of PET films after adding CNC coating [172]. These findings also suggest that CNCs have an excellent compatibility with CA as no aggregates on the size of light are scattering from either surface or bulk. Additionally, the coated films qualitatively exhibit low haze and high clarity as shown in Figure 5.5. This excellent transparency is a desirable feature of films for food packaging as a transparent film allows the packed product to be seen [177].

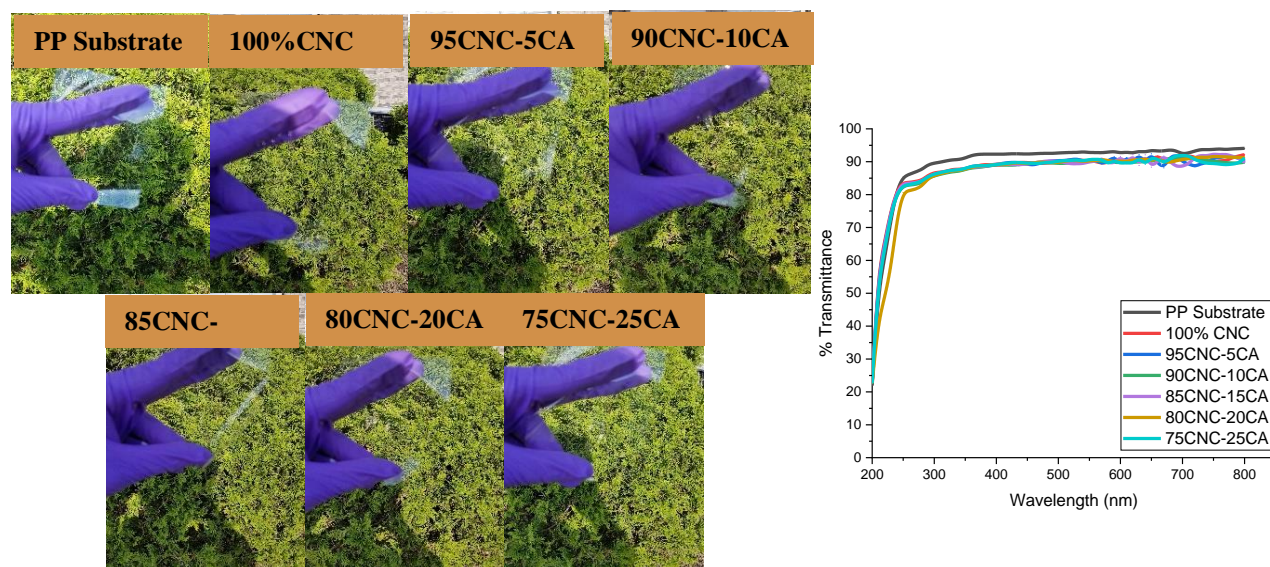


Figure 5.5 Optical transparency of CNC and CNC-CA coated PP films.

5.3.3 Contact Angle

To evaluate the surface hydrophobicity of the coated films, the contact angle with water was investigated. As shown in Figure 5.6, the uncoated PP surfaces are hydrophobic, having stable contact angle of 99.6° . In contrast, the coated layer surface exhibited hydrophilic character, showing unstable contact angle. The initial contact angle of CNC coated surface was 29° , and the value was rapidly decreased with time to a value of 14° . The CNC surfaces contain -OH groups, which is known to participate in extensive hydrogen bonding with water molecules. In contact with water molecules, the contact angle of water was decreased due to the sorption and swelling of the films, which caused unstable contact angle [178]. However, the hydrophobicity of the coated layer increased with the addition of CA. One possible reason is that the CA was H-bonded with the surface -OH groups of CNC and exposed their hydrophobic hydrocarbon chain on the surfaces. Thus, a reduction in the number of Lewis sites results in a decrease in the surface polarity of the CNC-CA coated films [179]. In addition, citric acid esterified some of OH-groups of CNC surfaces and occupy the free volume of the coated films which prevent them from water diffusion and swelling of film.

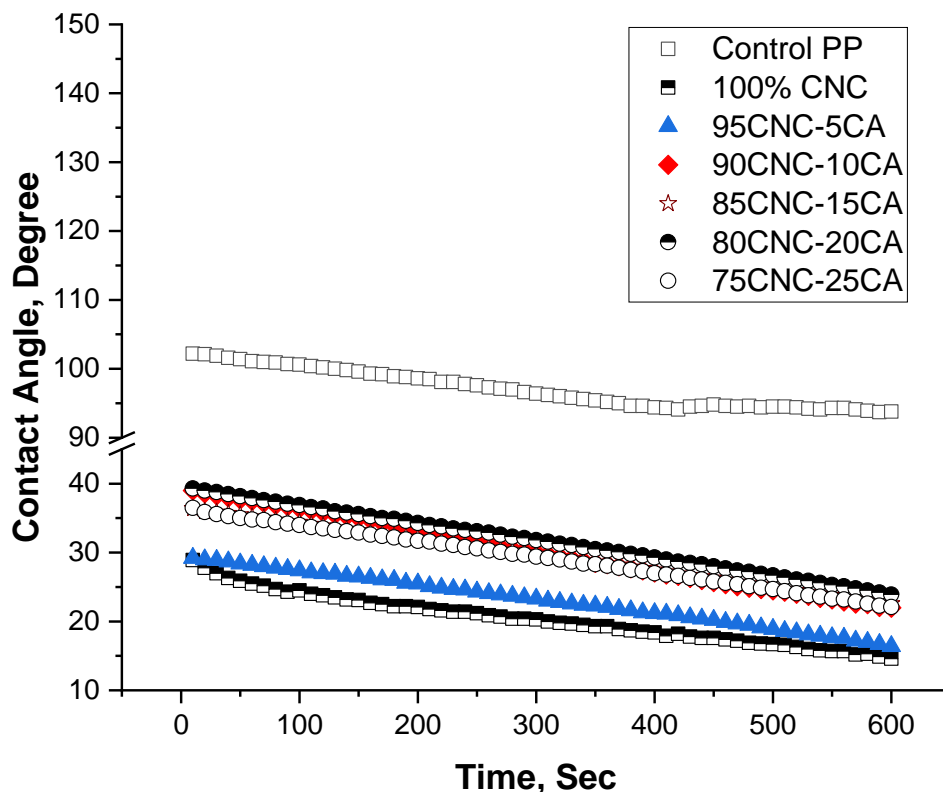


Figure 5.6. Variation of contact angle with time for uncoated and coated PP.

5.3.4 Barrier performance of coated films

As shown in Figure 5.7, the oxygen permeability (P_{O_2}) of pure CNC film was $2.62 \times 10^{-16} \text{ cm}^3 \cdot \text{cm} / \text{cm}^2 \cdot \text{s} \cdot \text{Pa}$, which is 4.5 times lower than high barrier PVOH and EVOH film. Interestingly, addition of CA to the CNC decreased the P_{O_2} as CA concentration was increased until a minimum was achieved at 20%CA in the CNC film, after which P_{O_2} increased again to the same level as pure CNC. Overall, addition of CA reduced OTR value to 70% of aligned CNC films. Furthermore, the CO_2 permeability (P_{CO_2}) of pure CNC film was $4.66 \text{E-}16 \text{ cm}^3 \cdot \text{cm} / \text{cm}^2 \cdot \text{s} \cdot \text{Pa}$, which is much lower than high barrier PVOH and EVOH film. Similarly, to P_{O_2} , P_{CO_2} was decreased as CA concentration was raised until a minimum was achieved at 20% CA in the CNC film, after which it went back up. However, in this case, P_{CO_2} was reduced quite a bit more by addition of CA where at 20% CA, P_{CO_2} was only 41% of the pure aligned CNC.

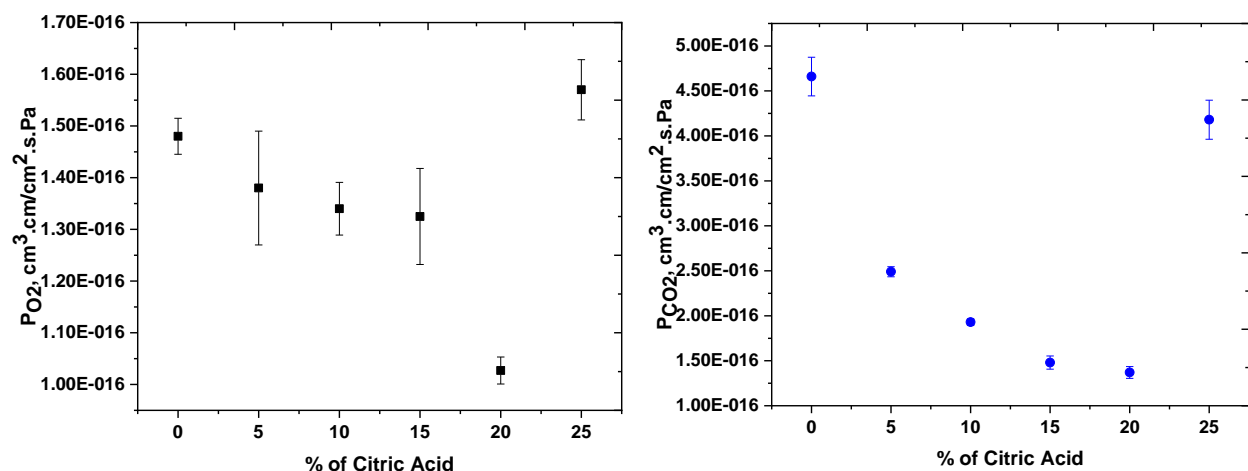


Figure 5.7 Oxygen and carbon dioxide permeability of CNC film with varying amount of CA.

Gas permeability is based upon the combination of diffusivity and the solubility of the gas molecules in the polymer, where the former depends on structural factors such as crystallinity, available free volume within polymers, and nature and kinetic diameter of the permeant gases and the former depends on the nature of the chemistry (e.g. hydrophobic vs hydrophilic) of the gas and polymer. The kinetic diameter of the permeant gases directly affect the transportation property through the polymer films [152]. A gas with higher kinetic diameter needs a higher activation energy for the formation of hole in polymers for their diffusion process [152]. Typically, the permeability of CO_2 is higher than O_2 as the kinetic diameter of oxygen is higher than that of carbon dioxide ($d_{O_2} = 0.346 \text{ nm} > d_{CO_2} = 0.33 \text{ nm}$) [153].

Gas molecules cannot pass through the individual CNCs as gas can only permeate through non-crystalline regions of the polymers, and therefore have a longer diffusion path (Figure 5.8). Chowdhury et al. (2019) reported that CNC films made with shear can have high packing density with lower free volume because of orientation of all CNCs in the same direction [180]. This anisotropic arrangement therefore enhances the tortuosity for gas diffusion that, coupled with the high polarity of the cellulose, led to a very low P_{O_2} and P_{CO_2} . Here, further improvement was achieved with the addition of citric acid (CA) up to 20% to the CNC suspension. It is probable that the added citric acid occupies what remaining free volume (pre-existing hole) is left and further increases the tortuosity of the system as shown schematic diagram (Figure 5.8). However, addition of 25% CA into the CNC suspensions, an increase the oxygen permeability is noted. Likely, there

is a critical percentage of CA loading where CA can saturate whatever pre-existing free volume there is among the CNC or may form intermolecular H-bond with CNCs with a minimal free volume. However, beyond this critical CA loading (20% CA in our study), CA may plasticize the coating system by increasing the free volume which would increase the permeability, increase the hydrophobicity of the overall film leading to higher solubility of the nonpolar oxygen and carbon dioxide, or may form discrete aggregates, although too small to scatter light. Whatever the reasons, it is clear that 20% citric acid in CNC is optimal.

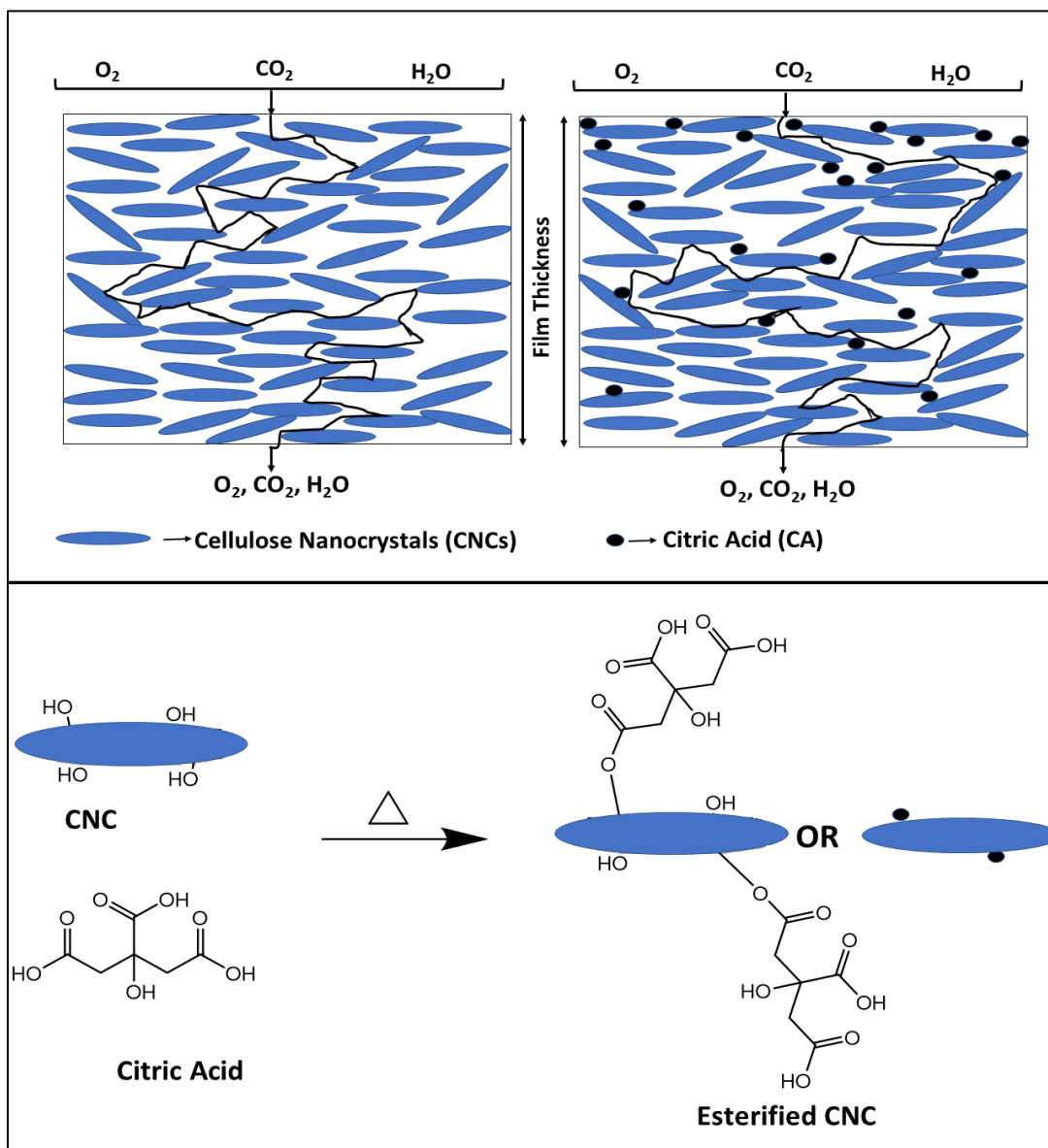


Figure 5.8 Schematic diagram of gas transmission through CNC and CNC-CA film.

It is also noted that addition of CA seems to reduce P_{CO_2} much more than P_{O_2} . CNC and CNC-CA coated PP films contains polar functional groups (-OH and -COOH). Therefore, nonpolar gases such as oxygen gas have little interaction with the CA/CNC coatings during sorption and diffusion steps. In contrast, while CO_2 is considered a hydrophobic gas, it does have a quadrupole moment. It may be that the dipole-quadrupole interaction between CO_2 and CA is higher as the polarity of the hydroxyl groups on CNCs is lower than the carboxylic acid groups found on CA. Furthermore, some of OH-group of CNC surfaces esterified which further reduces the CO_2 sorption (Figure 5.8).

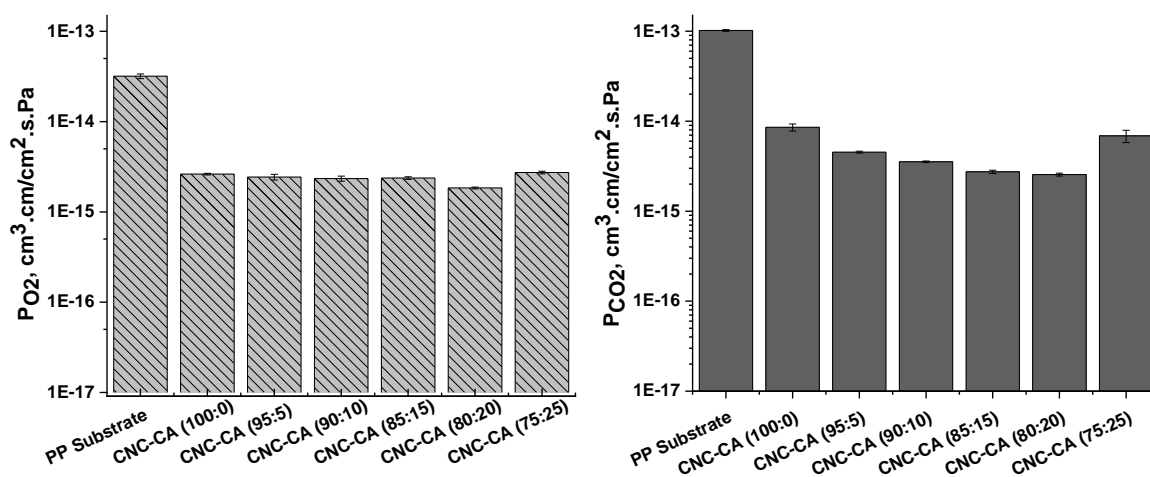


Figure 5.9 Oxygen permeability of CNC and CNC-CA coated PP films.

In addition, the oxygen permeability (OP) of un-coated PP films was 3.18×10^{-14} cm³.cm/cm².s.Pa as shown in Figure 5.9. Applying CNC and CA/CNC coating on PP films improved the oxygen barrier properties by 92% and 100%, respectively. Interestingly, the improvement of CO_2 barrier performance of coated PP was much higher as compared to O_2 barrier performance. However, CNC and CA/CNC coated PP has 92 and 99% reduction in CO_2 permeability as compared to uncoated PP films with a value of 1.02×10^{-13} cm³.cm/cm².s.Pa.

Low water vapor transmission rate (WVTR) as well as oxygen permeability of a packaging films are generally the two most important criteria for considering a barrier film. Similar to O_2 and CO_2 permeability, WVTR of a film depends on the packing density, existing free volume, hydrophilicity (polymer-moisture interaction) of the film, and crystalline-amorphous ratio.

Polypropylene itself is excellent moisture barrier films although it has low oxygen barrier performance. As shown Figure 5.10, the WVTR of uncoated PP was 2.2 g/m².24hr. CNC coating reduced WVTR significantly, which is surprising for such a highly polar polymer. However, it is likely that the high crystallinity of the CNC and low free volume due to alignment is reducing water transport. Addition of CA further reduced the WVTR down to a minimum achieved for coating of 80%CNC-20%CA formulation of about 1.3 g/m².24hr. While occupation of free volume as in the oxygen and carbon dioxide cases may be happening, the CA has also increased hydrophobicity of the CNC film, which may be further reducing WVTR.

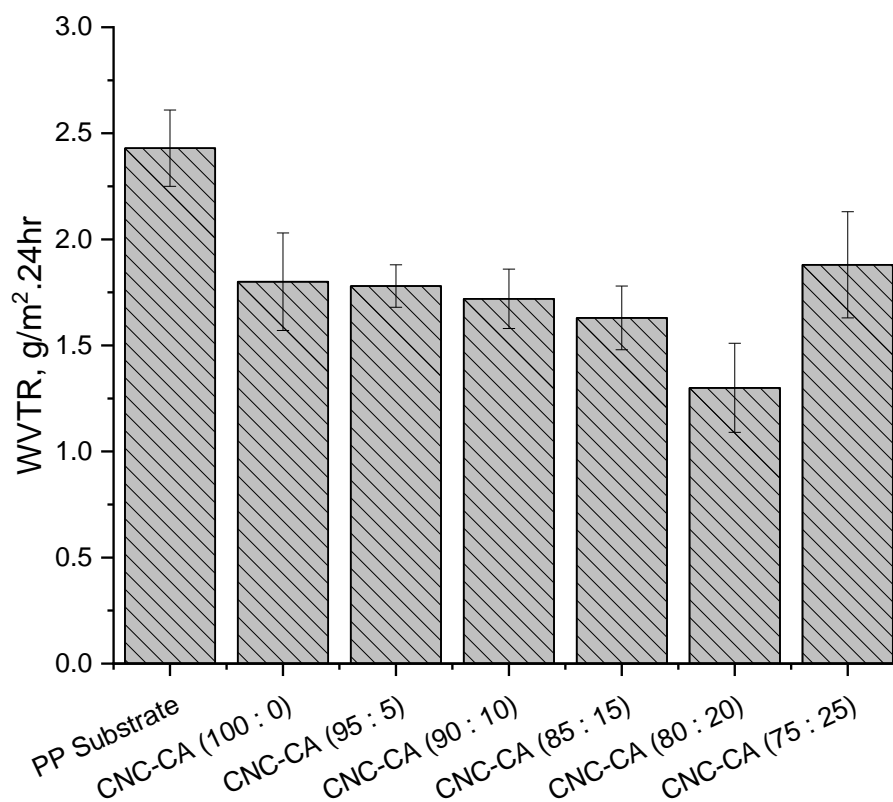


Figure 5.10 . Water vapor transmission rate (WVTR) of CNC and CNC-CA coated PP films.

5.3.5 Comparison of Barrier performance of CNC-CA coated PP with other commercial Polymers

As shown in Table 5.3, CNC and CA/CNC films has higher oxygen and carbon dioxide gas barrier performance of commercially available high barrier PVOH and EVOH films. Furthermore, CNC-CA coated PP films possesses high barrier performance for oxygen, carbon dioxide and moisture. While it is expected that the oxygen and carbon dioxide permeability values

of CNC-CA coated PP films are much lower than commercial low barrier substrate polymer films like HDPE, LDPE, and PLA, the “best” formulation here, 80CNC-20CA coated PP, had slightly better oxygen and much better (nearly an order of magnitude) carbon dioxide barrier performance than biaxially oriented PET film. Unfortunately, these coated PP are not quite as good as the “gold standard” oxygen barrier materials of polyvinyl alcohol (PVOH) and ethylene-vinyl alcohol copolymer (EVOH) having about 2X the transmission rate. As 1 micron of coating was applied on PP films, the barrier performance can be further improved by increasing the coating thickness.

Moisture barrier is another crucial property of packaging polymer film. In order to be excellent packaging films, the films should also possess high moisture barrier performance. Excellent moisture barrier performance was achieved with CNC-CA coating on PP films, which is unsurprising due to the PP substrate as PP itself is a very high moisture barrier film. Overall, WVTR was significantly lower (better) than PET, PP, HDPE, LDPE, and EVOH films.

Table 5.3 . WVTR of CNC-CA coated PP films, compared with other commercially available polymer films.

Polymer Films		P _{O2} cm ³ .cm/cm ² .s.Pa	P _{CO2} Permeability cm ³ .cm/cm ² .s.Pa	WVTR g/m ² .24hr	Conditions for WVTR	References
Uncoated PP		3.18E-14	1.02E-13	2.43	90%RH, 23°C	This Work
CNC Coated PP	100 CNC	2.62E-15	8.55E-15	1.8	90%RH, 23°C	This Work
	80CNC-20CA	1.84E-15	2.55E-15	1.3	90%RH, 23°C	This Work
100 CNC		1.48E-16	4.66E-16	90%RH, 23°C	This Work
80CNC-20CA		1.03E-16	1.93E-16	90%RH, 23°C	This Work
Cellulose Nanofibers (CNFs)		6.49E-15	2.72E-15	234	50%RH, 23°C	[167,181]
CNC-PVOH coated PLA		160	3% RH, 23°C	[114]
Polypropylene, PP		1.70E-13	6.90E-13	5	90% RH, 23°C	[167,182]
LDPE		2.24E-13	1.12E-12	8	100% RH, 37.8°C	[183,184]
HDPE		8.32E-14	2.61E-13	1.5	100% RH, 37.8°C	[183,184]
PLA		3.39E-14	9.34E-14	300	3% RH, 23°C	[114,167]
Cellophane		5.30E-16	9.70E-16	533	22% RH, 25°C	[167,185]
PET		2.16E-15	1.08E-14	15	85% RH, 23°C	[182,186]
PVOH		6.60E-16	9.20E-16	27	90% RH, 23°C	[167,182]
Ethylene vinyl alcohol, EVOH		6.65E-16	1.10E-15	10	90%RH, 35 °C	[167,187]

5.4 Summary

In this work, the polypropylene (PP) substrate was successfully coated with cellulose nanocrystals (CNC) and cellulose nanocrystal-citric acid (CNC-CA) using a shear process. Varying amount of CA (0 to 25% by weight) was added to the CNC suspensions to investigate the coating quality and barrier performance of the coated PP. The CNC and CNC-CA coatings were smoother than the base PP, although CNC-CA coated surfaces have higher surface roughness as compared to CNC-coated surface. Both CNC and CNC-CA coated PP have similar high transparency property with only a 2% reduction in transmission, likely due to higher reflectivity due to the increased refractive index. The CNC coating improved both O₂ and CO₂ barrier performance by 92%, while maintaining a high moisture barrier property (low WVTR). Addition CA up to 20% by weight further improved the gas barrier properties, most probably by occupying the existing free volume of the coating system, although the higher hydrophobicity of the CA may also contribute to the improved WVTR. Overall, this study showed that the CNC-CA coated PP films have better barrier performance than most commonly used commercial polymers revealing the potential of CNC-CA as ecological bio-based coating for traditional polymers to improve barrier performance.

CHAPTER 6. CONCLUSION AND FUTURE WORK

The goal of this research work was to investigate the molecular transportation in polymer packaging and fiber-reinforced polymer composite based CIPP liners. Two different form of CIPP liners (steam-cured and UV-cured liners) were collected from the installations sites, and investigated the physical, thermal, viscoelastic and mechanical properties of the liners. Study revealed that physical property, and presence of volatiles compounds varied from inner layer to outer layer of the liners. Short-term water aging did not degrade mechanical property of the liners, although the modulus of the liners was increased because of leaching of unreacted organic compounds. It is important to note that the properties of the liners varied from one installation site to another even though same materials and curing conditions were used. Study suggested that the final properties (thermal, mechanical, viscoelastic etc.) of the liners depended on the curing conditions. Improper curing causes to have high volatile compounds inside the liners, and poor mechanical performance. Furthermore, the liner's performance responses differently in different environment conditions. Study suggested that aggressive chemical aging (salt solutions and pore solution aging) had much higher negative impact than water aging. Also, improper cured liners may show degradation responses much faster than cured liners.

Another important aim of this research work was to develop new high gas barrier coating materials for packaging applications. We presented CNCs as high gas barrier coating materials which are sustainable, low cost, environment friendly. Our study showed that by controlling the order parameter of the CNC coated films, the barrier performance could be enhanced significantly, which was even better than high barrier EVOH and PVOH polymer films. We are the first group to investigate the free volume of CNCs with different structure arrangements. Furthermore, we proposed modified Dil model for single component CNC system to predict successfully the gas permeability of CNC films with different Herman's order parameter. Furthermore, addition of citric acid into CNC suspension can enhance the gas and water vapor barrier performance of CNC coated film. Polypropylene (PP) films are cheaper and high moisture barrier but have poor oxygen barrier performance. Our study suggested that application of approximately 1 microns CNC-CA coating on PP substrate could improve the gas barrier performance while retaining their high water vapor barrier performance. This research approach has opened a new window for coating industries to utilize biobased coating for traditional low gas barrier polymers.

This research work has inspired to conduct research further on CNCs and CIPP liners. As we need more time to conduct the research, the following directions can be listed as future research:

6.1 Thermal and UV-aging of CIPP liners

Our current study investigated the water and aggressive solution aging of CIPP liners. It is very important to investigate the thermal and UV-aging of CIPP to understand the durability of the liners. Also, a mathematical model should be proposed to show the durability of the liners for 70 years by considering the liners to be exposed into thermal and UV-aging.

6.2 Barrier performance of CNC films at higher relative humidity

Recent study showed that increasing the alignment of CNCs improve the gas barrier performance of the CNC films. The barrier performance was measured for dry oxygen and carbon dioxide gas system. As CNCs are hydrophilic due to the presence of polar -OH groups, we are expecting that the barrier performance will be degraded at higher relative humidity. Previous study from our research group reported that the hygroscopic strain of aligned CNC film was 10 times higher in transvers direction than in axial direction. As a future study, the barrier performance and free volume change at higher relative humidity of CNC films could be investigated for its applicability for food packaging.

6.3 Improve the hydrophobicity of CNC Film

Due to the hydrophilic behavior of CNC films, the commercialization of CNC coated polymer films is difficult for packaging applications. This drawback could be minimized by addition of food grade crosslinker which can initiate cross linking reaction within 80°C. Addition of crosslinker might decrease the barrier performance of the film. Thus, detailed investigation should be performed to evaluate the barrier performance at low and high relative humidity.

6.4 Investigate the solvent-free process to disperse the CNC into extrudable polymers

CNCs have gained wide attention in packaging, structural and automotive applications due to their high strength and modulus, aspect ratio, non-toxicity and sustainability. Most of the polymer used are hydrophobic and extrudable while cellulose nanocrystals are hydrophilic and

dispersed in water system. Dispersion is the big challenges for utilize them in extrudable polymers. Plasticizer dissolved in water or water/ethanol system could be used to disperse the CNC into the extrudable polymers.

APPENDIX A

Paper 1: Evaluation of the Physical, Chemical, Mechanical, and Thermal Properties of Steam-Cured Pet/Polyester Cured-In-Place Pipe

Analytical standards

Analytical standards for identification, confirmation and quantification of organic compounds by ^1H -NMR and gas chromatography/mass spectrometry (GC/MS) included dichloromethane $\geq 99.8\%$ that contained 40-150 mg/L amylene as stabilizer (CAS# 75-09-2, Sigma-Aldrich), and hexane $\geq 97.0\%$ (CAS# 110-54-3, Sigma-Aldrich) used for solid-liquid extraction experiments were used. Benzaldehyde $\geq 99.5\%$ that was purified by redistillation (CAS# 100-52-7, Sigma-Aldrich), benzoic acid (CAS# 65-85-0, Supelco), methanol $\geq 99.9\%$ (CAS# 67-56-1), phenol (CAS# 108-95-2, ACROS Organics), styrene $\geq 99\%$ that contained 4-*tert*-butylcatechol stabilizer (CAS# 100-42-5, Sigma-Aldrich), 1-tetradecanol (CAS# 112-72-1, Sigma Aldrich).

Calibration curves were created separately for each extractant solvents. For methylene chloride extracts, styrene ($R^2=0.9996$ for low range (0.1 to 3 ppm) and $R^2=0.9985$ for high range (3 to 15 ppm), benzaldehyde ($R^2=0.9992$ & 0.9981 & 0.9954 for 0.06 to 20.88 ppm), benzoic acid ($R^2=0.9968$ for 2.53 to 10.12 ppm), 1-tetradecanol ($R^2=0.996$ & 0.9919 for 0.106 to 30.56 ppm), phenol ($R^2=0.9996$ for 0.44 to 17.6 ppm) were created. For hexane extracts, styrene ($R^2=0.9998$ for 0.6 to 7 ppm), benzaldehyde ($R^2=0.9989$ & 0.9913 for 0.13 to 48.72 ppm), 1-tetradecanol ($R^2=0.9928$ for 0.4 to 80 ppm) were created.

Curing temperature determination

The maximum curing temperature is at 103 °C for CIPP liner.

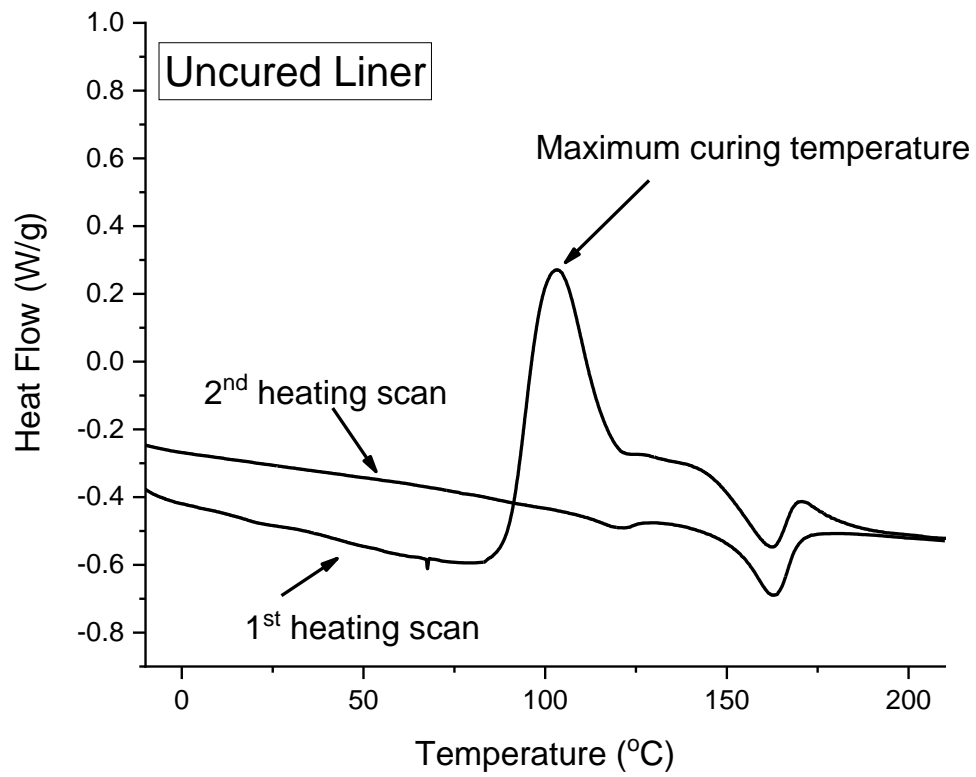


Figure A.1 DSC thermogram of uncured resin liner for determining curing temperature.

Porosity Measurement

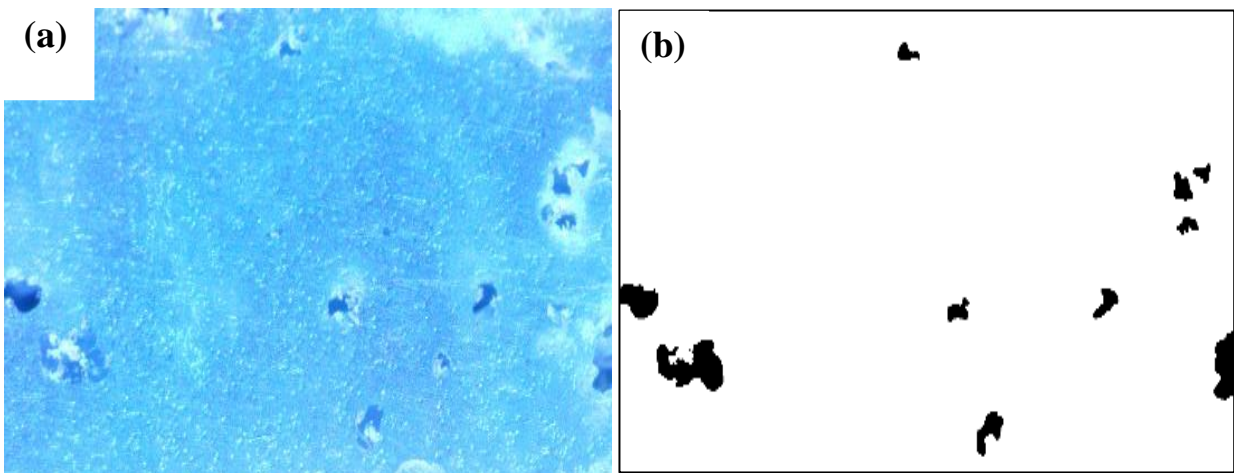


Figure A.2 (a) Optical microscopic image of CIPP liner, (b) Image J processed image.

Thermal Analysis

As shown in Figure A.3, The uncoated PET felt show sharp endothermic peak (Melting temperature) around 250 °C. In contrast, coated PET felt shows two endothermic peaks at 120 and 160 °C, indicating the melting temperature of polyethylene/polypropylene bilayer coating [188]. The cooling scan shows two exothermic peaks representing recrystallization of bilayer coating.

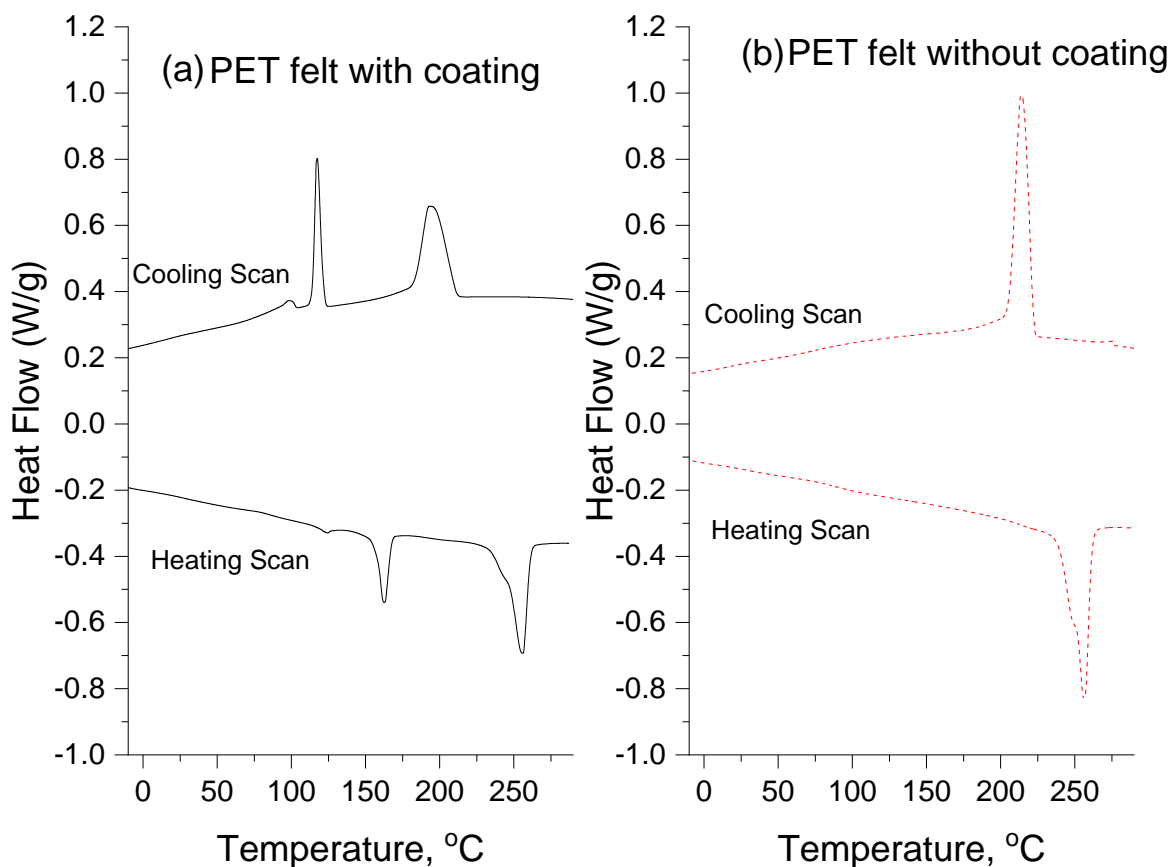


Figure A.3 DSC thermogram of (a) PET felt without coating layer, and (b) PET felt with coating layer.

As shown in Figure A.4(a), the main decomposition peak at 436 °C was due to the structural decomposition of PET felts followed by burn off carbon residue at 540 °C. Coated PET felt exhibits two more decomposition peaks representing the decomposition of bilayer coating.

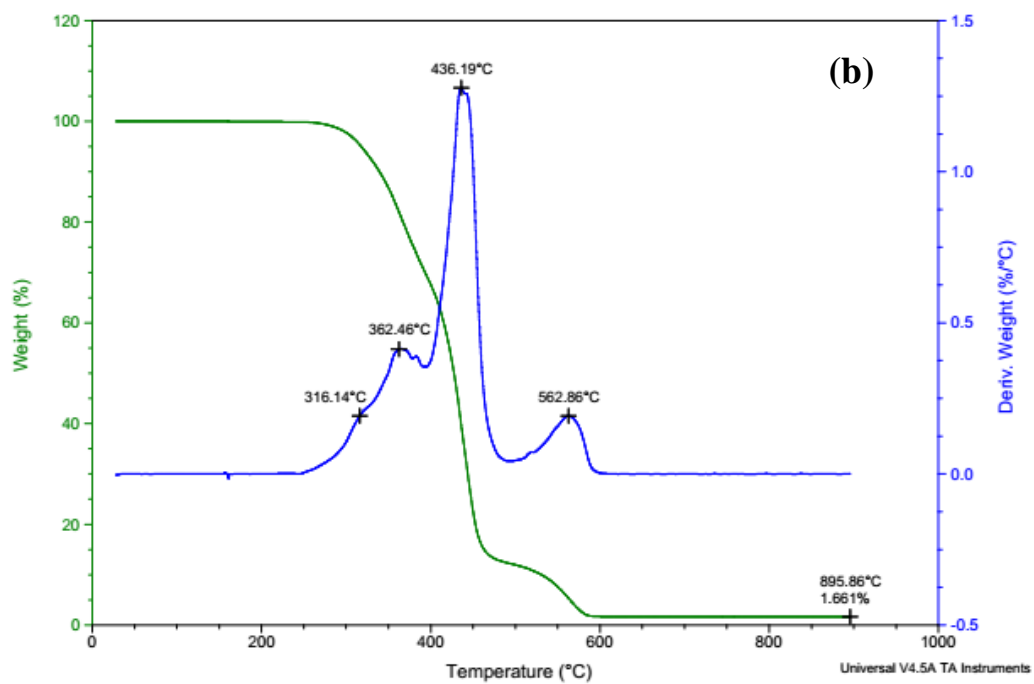
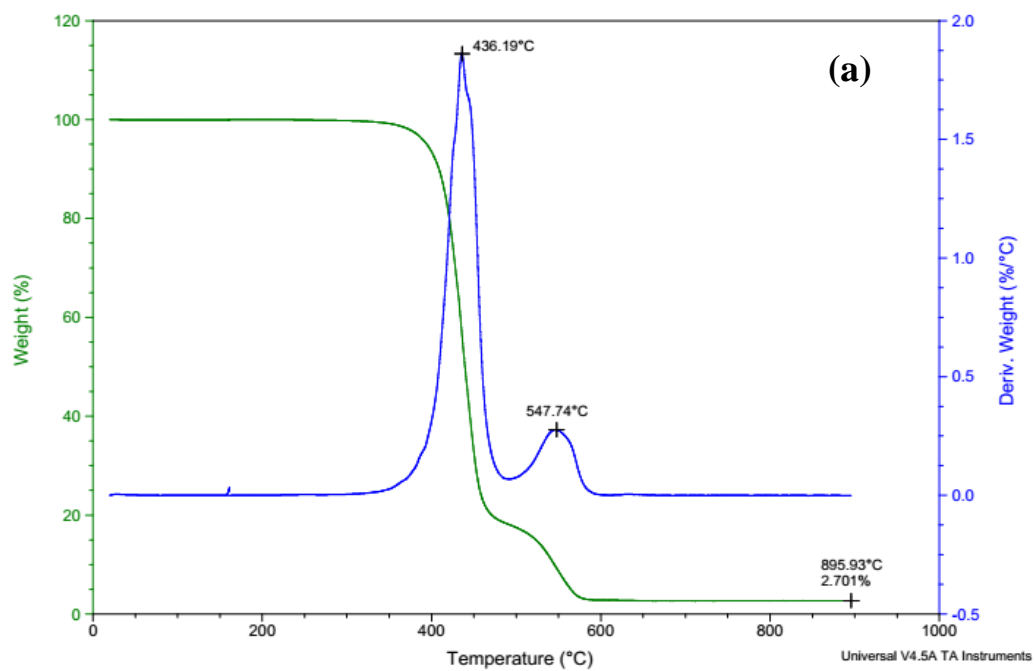


Figure A.4 TGA thermogram of (a) PET felt without coating layer, and (b) PET felt with coating layer.

¹HNMR Analysis

Figure A.5 shows the ¹HNMR spectra of uncured resin liner, onsite cured (inner and outer layer) and oven cured CIPP.

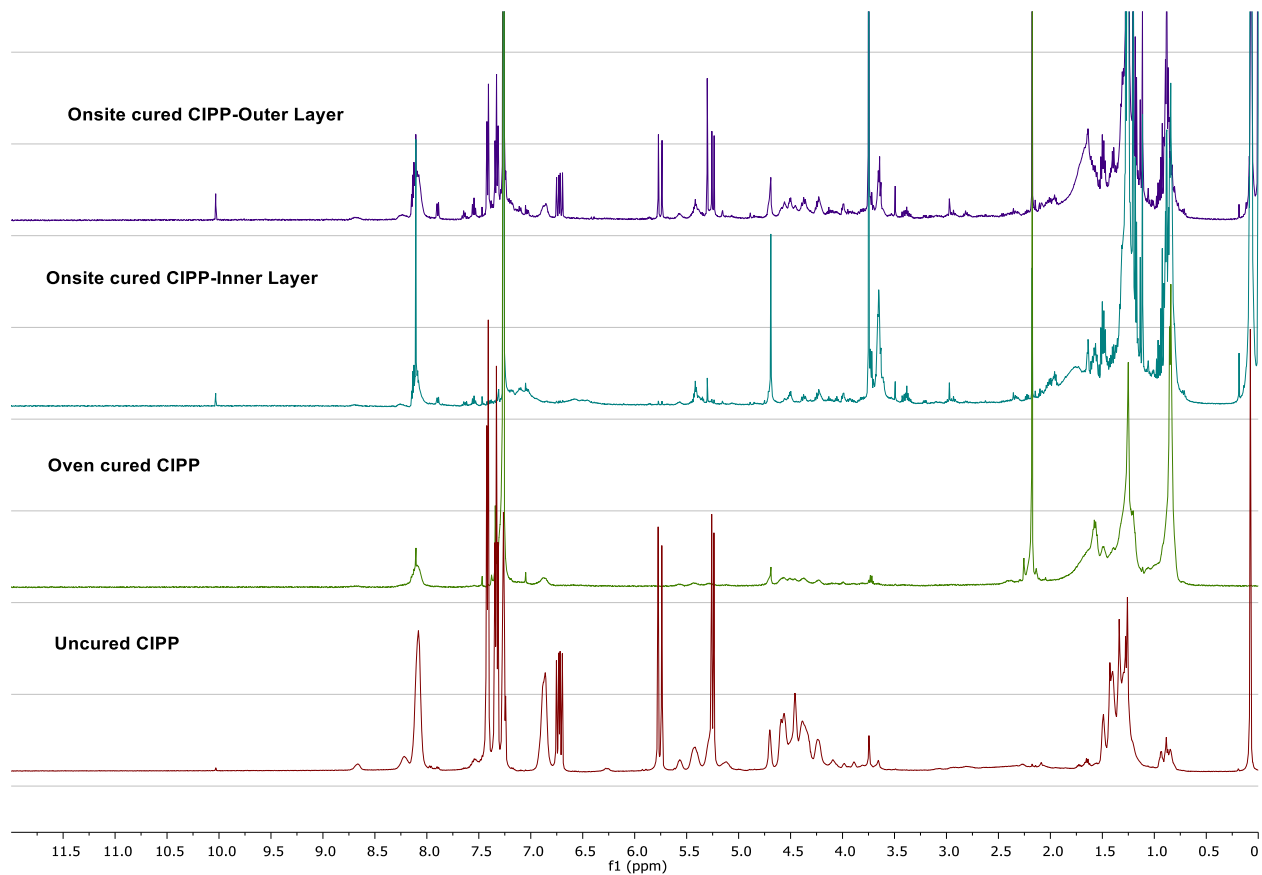


Figure A.5 ¹HNMR Spectra of CDCl₃ leaching solution from uncured, onsite cured and oven cured CIPP specimens.

Figure A.6 and A.7 show the probable formation of styrene dimer and trimer, and oxidation products of styrene.

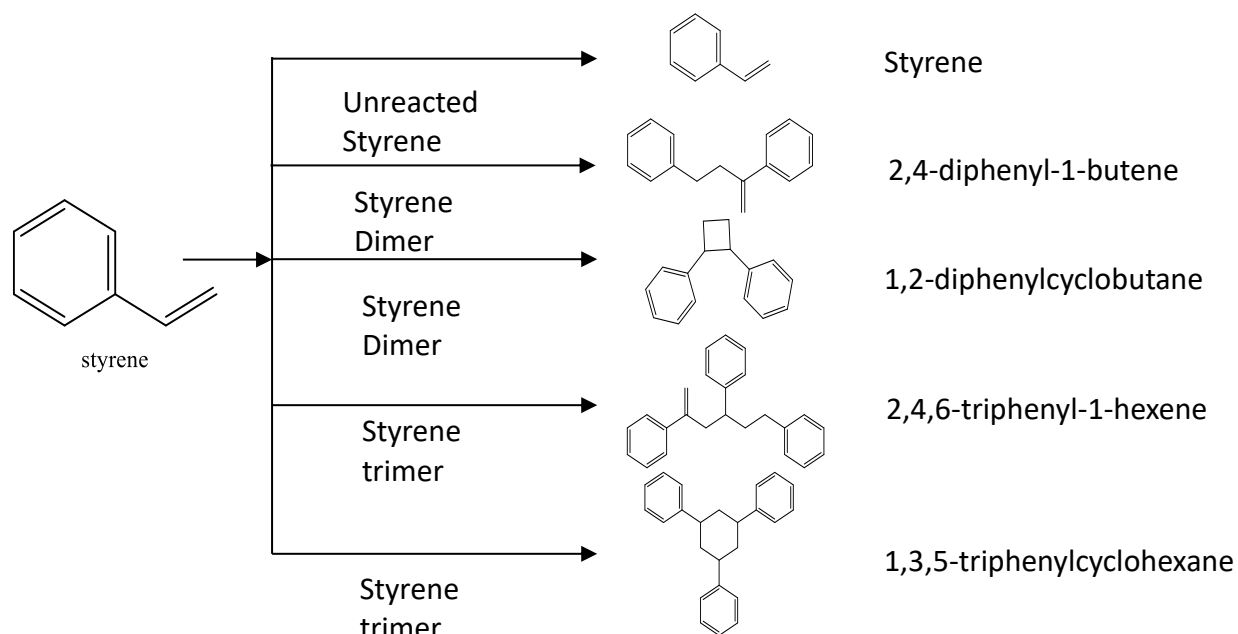


Figure A.6 dimer and trimer formation of styrene.

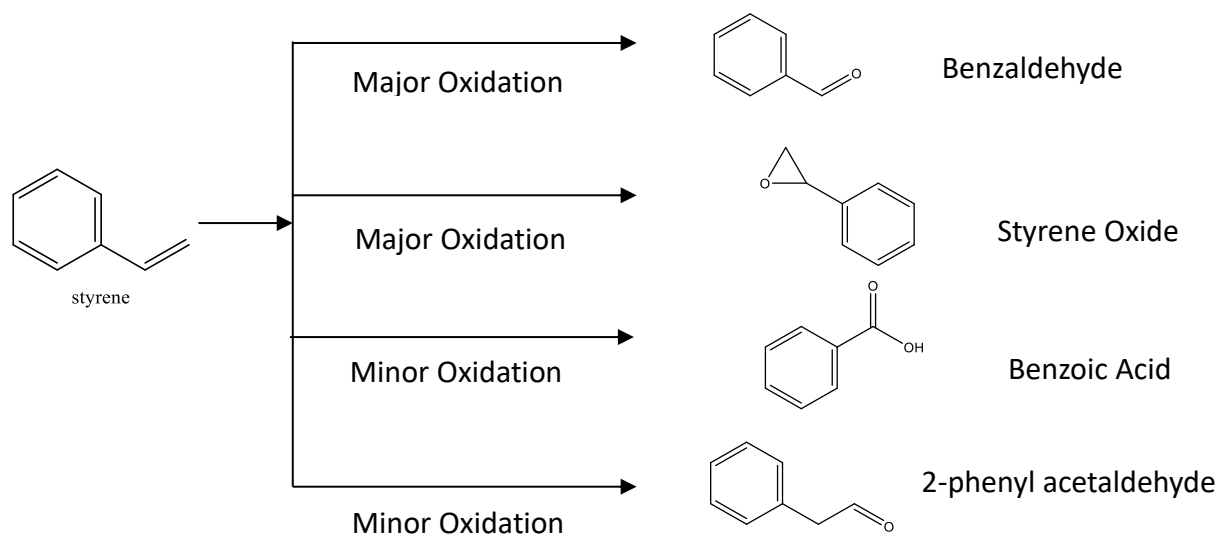


Figure A.7 dimer and trimer formation of styrene.

Table A.1 Compounds identified from GC-MS of leachate solutions of CIPP liners.

Compounds	Uncured resin	Onsite cured CIPP	Oven cured CIPP
	mg/g	mg/g	mg/g
Styrene	114.4442±6.3097*	0.7583±0.0351	0.0167±0.0007
Benzaldehyde	1.3672	0.0625±0.0053	0.3085±0.0341
1-tetradecanol	0.1048	0.0677±0.0121	0.1016±0.0126
Phenol	0.0020±0.0001	0.0020±0.0001
Benzoic acid	0.0244±0.0004	0.0331±0.0023

Asterix (*) represents 1000 times dilution, all other results represent 10 times



Figure A.8 Water diffused through the thickness of the CIPP liner during CIPP installation.

Conditioning of CIPP specimens

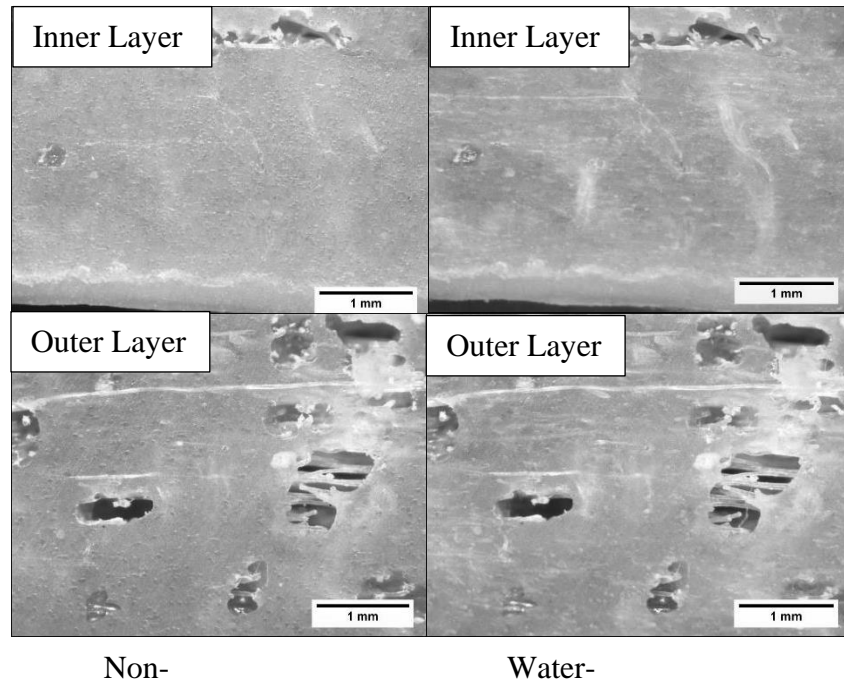


Figure A.9 (a) Inner and (b) Outer layers of non-conditioned and water-conditioned CIPP specimens.

Mechanical Characterization of CIPP

The non-conditioned samples show toughened behavior. During the experiment, these samples were not fractured. They were bend as shown in Figure A.10. In contrast, water conditioned samples exhibited brittle behaviors and fractured Figure A.11.

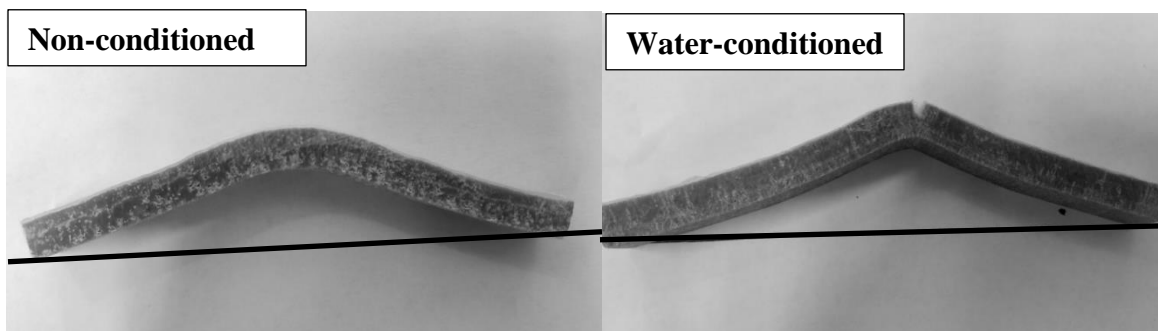


Figure A.10 Specimens after mechanical testing.

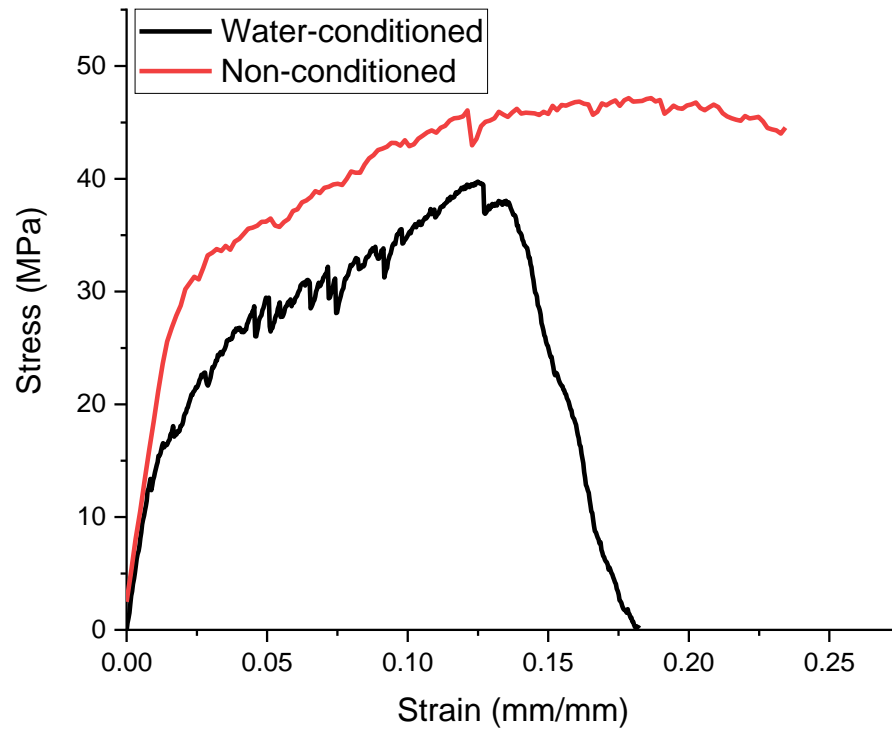


Figure A.11 Stress-strain curve of non-conditioned and water-conditioned CIPP liners.

APPENDIX B

Paper-2: Influence of Aggressive Environmental Aging on Mechanical and Thermo-Mechanical Properties of UV-Cured CIPP Liners

Interlaminar Shear Strength (ILSS) Measurement

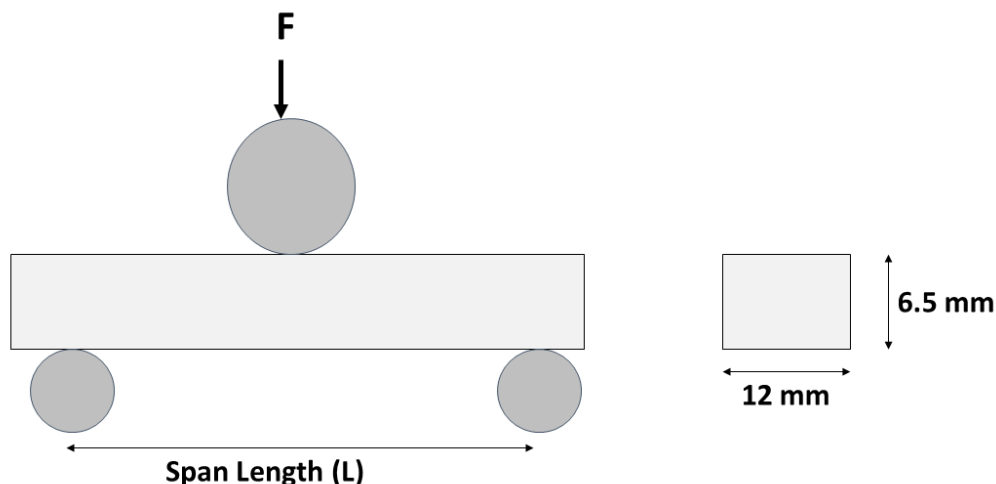


Figure B.1 ILSS test setup and test specimen.

Curing temperature determination by DSC

The uncured CIPP liner of 10-12 mg was taken in a DSC aluminum hermetic pan. Heat-cool-heat cycle scans were performed at a ramp rate of 20 °C/min from -25 °C to 200 °C. Heating and cooling curves were examined to understand curing behavior of liners.

Uncured CIPP resin tube was collected from the installation site and the curing behavior was investigated using DSC analysis. As shown in Figure B.2, the exothermic peak around 160°C in the first heating cycle, indicated maximum curing temperature of the uncured resin tube. The absent of exothermic peak in the second heating cycle indicated that the resin was fully cured after 1st heating cycle.

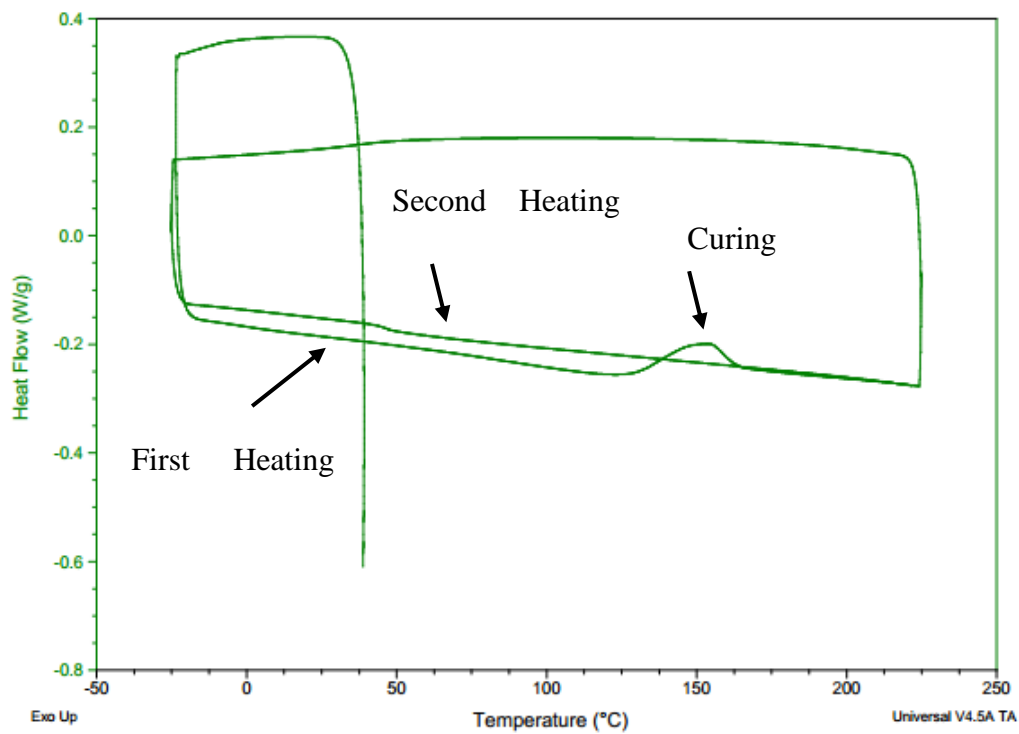


Figure B.2 DSC analysis of uncured resin tube.

Thermogravimetric Analysis

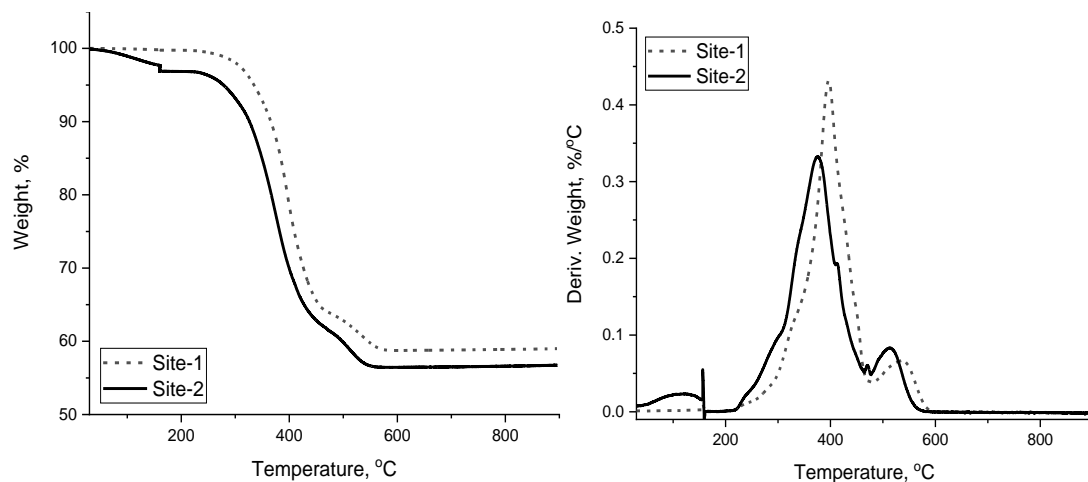


Figure B.3 TG and DTG curves of CIPP liners from installation site 1 and 2.

Aging test of CIPP specimens

The accelerated aging time was calculated according to ASTM F1980-16:

$$\text{Accelerated Aging Time (AAT)} = \frac{\text{Desired Real Time (RT)}}{Q_{10}[\frac{T_{AA} - T_{RT}}{10}]} \quad (\text{B-1})$$

Desired real time = 96 days

Accelerated aging time (T_{AA}) = 15 days

Room Temperature (T_{RT}) = 23 °C

Aging Factor, Q_{10} = 2.0

Ion Chromatography

The presence of ions in tap and DI water was investigated using Ion chromatography. The mobile phase (eluent) is pumped through the system with a constant flow rate. The sample is injected into it. The mobile phase carries the sample through the static phase (separator) where the sample is split up into its component ions. In the detector, single components are recognized by a change in conductivity.

The ions are effectively separated according to their charge/size ratio as they interact with the exchange groups in the column:

- Ions with a smaller charge/size ration elute earlier
- Ions with a larger charge/size ratio elute later

Experimental conditions to run our samples

Cation eluent - Oxalic acid (Conc.: 3.5 mM)

Cation Conductivity: 745 - 765 uS/cm

Cation Flow rate: 0.9 mL/min

Anion eluent - Equal mix of Sodium carbonate (Conc.: 3.2 mM) and Sodium bicarbonate (Conc.: 1 mM)

Anion Conductivity: 0.5 - 2 uS/cm

Anion Flow rate: 0.7 mL/m

Tap water and DI water contained cations and anions (Table SI-1), which may ingress into composite body during processing of the specimens for the experiments.

Table B.1 Presence of anions and cations in tap and DI water.

Ions	Tap Water	DI water
F-	0	0.01
Cl-	40.13	0.28
Br-	0.1	0
NO ₃ -	0.21	0.01
PO ₄ ³⁻	0.57	0
SO ₄ ²⁻	0	0
Li+	0	0
K+	3.35	0.02
Mg ²⁺	35.26	0.36
Ca ²⁺	109.29	1.65

APPENDIX C

Paper-3: Structure-Property Relationship of Cellulose Nanocrystals Film for Gas Barrier Applications

TEM image of CNC

The TEM image is shown in Figure SI-1. The Average length and width of TEMs were $100\pm 25\text{nm}$ and $5.0\pm 1.5\text{ nm}$.



Figure C1. TEM image of CNC.

Zeta Potential

Zeta potential was measured by controlling the pH by adding HCl and NaOH to a CNC solution in the dilute state. 1mL CNC sample was placed in a disposable cuvette and measured on a

Zetasizer Nano ZS equipment (Malvern Instruments Ltd). The zeta potential of CNC suspension, within 2.7 -12.8 pH, was -47.4 ± 2 mV.

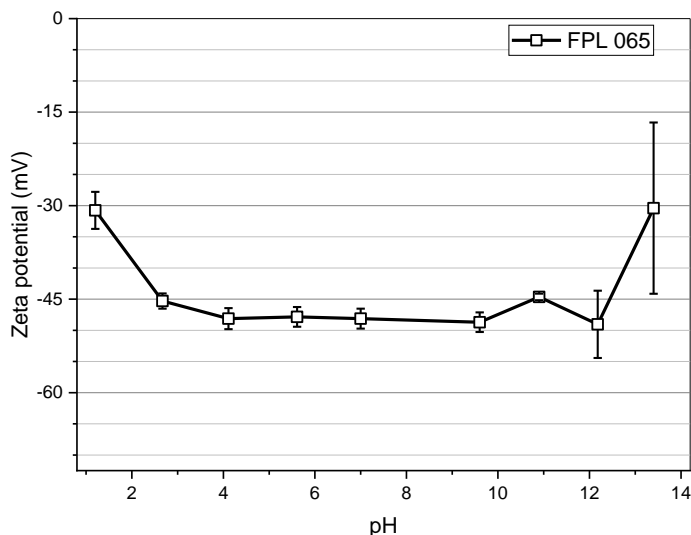


Figure C2. Zeta potential of CNC suspension as a function of pH.

XRD Analysis of CNC

20 gm of 2 wt% CNC suspension was poured into a 50 mm polystyrene petri dish and left, uncovered, inside the fume hood at RT for 7 days. The dry film was then peeled off from the container and analyzed by X-ray diffraction using a Panalytical Empyrean Powder X-ray diffractometer, with Cu radiation (1.540598 \AA), at 45 kV and 40 mA, by rotating the sample at 2 Hz, on a single crystal Si wafer. The diffractometry displayed 6 peaks characteristic of Cellulose I β and II. Peaks were identified and deconvoluted using OriginPro 2018. Segal Crystallinity index was calculated² from the (200) plane of cellulose I β , using the following equation, where $I_{(\text{peak})}$ is the intensity of the deconvoluted peak at the plane's characteristic angle.

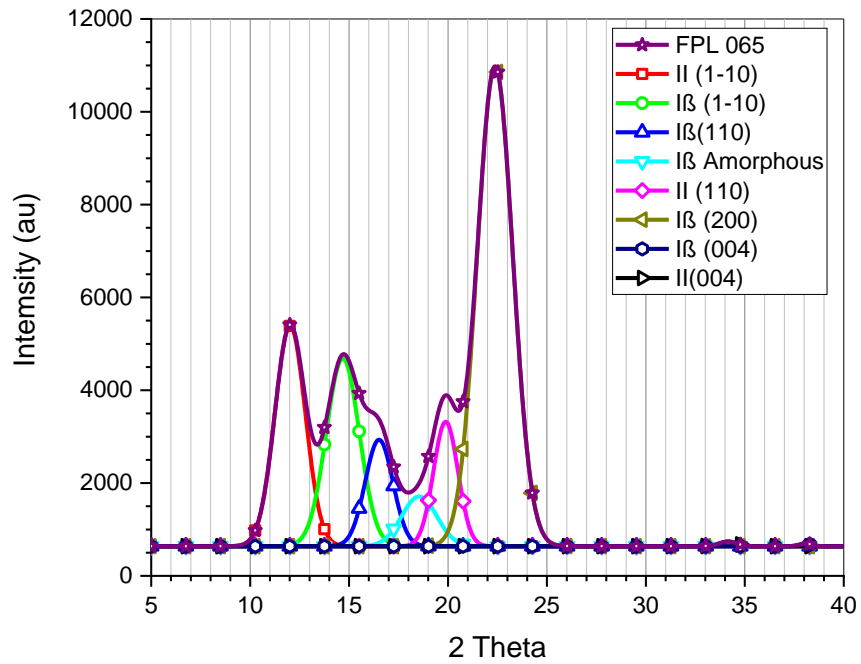


Figure C3. X-ray deconvoluted peaks of CNC

Table C1. Peak analysis of CNC

Plane	2θ (°)	Peak Height	FWHM
II (1-10)	12.02	9157	1.8121
Iβ (1-10)	14.67	8281	1.9383
II Amorphous	16.53	4401	1.7407
Iβ (110)	18.73	2486	1.9132
Iβ Amorphous	19.85	3403	1.2540
II (110)	20.63	354	0.6905
Iβ (200)	22.37	23447	2.1293
II & Iβ (004)	34.15	108	1.0155

$$CI\% = \frac{(I_{\beta(200)} - I_{\beta \text{ Amorphous}})}{I_{\beta(200)}}$$

$$CI\% = 85.5\%$$

Surface Tension and Surface Energy Measurement

Surface tension of the CNC coating formulations was measured by pendant drop tensiometer, using a Ramé-Hart contact angle goniometer (Ramé-Hart Inc., NJ, USA) with DROP Image Advanced software. A small drop of liquid (10-15 µl) was suspended from a Teflon tip (volume 30 µl) into the air under room temperature. Ten measurement of the surface tension was taken with 30 seconds per measurement, and the average value was reported as a final measurement of the surface tension.

The PP substrate was placed in the goniometer and a 4 µL drop of liquids (water and diiodomethane) carefully deposited on its surface by using a micropipette. The contact between PP and the liquid was measured by sessile drop method at RT and 50% RH. A minimum of 5 droplets were examined for each film, and the average value was considered for surface energy measurement. The values of contact angles of water and diiodomethane drops deposited on PP substrate were then used to calculate the surface energy of the PP by using the DROP Image Advanced software.

Calculation Method: Geometric

Liquid 1 Name (Angle): Water (106.24 ± 0.61)

Liquid 2 Name (Angle): Diiodomethane (59.80 ± 0.55)

Substrate: PP

Polar Component: 0.03 ± 0.02

Dispersive Component: 28.69 ± 0.32

Total Surface Energy: 28.72 ± 0.31

Instrumentation for Gas permeability

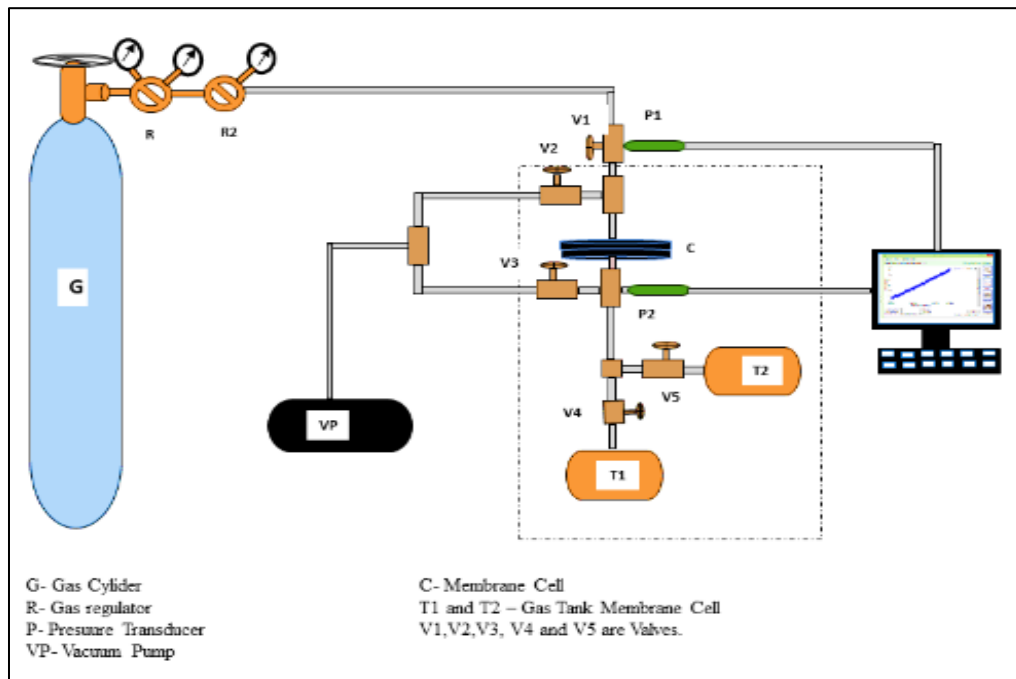


Figure C4. Experimental setup for measuring gas permeability.

Table C2: Relative fractional free volume, and gas permeability data for engineering polymers and cellulose nanocrystals (CNCs).

Polymer	Relative Fractional Free volume	P _{O2}	P _{CO2}	Reference
Self-standing CNC film	1.234	2.91E-15	1.07E-14	This Work
Shear oriented CNC film	1.041	1.48E-16	4.21E-16	This Work
Cellulose nanofibers (CNFs)	0.87	6.49E-15	2.72E-15	[137,142]
PAN	1.47	1.50E-17	6.00E-17	[189,190]
PVOH	1.56	6.60E-16	9.20E-16	[190,191]
EVOH	1.74	6.65E-16	1.10E-15	[190,192]
PVC	1.61	3.40E-15	1.20E-14	[190,193,194]
PET	2.15	2.16E-15	1.08E-14	[195,196]
Nylon 6	2.34	2.85E-15	6.60E-15	[140,190]
PLA	2.1-2.37	3.39E-14	9.34E-14	[190,197]
HDPE	3.36	3.00E-14	2.70E-14	[190,198]
Polysulfone	3.39	1.13E-13	4.2E-13	[190,199]
Polymethyl methacrylate	3.71	1.16E-14	2.33E-13	[190,200]
PS	5.1	2.00E-13	7.90E-13	[190,201]
PP	3.54	1.70E-13	6.90E-13	[190,202]
Polycarbonate	6.50	2.96E-13	1.92E-12	[190,203]
LDPE	7.22	2.20E-13	9.50E-13	[190,204]
Polybutadiene	9.17	1.43 E-12	1.04 E-11	[190,205]
PTMSP	9.45	8.7E-10	2.82E-9	[206,207]
PDMS	24.02	6.95E-11	3.49E-10	[208,209]

Parameters and Calculation for Model

The volume fraction of anisotropic phase of CNC film:

$$\phi_{anisotropic} = \frac{X(m/d_{anisotropic})}{(X(m/d_{anisotropic})) + Y(m/d_{isotropic})} \quad (1)$$

Modified Dil model for single component CNC system:

$$\frac{P_{anisotropic}}{P_{isotropic}} = \frac{1 - \phi_{anisotropic}}{1 + \frac{L\phi_{anisotropic}}{2W} \left(1 - \sqrt{\frac{2}{3}} (1 - S) \right)} \quad (2)$$

Modified Bharadwaj model for single component CNC system:

$$\frac{P_{anisotropic}}{P_{isotropic}} = \frac{1 - \phi_{anisotropic}}{1 + \frac{L\phi_{anisotropic}}{2W} \left(\frac{2}{3} \right) \left(S + \left(\frac{1}{2} \right) \right)} \quad (3)$$

Table C3. Parameters for predicting gas permeability with varying Herman's order parameter.

S	d _{aniso}	d _{isotropic}	Φ ^a	L	W	Dil ^b Model	Bharadwaj ^c model
						P _{aniso} /P _{iso}	P _{aniso} /P _{iso}
0	1.55	1.45	0	100	5	1	1
0.1	1.55	1.45	0.094156	100	5	0.747254	0.658019
0.2	1.55	1.45	0.189542	100	5	0.5363	0.430058
0.3	1.55	1.45	0.286184	100	5	0.374346	0.282552
0.4	1.55	1.45	0.384106	100	5	0.255371	0.186373
0.5	1.55	1.45	0.483333	100	5	0.169799	0.122368
0.6	1.55	1.45	0.583893	100	5	0.108823	0.07878
0.7	1.55	1.45	0.685811	100	5	0.065578	0.048438
0.8	1.55	1.45	0.789116	100	5	0.035091	0.026029
0.9	1.55	1.45	0.893836	100	5	0.013913	1.67E-12
1	1.55	1.45	1	100	5	0	0

^aCalculated from equation 1

^bCalculated from equation 2

^cCalculated from equation 3

Table C4. Comparison of theoretical relative permeability (P_c/P_m) results of CNC films with experimental values.

Herman's Order Parameter	Pa/Pc (Experimental value)		Pa/Pc (Modified Dil et al. model)	Error in Prediction (%)		Pa/Pc (Modified Bharadwaj model)	Error in Prediction (%)	
	O ₂	CO ₂		O ₂	CO ₂		O ₂	CO ₂
0.28	0.389 ^a	0.225	0.403	3.473	44.168	0.307	-26.710	26.710
0.49	0.166 ^a	0.08	0.177	6.214	54.802	0.128	-29.688	37.50
0.75	0.051 ^b	0.039	0.049	-4.081	20.408	0.037	-37.838	-5.405
0.85	0.01 ^a	0.037	0.024	58.333	-54.167	0.019	47.368	-94.737

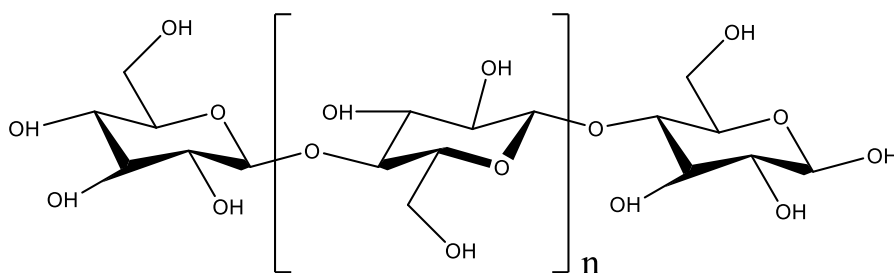
^aThe experimental values were considered from previous study [137].

^bExperimental values from this study

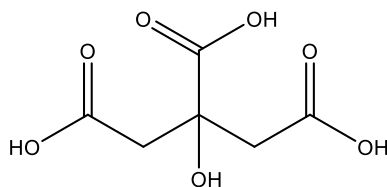
APPENDIX D

Paper-4: Gas and Water Vapor Barrier Performance of Cellulose Nanocrystals-Citric Acid Barrier Coatings for Flexible Packaging

Structure of Cellulose nanocrystal (CNC) and Citric acid (CA)



Cellulose



Citric Acid

Figure D1. Chemical structure of cellulose and citric acid.

TEM image of CNC

The TEM image was shown in Figure SI-1. The Average length and width of TEMs were 100 ± 25 nm and 5.0 ± 1.5 nm.



Figure D2. TEM image of CNC.

Zeta Potential

Zeta potential was measured by controlling the pH by adding HCl and NaOH to a CNC solution in the dilute state. 1mL CNC sample was placed in a disposable cuvette and measured on a Zetasizer Nano ZS equipment (Malvern Instruments Ltd). The zeta potential of CNC suspension, within 2.7 -12.8 pH, was -47.4 ± 2 mV.

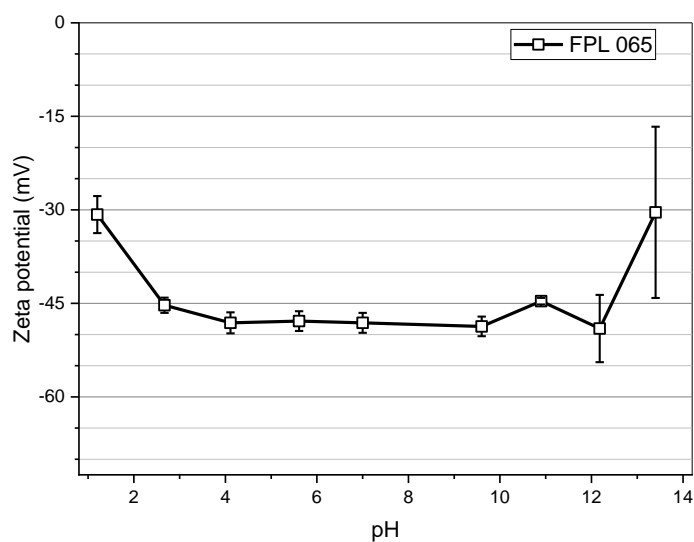


Figure D3. Zeta potential of CNC suspension as a function of P^H .

XRD Analysis of CNC

20 gm of 2 wt% CNC suspension was poured into a 50 mm polystyrene petri dish and left, uncovered, inside the fume hood at RT for 7 days. The dry film was then peeled off from the container and analyzed by X-ray diffraction using a Panalytical Empyrean Powder X-ray diffractometer, with Cu radiation (1.540598 \AA), at 45 kV and 40 mA, by rotating the sample at 2 Hz, on a single crystal Si wafer. The diffractometry displayed 6 peaks characteristic of Cellulose I β and II. Peaks were identified and deconvoluted using OriginPro 2018. Segal Crystallinity index was calculated² from the (200) plane of cellulose I β , using the following equation, where $I_{(\text{peak})}$ is the intensity of the deconvoluted peak at the plane's characteristic angle.

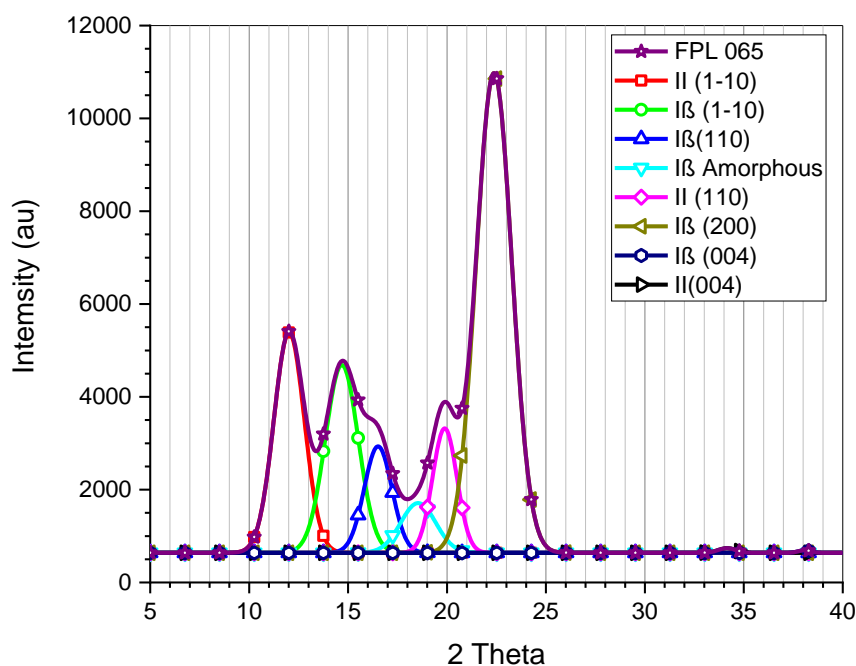


Figure D4. X-ray deconvoluted peaks of CNC

Table D1. Peak analysis of CNC

Plane	2 θ (°)	Peak Height	FWHM
II (1-10)	12.02	9157	1.8121
Iβ (1-10)	14.67	8281	1.9383
II Amorphous	16.53	4401	1.7407
Iβ (110)	18.73	2486	1.9132
Iβ Amorphous	19.85	3403	1.2540
II (110)	20.63	354	0.6905
Iβ (200)	22.37	23447	2.1293
II & Iβ (004)	34.15	108	1.0155

$$CI\% = \frac{(I_{I\beta(200)} - I_{I\beta \text{ Amorphous}})}{I_{I\beta(200)}}$$

$$CI\% = 85.5\%$$

PP substrate and Coating formulations compatibility

The surface energy of PP substrate was 28 mNm⁻¹. In contrast, the surface tension of coating CNC and CNC-CA coating formulations were 68-70 mNm⁻¹ as shown in Table

Table D2: Surface tension of Coating formulations.

Coating Formulation	Surface Tension, mN/m
100% CNC	70.54±0.21
95CNC-5CA	70.20±0.19
90CNC-10CA	69.97±0.15
85CNC-15CA	69.76±0.42
80CNC-20CA	69.43±0.23
75CNC-25CA	68.74±0.15

CNC coating on PP substrate

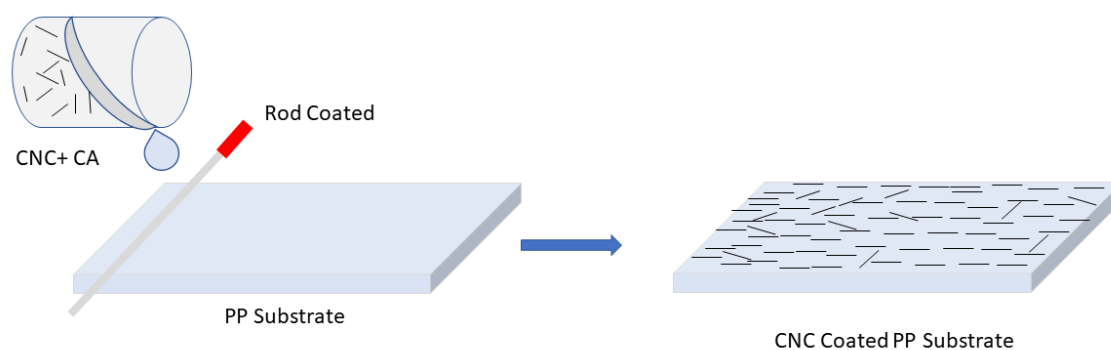


Figure D5. Application of CNC-CA on PP substrate.

Instrument for Measuring Gas Permeability

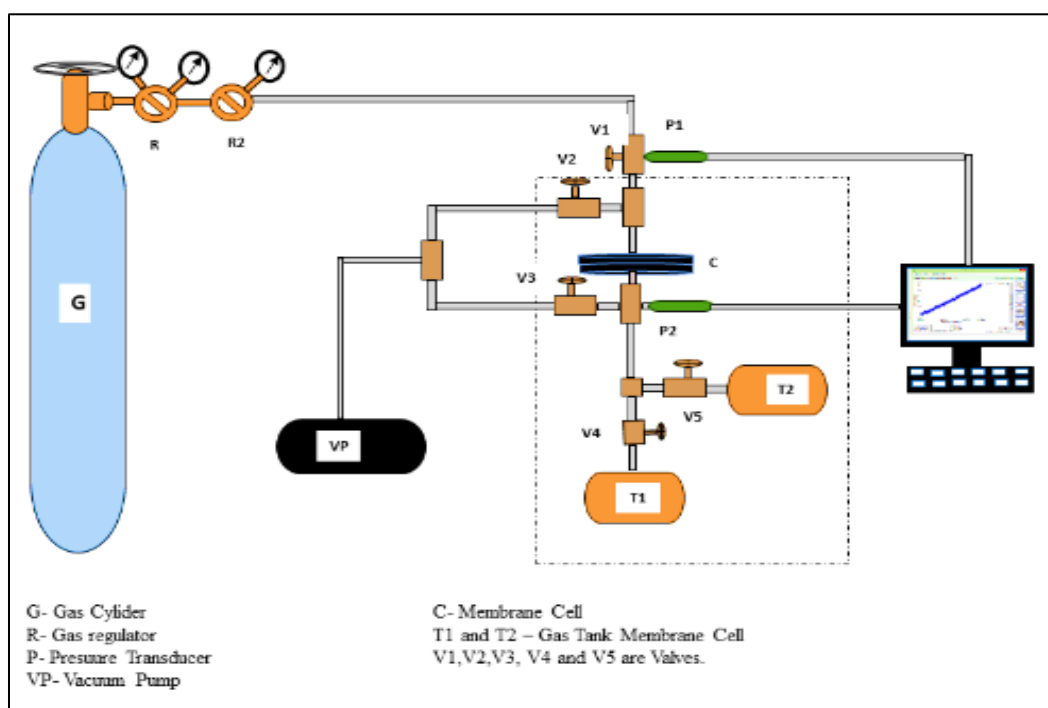


Figure D6. Experimental setup for measuring gas permeability.

Thickness of CNC and CNC-CA coated PP

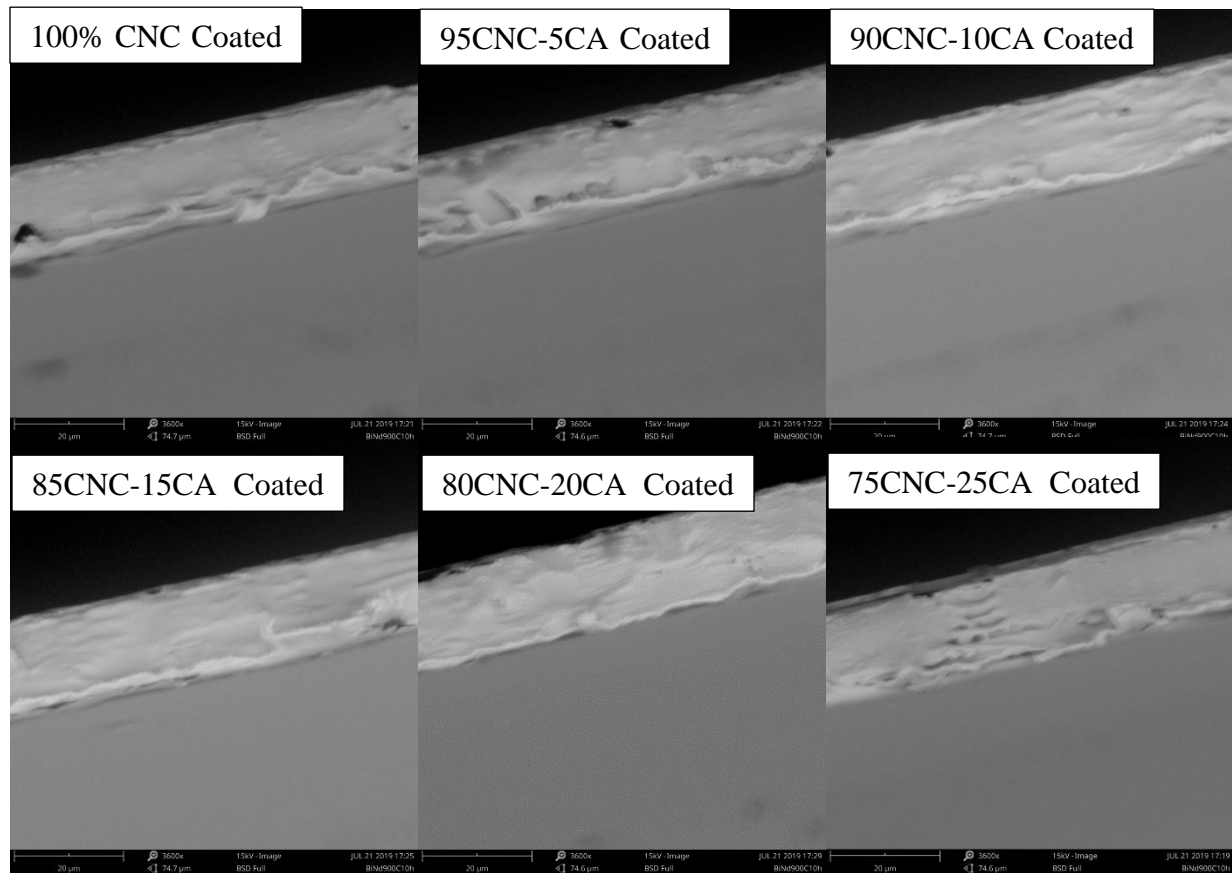


Figure D7. Microscopic images of cross section Area of CNC and CNC-CA coated PP.

Yield stress and flow index value

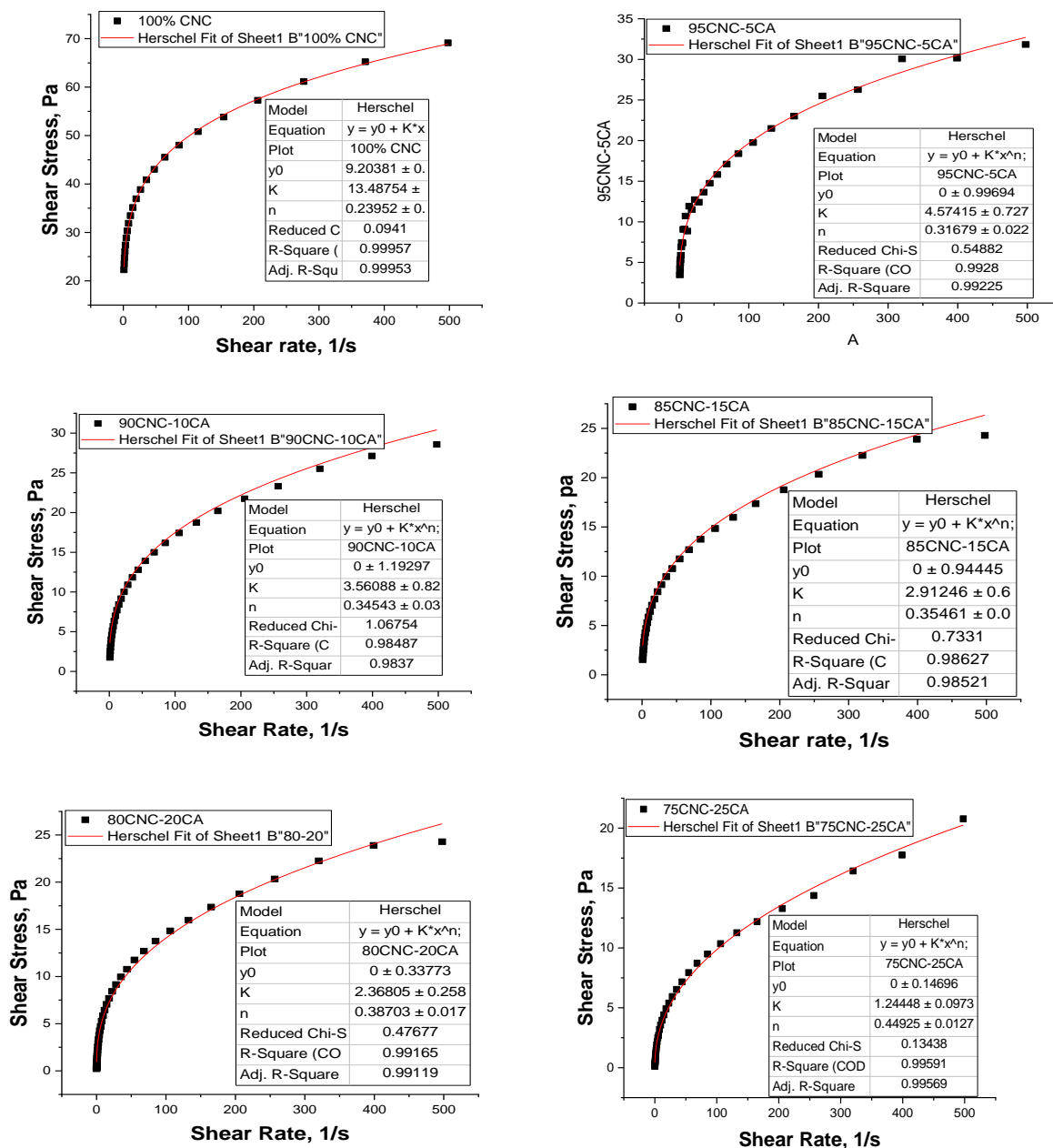


Figure D8. Yield stress vs shear rate curves for CNC-CA formulations to determine flow index values.

Contact Angle Measurement

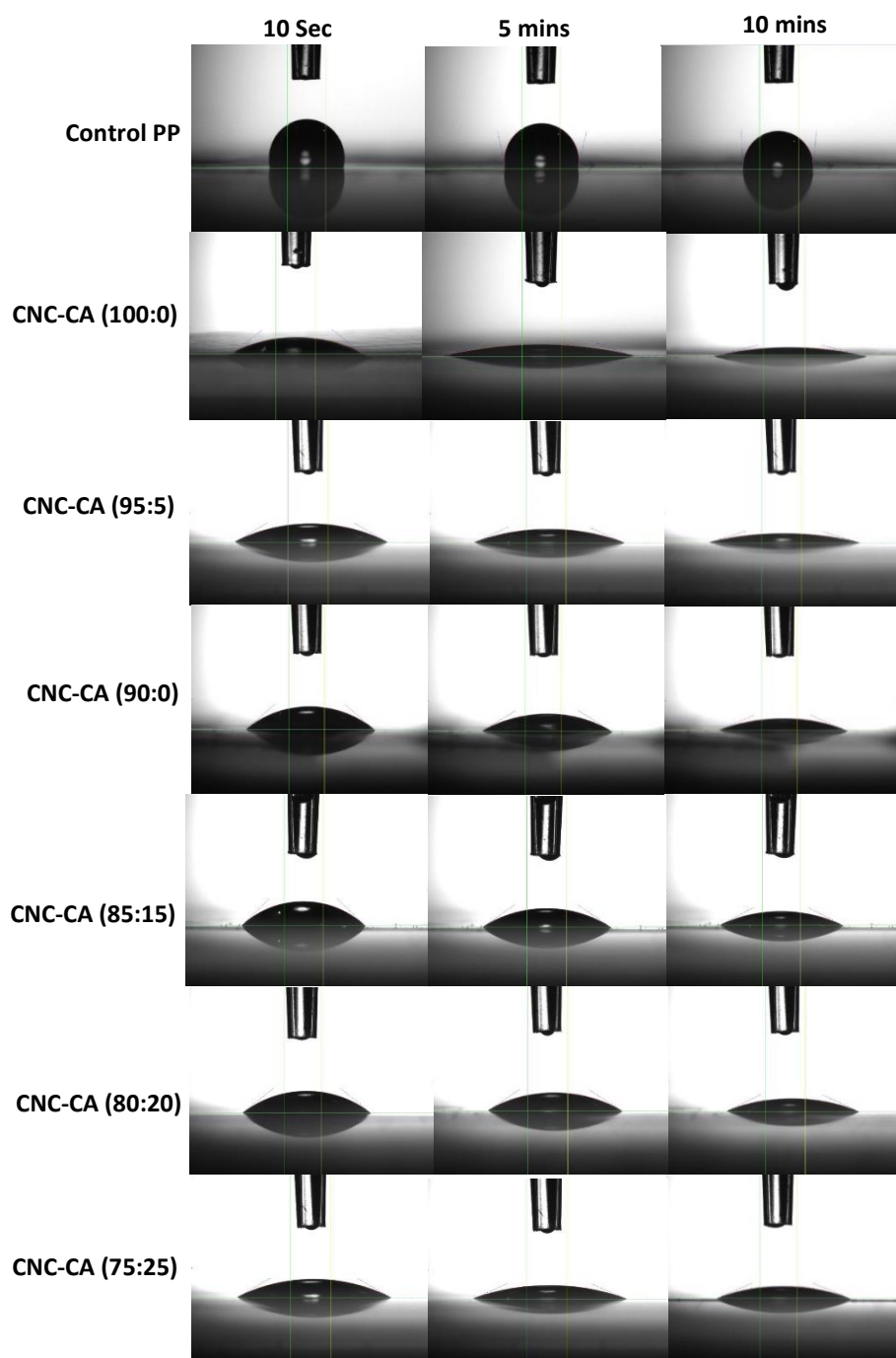


Figure D9. Contact angle measurement of CNC and CNC-CA coated PP films.

FTIR Analysis of CNC and CNC-CA Coated Layer

Some of added CA in CNC suspension participated in esterification of OH-groups of CNC surfaces. Rest of the CA occupy the free volume of the CNC films. Thus, the peak at 1729 cm^{-1} is the C=O stretching vibration peak, which is probably a coalescence peak caused by the ester bond (from esterified CNC) and carboxyl C=O groups in CA.

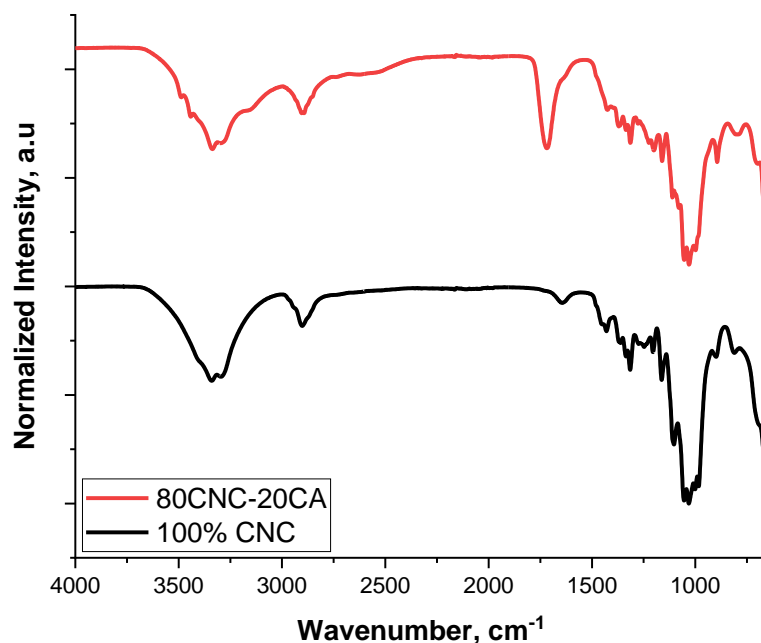
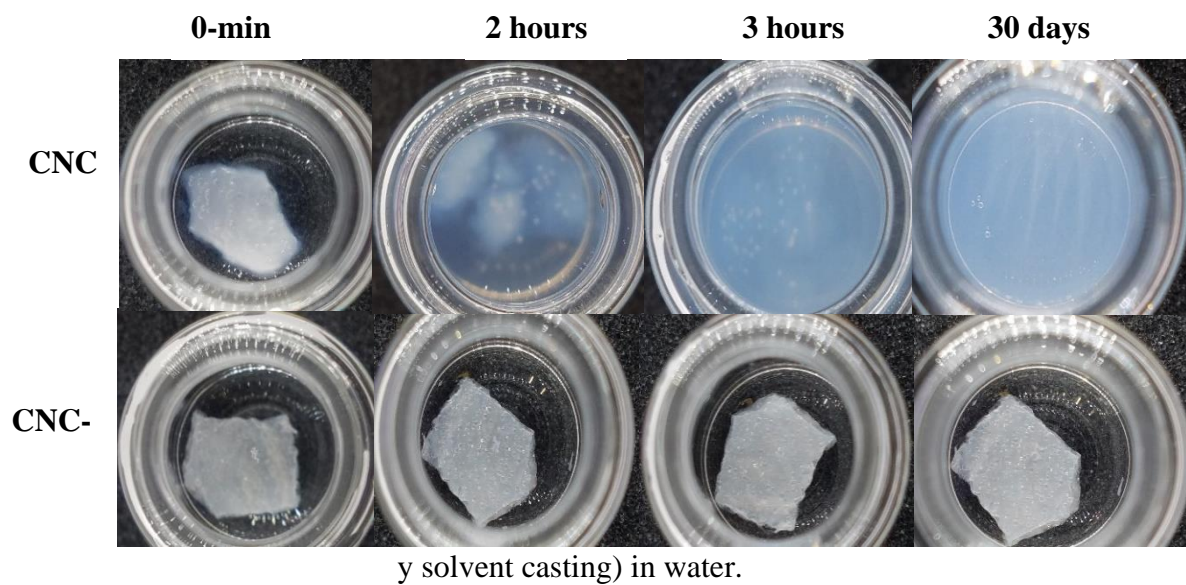


Figure D10. FTIR spectra of CNC and CNC-CA film.

The hydrophilicity nature of the CNC and CNC-CA films were investigated by immersing the films in water. The delaminated CNC and CNC-CA films were very thin. In order to visualize the dissolution of CNC films, both films were also prepared by solvent casting method and dried at $80\text{ }^{\circ}\text{C}$ for 5 hours to investigate the solubility. As can be seen from Figure S10, CNC films dissolved in water within 2 hours while CNC-CA films remained intact after 30 days. This implies that addition of CA into CNC enhances the hydrophobicity by surface esterification followed by crosslinking.

Figure D11. Solubility of CNC and CNC-CA film (prepared b



REFERENCES

- [1] Al-Assafi, S., & Mosallam A. Impact of aqueous environments on performance of pultruded composites. Proc. HBRC Int. Conf. Futur. Vis. challenges urban Dev., Cairo, Egypt: 2004, p. 20–4.
- [2] Joannie W. Chin, Khaled Aouadi, Michael R. Haight, William L. Hughes and TN. Effects of Water , Salt Solution and Simulated Concrete Resins Used in Civil Engineering Applications. Polym Compos 2001;22:282–98. doi:10.1002/pc.10538.
- [3] Nacher LS, Amoros JEC, Moya MDS, Lopez J. Mechanical Properties of Polyester Resins in Saline Water Environments. Int J Polym Anal Charact 2007;5341:373–90. doi:10.1080/10236660701516557.
- [4] Crank, J. Park GS. Diffusion in Polymers, Academic Press. Academic Press Inc. (London) Ltd; 1968.
- [5] Teimouri Sendesi SM, Ra K, Conkling EN, Boor BE, Nuruddin M, Howarter JA, et al. Worksite Chemical Air Emissions and Worker Exposure during Sanitary Sewer and Stormwater Pipe Rehabilitation Using Cured-in-Place-Pipe (CIPP). Environ Sci Technol Lett 2017;4:325–33. doi:10.1021/acs.estlett.7b00237.
- [6] Teimouri Sendesi SM, Ra K, Conkling EN, Boor BE, Nuruddin M, Howarter JA, et al. Worksite Chemical Air Emissions and Worker Exposure during Sanitary Sewer and Stormwater Pipe Rehabilitation Using Cured-in-Place-Pipe (CIPP). Environ Sci Technol Lett 2017;4:325–33. doi:10.1021/acs.estlett.7b00237.
- [7] Li X, Ra K, Mahboobeh S, Sendesi T, Howarter JA, Youngblood JP, et al. Outdoor manufacture of UV-Cured plastic linings for storm water culvert repair : Chemical emissions and residual. Environ Pollut 2019;245:1031–40. doi:10.1016/j.envpol.2018.10.080.
- [8] Ra K, Teimouri Sendesi SM, Nuruddin M, Zyaykina NN, Conkling EN, Boor BE, et al. Considerations for Emission Monitoring and Liner Analysis of Thermally Manufactured Sewer Cured-in-Place-Pipes (CIPP). J Hazard Mater 2019;371:540–9. doi:10.1016/j.jhazmat.2019.02.097.

- [9] Ra K, Mahboobeh S, Sendesi T, Howarter JA, Jafvert CT. Peer Reviewed Critical Review : Surface Water and Stormwater Quality Impacts of Cured-In-Place Pipe Repairs. *Journal-American Water Work Assoc* 2018;110:15–32. doi:10.1002/awwa.1042.
- [10] Hubbe MA, Ferrer A, Tyagi P, Yin Y, Salas C. com Nanocellulose in Thin Films, Coatings, and Plies for Packaging Applications: A Review. *BioResources* 2017;12:2143–233.
- [11] Stark NM. Opportunities for Cellulose Nanomaterials in Packaging Films : A Review and Future Trends. *J Renew Mater* 2016;4:313–26. doi:10.7569/JRM.2016.634115.
- [12] Harada R, Doherty I, Leffler S, Mcclanahan D, Osborn L. Factors Affecting Installed Cured-In-Place Pipe Liner Thickness. *North Am. Soc. Trenchless Technol.*, Washington, D.C.: 2011, p. pape.
- [13] Ashland. Hetron Q 6405 Resin. Safety data Sheet. Columbus, OH: 2012. doi:10.1021/ie50466a600.
- [14] Donaldson, Bridget M. Environmental Implications of Cured-in-Place Pipe Rehabilitation Technology. *J Transp Res Board* 2009:172–9. doi:10.3141/2123-19.
- [15] Tabor ML, Newman D, Whelton AJ. Stormwater chemical contamination caused by cured-in-place pipe (CIPP) infrastructure rehabilitation activities. *Environ Sci Technol* 2014;48:10938–47. doi:10.1021/es5018637.
- [16] Rahim K. The success of Styrene-free Cured-in-place pipe (CIPP) Resins. *Trenchless Technol. Roadshow*, Scotiabank Convention Center, ON: n.d.
- [17] Moore W. Non-Styrene Options For Cured In Place Pipe. *NASTT - No Dig*, Ft. Lauderdale, FL USA: n.d.
- [18] Mississippi Textile Corporation. MSDS of CIPP of Indiana installation sites. 2016.
- [19] Donaldson BM, Baker AJ. Understanding the Environmental Implications of Cured-in-Place Pipe Rehabilitation Technology Virginia Transportation Research Council Standard Title Page -Report on Federally Funded Project. Charlottesville, VA: 2008.
- [20] Ahmad M, Bajahlan AS. Leaching of styrene and other aromatic compounds in drinking water from PS bottles. *J Environ Sci* 2007;19:421–6. doi:10.1016/S1001-0742(07)60070-9.
- [21] Ajdari EB. Volatile Organic Compound (VOC) Emission during Cured-in-Place-Pipe (CIPP) Sewer Pipe Rehabilitation. University of New Orleans, 2016.
- [22] Lee, S. Y., & Springer GS. Effects of Cure on the Mechanical Properties of Composites. *J Compos Mater* 1988;22:15–29.

- [23] Alavi-Soltani S, Sabzevari S, Koushyar H, Minaie B. Thermal, rheological, and mechanical properties of a polymer composite cured at different isothermal cure temperatures. *J Compos Mater* 2012;46:575–87. doi:10.1177/0021998311415443.
- [24] Tang JM, Lee WI, Springer GS. Effects of cure pressure on resin flow, voids and mechanical properties. *J Compos Mater* 1987;21:421–40.
- [25] Olivier P, Cottu JP, Ferret B. Effects of cure cycle pressure and voids on some mechanical properties of carbon/epoxy laminates. *Composites* 1995;26:509–15. doi:10.1016/0010-4361(95)96808-J.
- [26] Bowles KJ, Frimpong S. Void effects on the interlaminar shear strength of unidirectional graphite fiber reinforced composites. *NASA STI/Recon Tech Rep N* 1992;26:1487–509.
- [27] Koushyar H. Effects of Variation in Autoclave Pressure, Cure Temperature, and Vacuum-Application Time on the Porosity and Mechanical Properties of a Carbon/Epoxy Composite. *Wichita State University*, 2011.
- [28] Almeida M De, Cerqueira M, Leali M. The influence of porosity on the interlaminar shear strength of carbon / epoxy and carbon / bismaleimide fabric laminates. *Compos Sci Technol* 2001;61:2101–8.
- [29] Dong C. Effects of Process-Induced Voids on the Properties of Fibre Reinforced Composites. *J Mater Sci Technol* 2016;32:597–604. doi:10.1016/j.jmst.2016.04.011.
- [30] Alzraiee H, Asce SM, Bakry I, Asce SM, Zayed T, Asce M. Destructive Analysis-Based Testing for Cured-in-Place Pipe. *J Perform Constr Facil* 2015;29:1–9. doi:10.1061/(ASCE)CF.1943-5509.0000567.
- [31] Eric Wood. Lining of passageways. U.S. Patent 4,064,211, 1977. doi:10.1016/j.(73).
- [32] Insituform Technologies I. Impregnated Insitutube® Product Material Safety Data Sheet. *Chesterfield, MO*: 2005.
- [33] Harrison Street Sewer Line Repair - 2016. Section 33 5500 - Sewer Pipe Lining (Cured-In-Place Pipe). 2016.
- [34] Allouche E, Alam S, Simicevic J, Sterling R, Condit W, Matthews J, et al. A pilot study for retrospective evaluation of cured-in-place pipe (CIPP) rehabilitation of municipal gravity sewers. *Tunn Undergr Sp Technol* 2014;39:82–93. doi:10.1016/j.tust.2012.02.002.
- [35] Young W Bin. Compacting pressure and cure cycle for processing of thick composite laminates. *Compos Sci Technol* 1995;54:299–306. doi:10.1016/0266-3538(95)00067-4.

- [36] Mackenzie KA. Measurement of Resin Pressure in Composite Laminates During Cure. University of British Columbia, 1993.
- [37] Liu X, Chen F. A review of void formation and its effects on the mechanical performance of carbon fiber reinforced plastic. *Eng Trans* 2016;64:33–51.
- [38] A. Rubin KJ. Evaluation of Porosity In Composite Aircraft. *Mech Compos Mater* 1994;30:587–600.
- [39] National Toxicology Program. Report on Carcinogens, 14th Edition. 2016.
- [40] Noh JH, Patala R, Meijboom R. Catalytic evaluation of dendrimer and reverse microemulsion template Pd and Pt nanoparticles for the selective oxidation of styrene using TBHP. *Appl Catal A Gen* 2016;514:253–66. doi:10.1016/j.apcata.2016.01.033.
- [41] AkzoNobel. Product data sheet.pdf 2015:1–3.
- [42] Alexander M. Environmental fate and effects of styrene. *Crit Rev Environ Sci Technol* 1997;27:383–410. doi:10.1080/10643389709388504.
- [43] Dhoot SN. SORPTION AND TRANSPORT OF GASES AND ORGANIC VAPORS IN POLY (ETHYLENE TEREPHTHALATE) SORPTION AND TRANSPORT OF GASES AND ORGANIC VAPORS IN POLY (ETHYLENE TEREPHTHALATE) by Sushil Naresh Dhoot , B . S ., M . S . Doctor of Philosophy The University of Te. The University of Texas at Austin, 2004.
- [44] Chowdhury NT, Wang J, Chiu WK, Yan W. Residual Stresses Introduced to Composite Structures Due to the Cure Regime: Effect of Environment Temperature and Moisture. *J Compos* 2016;2016:1–13.
- [45] Matthews J. Sewer Rehabilitation Using an Ultraviolet-Cured GFR Cured-in-Place Pipe. *Pract Period Struct Des Constr* 2015;20:04014021. doi:10.1061/(ASCE)SC.1943-5576.0000216.
- [46] Mark W. Hutchinson. North American Society for Trenchless Technology (NASTT) Learning about UV CIPP versus Steam and Water Cure CIPP in Portland Oregon. City of Portland, Portland Oregon: 2018.
- [47] Whelton AJ, Ra K, Mahboobeh S, Sendesi T, Nuruddin M, Li X, et al. Contaminant Release from Storm Water Culvert Rehabilitation Technologies : Understanding Implications to the Environment and Long-Term Material Integrity. vol. 5. 2019. doi:10.5703/1288284317089.

- [48] Kobos L, Mahboobeh S, Sendesi T, Whelton AJ, Boor BE, Howarter JA, et al. In vitro toxicity assessment of emitted materials collected during the manufacture of water pipe plastic linings. *Inhal Toxicol* 2019;31:131–46. doi:10.1080/08958378.2019.1621966.
- [49] Granite Inliner. UV Light-Cured CIPP n.d. <http://inliner.com/uploads/pdfstxbrochure.pdf>.
- [50] Ajdari EB. Volatile Organic Compound (VOC) Emission during Cured-in-Place-Pipe (CIPP) Sewer Pipe Rehabilitation. University of New Orleans, 2016.
- [51] W. Thomas Straughan LKG. Long-Term Structural Behavior of Pipeline Rehabilitation Systems. *J Infrastruct Syst* 1995;1:214–20.
- [52] John C. Matthews. Large-Diameter Sewer Rehabilitation Using a Fiber-Reinforced Cured-in-Place Pipe. *Pract. Period. Struct. Des. Constr.*, vol. 20, 2015, p. 04014031. doi:10.1061/(ASCE)SC.1943-5576.0000231.
- [53] Amir Mahdi Riahi. Short-Term and Long-Term Mechanical Properties of CIPP Liners. University of Waterloo, 2015.
- [54] Alam S, Matthews J, Sterling R, Allouche E, Selvakumar A, Condit W, et al. Evaluation of testing methods for tracking CIPP liners ' life-cycle performance Evaluation of testing methods for tracking CIPP. *Cogent Eng* 2018;5:1463594. doi:10.1080/23311916.2018.1463594.
- [55] Allouche E, Alam S, Simicevic J, Sterling R, Condit W, Matthews J, et al. A pilot study for retrospective evaluation of cured-in-place pipe (CIPP) rehabilitation of municipal gravity sewers. *Tunn Undergr Sp Technol Inc Trenchless Technol Res* 2014;39:82–93. doi:10.1016/j.tust.2012.02.002.
- [56] Nuruddin M, Mendis G, Ra K, Sendesi SMT, Futch T, Youngblood JP, et al. Evaluation of the physical , chemical , mechanical , and thermal properties of steam-cured PET / Polyester cured-in-place pipe (CIPP). *J Compos Mater* 2019;53:2687–99. doi:10.1177/0021998319839132.
- [57] Boinard E, Pethrick RA, Dalzel-job J, Dockyard RR, Ky F, Macfarlane CJ. Influence of resin chemistry on water uptake and environmental ageing in glass fibre reinforced composites-polyester and vinyl ester laminates. *J Mater Sci* 2000;35:1931–7.
- [58] Wang Y, Meng J, Zhao Q, Qi S. Accelerated Ageing Tests for Evaluations of a Durability Performance of Glass-fiber Reinforcement Polyester Composites. *J Mater Sci Technol* 2010;26:572–6. doi:10.1016/S1005-0302(10)60087-4.

- [59] Zhong Y, Cheng M, Zhang X, Hu H, Cao D, Li S. Hygrothermal durability of glass and carbon fiber reinforced composites – A comparative study. *Compos Struct* 2019;211:134–43. doi:10.1016/j.compstruct.2018.12.034.
- [60] Mouzakis DE, Zoga H, Galiotis C. Accelerated environmental ageing study of polyester / glass fiber reinforced composites (GFRPCs). *Compos Part B* 2008;39:467–75. doi:10.1016/j.compositesb.2006.10.004.
- [61] Lu T, Solis-ramos E, Yi Y, Kumosa M. Synergistic environmental degradation of glass reinforced polymer composites. *Polym Degrad Stab* 2016;131:1–8. doi:10.1016/j.polymdegradstab.2016.06.025.
- [62] Perreux D, Suri C. A study of the coupling between the phenomena of water absorption and damage in glass/epoxy composite pipes. *Compos Sci Technol* 1997;3538:1403–13. doi:10.1016/S0266-3538(97)00076-6.
- [63] Apicella A, Migliaresi C, Nicodemo L, Nicolais L, Iaccarino L, Roccotelli S. Water sorption and mechanical properties of a glass-reinforced polyester resin. *Composites* 1982;13:406–10. doi:10.1016/0010-4361(82)90151-3.
- [64] Robert M, Benmokrane B. Combined effects of saline solution and moist concrete on long-term durability of GFRP reinforcing bars. *Constr Build Mater* 2013;38:274–84. doi:10.1016/j.conbuildmat.2012.08.021.
- [65] Chen Y, Davalos JF, Ray I, Kim H. Accelerated aging tests for evaluations of durability performance of FRP reinforcing bars for concrete structures. *Compos Struct* 2007;78:101–11. doi:10.1016/j.compstruct.2005.08.015.
- [66] Ray BC. Temperature effect during humid ageing on interfaces of glass and carbon fibers reinforced epoxy composites. *J Colloid Interface Sci* 2006;298:111–7. doi:10.1016/j.jcis.2005.12.023.
- [67] Karbhari, V. M., K. Murphy and SZ. Effect of concrete based alkali solutions on short-term durability of E-glass/vinylester composites. *J Compos Mater* 2002;36:2101–21. doi:10.1106/002199802026977.
- [68] SAERTEX Multicom GmbH. SAERTEX-S-Liner, SAERTEX-M-Liner Product Safety Data Sheet. Saerbeck Germany: 2009.
- [69] DSM. ATLAC® E-Nova RE 3475 Safety Data Sheet. Schaffhausen Switzerland: 2011.
- [70] DSM. ATLAC® E-NOVA RE 3475 Product Data Sheet. Schaffhausen Switzerland: 2013.

- [71] Ghods P, Isgor OB, Bensebaa F, Kingston D. Angle-resolved XPS study of carbon steel passivity and chloride-induced depassivation in simulated concrete pore solution. *Corros Sci* 2012;58:159–67. doi:10.1016/j.corsci.2012.01.019.
- [72] ASTM D543 – 14. Standard Practices for Evaluating the Resistance of Plastics to Chemical Reagents. n.d. doi:10.1520/D0543-14.2.
- [73] ASTM D618 – 13. Standard Practice for Conditioning Plastics for Testing. n.d. doi:10.1520/D0618-13.2.
- [74] ASTM D2344/D2344M – 16. Standard Test Method for Short-Beam Strength of Polymer Matrix Composite Materials and Their Laminates. n.d. doi:10.1520/D2344.
- [75] Panaitescu I, Koch T, Archodoulaki V. Accelerated aging of a glass fiber / polyurethane composite for automotive applications. *Polym Test* 2019;74:245–56. doi:10.1016/j.polymertesting.2019.01.008.
- [76] Miyano Y, Nakada M, Sekine N. Accelerated testing for long-term durability of GFRP laminates for marine use. *Compos Part B* 2004;35:497–502. doi:10.1016/j.compositesb.2003.11.006.
- [77] Miyano Y. Accelerated testing for long-term strength of innovative CFRP laminates for marine use. *Compos Part B* 2008;39:5–12. doi:10.1016/j.compositesb.2007.02.009.
- [78] Aplcella A, Nicolais L. Environmental Aging of Epoxy Resins : Synergistic Effect of Sorbed Moisture , Temperature , and Applied Stress. *Ind Eng Chem Prod Res Dev* 1981;20:138–44. doi:10.1021/i300001a018.
- [79] J. P. Soulier, R. Berruet, A. Chateauminois, B. Chabert and RG. Interactions of fibre-reinforced epoxy composites with different salt water solutions including isotonic liquid. *Polym Commun* 1988;29:243–6.
- [80] Dana, H. R., Perronnet, A., Fréour, S., Casari, P., & Jacquemin F. Identification of moisture diffusion parameters in organic matrix composites. *J Compos Mater* 2013;47:1081–92. doi:10.1177/0021998313477963.
- [81] Pavlidou S, Krassa K, Papaspyrides CD. Woven Glass Fabric / Polyester Composites : Effect of Interface Tailoring on Water Absorption. *J Appl Polym Sci* 2005;98:843–51. doi:10.1002/app.22179.

- [82] Kingdom U. Moisture Diffusion in a Fiber-reinforced Composite : Part I – Non-Fickian Transport and the Effect of Fiber Spatial Distribution. *J Compos Mater* 2005;39:2113–41. doi:10.1177/0021998305052030.
- [83] Hodzic A, Kim JK, Lowe AE, Stachurski ZH. The effects of water aging on the interphase region and interlaminar fracture toughness in polymer – glass composites. *Compos Sci Technol* 2004;64:2185–95. doi:10.1016/j.compscitech.2004.03.011.
- [84] Chin JW, Nguyen T, Aouadi K. Sorption and Diffusion of Water , Salt Water , and Concrete Pore Solution in Composite Matrices. *J Appl Polym Sci* 1999;71:483–92. doi:10.1002/(SICI)1097-4628(19990118)71:3<483::AID-APP15>3.0.CO;2-S.
- [85] Salehi M, Krishnamurthy A, Forster AM, Hsiao KT, Whelton AJ. Polyester composite water uptake and organic contaminant release affected by carbon nanofiber reinforcements. *J Appl Polym Sci* 2016;43724:1–9. doi:10.1002/app.43724.
- [86] A P Chakraverty, U K Mohanty SCM and AS. Sea Water Ageing of GFRP Composites and the Dissolved salts. *IOP Conf. Ser. Mater. Sci. Eng.* Vol. 75. No. 1., IOP Publishing; 2015. doi:10.1088/1757-899X/75/1/012029.
- [87] A S Maxwell, W R Broughton GD and GDS. Review of Accelerated Aging methods and Lifetime Prediction Techniques for Polymeric Materials. *NPL Report DEPC MPR*, 16. 2005.
- [88] Rege, S. K. and SCL. Effect of Salt Water on Mechanical Properties of Fibre Reinforced Plastics. *Fibre Sci Technol* 1983;19:317–24. doi:10.1016/0015-0568(83)90017-9.
- [89] A. Caceres, R.M. Jamond, T.A. Hoffard LJM. Salt-fog accelerated testing of glass fiber reinforced polymer composites. *NFESC No. TR-2215-SHR*. 2002.
- [90] Bashir, S. T., Yang, L., Liggat, J. J., & Thomason JL. Kinetics of dissolution of glass fibre in hot alkaline solution. *J Mater Sci* 2018;53:1710–22. doi:10.1007/s10853-017-1627-z.
- [91] Kouassi SS, Andji J, Bonnet J, Rossignol S. Dissolution of waste glasses in high alkaline solutions. *Ceramics-Silikáty* 2010;54:235–40.
- [92] Li W, Ji C, Zhu H, Xing F, Wu J, Niu X. Experimental Investigation on the Durability of Glass Fiber-Reinforced Polymer Composites Containing Nanocomposite. *J Nanomater* 2013;2013. doi:http://dx.doi.org/10.1155/2013/352639.
- [93] Naebe, M., Abolhasani, M.M., Khayyam, H., Amini, A. and Fox B. Crack Damage in Polymers and Composites : A Review Crack Damage in Polymers and Composites : A Review. *Polym Rev* 2016;56:31–69. doi:10.1080/15583724.2015.1078352.

- [94] Zhu H, Leung CKY, Kim J, Liu M. Degradation of glass fiber-reinforced plastic composites containing nanoclay in alkaline environment. *J Compos Mater* 2011;45:2147–56. doi:10.1177/0021998311401064.
- [95] Basso M, Pupure L, Simonato M, Furlanetto R, Nardo L De, Jo R. Nonlinear creep behaviour of glass fiber reinforced polypropylene: Impact of aging on stiffness degradation. *Compos Part B* 2019;163:702–9. doi:10.1016/j.compositesb.2019.01.052.
- [96] Nayak RK. Influence of seawater aging on mechanical properties of nano-Al₂O₃ embedded glass fiber reinforced polymer nanocomposites. *Constr Build Mater* 2019;221:12–9. doi:10.1016/j.conbuildmat.2019.06.043.
- [97] Bagherpour S. Fibre Reinforced Polyester Composites. *Polyester, InTech*; 2012, p. 135–66.
- [98] Yao, J. and GZ. Water Absorption Behavior and Its Influence on Properties of GRP Pipe. *J Compos Mater* 2007;41:993–1008. doi:10.1177/0021998306067265.
- [99] Garland CA. Effect of manufacturing process conditions on the durability of pultruded vinyl ester / glass composites. West Virginia University, 2000.
- [100] Shahpanah M, Mehrabian S, Abbasi-firouzjah M, Shokri B. Surface & Coatings Technology Improving the oxygen barrier properties of PET polymer by radio frequency plasma-polymerized SiO_x N_y thin film. *Surf Coat Technol* 2019;358:91–7. doi:10.1016/j.surfcoat.2018.11.023.
- [101] Wu C, Liao R, Lai L, Jeng M, Liu D. Surface & Coatings Technology Organosilicon / silicon oxide gas barrier structure encapsulated flexible plastic substrate by using plasma-enhanced chemical vapor deposition. *Surf Coat Technol* 2012;206:4685–91. doi:10.1016/j.surfcoat.2012.05.080.
- [102] Liew Y-F, Yoon-Fei, Hu N-X, Chan HS-O, Xu G, Popovic Z. Investigation of the sites of dark spots in organic light-emitting devices. *Appl Phys Lett* 2000;77:2650. doi:10.1063/1.1320459.
- [103] Tihminlioglu F, Atik ID, Özen B. Water vapor and oxygen-barrier performance of corn – zein coated polypropylene films. *J Food Eng* 2010;96:342–7. doi:10.1016/j.jfoodeng.2009.08.018.

- [104] Christophliemk H, Johansson C, Ullsten H, Järnström L. Progress in Organic Coatings Oxygen and water vapor transmission rates of starch-poly (vinyl alcohol) barrier coatings for fl exible packaging paper. *Prog Org Coatings* 2017;113:218–24. doi:10.1016/j.porgcoat.2017.04.019.
- [105] Kim SW, Choi HM. Enhancement of thermal , mechanical , and barrier properties of ethylene vinyl alcohol copolymer by incorporation of graphene nanosheets : effect of functionalization of graphene oxide. *High Perform Polym* 2015;27:694–704. doi:10.1177/0954008314557051.
- [106] Kirwan MJ, Plant S, Strawbridge JW. Plastics in Food Packaging. In: Richard Coles and Mark Kirwan, editor. *Food Beverage Packag. Technol.*, Blackwell Publishing Ltd; 2011, p. 157–212.
- [107] Özen, İlhan and YZM. Barrier properties of polypropylene/poly (m-xylene adipamide) and polypropylene/poly (ethylene-co-vinyl alcohol) blend films. *J Plast Film Sheeting* 2010;26:377–94. doi:10.1177/8756087910397901.
- [108] Cutter CN. MEAT Opportunities for bio-based packaging technologies to improve the quality and safety of fresh and further processed muscle foods. *Meat Sci* 2006;74:131–42. doi:10.1016/j.meatsci.2006.04.023.
- [109] Chandra R, Rustgi R. BIODEGRADABLE POLYMERS. *Prog Polym Sci* 1998;23:1273–335.
- [110] Nuruddin M, Gupta R, Tcherbi-narteh A, Hosur M, Jeelani S. Thermal and Mechanical Properties of Cellulose Nanofibers Reinforced Polyvinyl Alcohol Composite Films. 69th FPS Int. Conv., Atlanta, GA: 2015.
- [111] Paulo J, Oliveira D, Pinheiro G, Lisie S, Cleber F, Renato A, et al. International Journal of Biological Macromolecules Cellulose nanocrystals from rice and oat husks and their application in aerogels for food packaging. *Int J Biol Macromol* 2019;124:175–84. doi:10.1016/j.ijbiomac.2018.11.205.
- [112] Clarkson CM, El SM, Azrak A, Schueneman GT, Snyder JF, Youngblood JP. Crystallization kinetics and morphology of small concentrations of cellulose nanofibrils (CNFs) and cellulose nanocrystals (CNCs) melt-compounded into poly (lactic acid) (PLA) with plasticizer. *Polymer (Guildf)* 2020;187:122101. doi:10.1016/j.polymer.2019.122101.

- [113] Chowdhury RA, Clarkson C, Youngblood J. Continuous roll-to-roll fabrication of transparent cellulose nanocrystal (CNC) coatings with controlled anisotropy. *Cellulose* 2018;25:1769–81. doi:10.1007/s10570-018-1688-4.
- [114] Chowdhury RA, Clarkson C, Apalangya VA, Islam SN, Youngblood JP. Roll-to-roll fabrication of cellulose nanocrystal-poly (vinyl alcohol) composite coatings with controlled anisotropy. *Cellulose* 2018;25:6547–60. doi:10.1007/s10570-018-2019-5.
- [115] Chowdhury RA. Roll-To-Roll Fabrication of Cellulose Nanocrystal Nanocomposite for Gas Barrier and Thermal Management Applications. Purdue University, 2019.
- [116] Mendoza-galv A, Tejeda-gal T, Dom AB, Araceli R, Järrendahl K, Arwin H. Linear Birefringent Films of Cellulose Nanocrystals Produced by Dip-Coating. *Nanomaterials* 2019;9:45. doi:10.3390/nano9010045.
- [117] Chowdhury RA, Clarkson CM, Shrestha S, El SM, Azrak A. coating based on a blocked isocyanate with cellulose nanocrystals (CNC) as the polyol. *ACS Appl Polym Mater* 2019. doi:10.1021/acsapm.9b00849.
- [118] Chowdhury RA, Rai A, Glynn E, Morgan P, Moore AL, Youngblood P. Superior , processing-dependent thermal conductivity of cellulose Nanocrystal-Poly (vinyl alcohol) composite films. *Polymer (Guildf)* 2019;164:17–25. doi:10.1016/j.polymer.2019.01.006.
- [119] Peng SX, Shrestha S, Yoo Y, Youngblood JP. Enhanced dispersion and properties of a two-component epoxy nanocomposite using surface modified cellulose nanocrystals. *Polymer (Guildf)* 2017;112:359–68. doi:10.1016/j.polymer.2017.02.016.
- [120] Hosur M V, Nuruddin M, Hubbard D, Tcherbi-narteh A, Jeelani S. Extraction of Cellulose and Lignin from Biomass and Their Use in Reinforcing Polymers and Synthesis of Phenolic Resins. 21st Int. Conf. Compos. Mater., Xi'an: 2017.
- [121] Nuruddin M, Hosur M, Mahdi TH, Jeelani S. Sensors & Transducers Flexural , Viscoelastic and Thermal Properties of Epoxy Polymer Composites Modified with Cellulose Nanofibers Extracted from Wheat Straw. *Sensors & Transducers* 2017;210:1–8.
- [122] Nuruddin M, Mahdi TH, Hosur M, Jeelani S. Mechanical and Thermal Properties of Cellulose Nanofibers Reinforced Epoxy Polymer Nanocomposites. ASC 29th Tech. Conf., San Diego, CA: 2014, p. 382.

- [123] Shrestha S, Chowdhury RA, Toomey MD, Betancourt D, Montes F, Youngblood JP. Surface hydrophobization of TEMPO-oxidized cellulose nanofibrils (CNFs) using a facile , aqueous modification process and its effect on properties of epoxy nanocomposites. *Cellulose* 2019;26:9631–43. doi:10.1007/s10570-019-02762-w.
- [124] Nuruddin M, Hosur M, Gupta R, Hosur G, Tcherbi-narteh A. Cellulose Nanofibers- Graphene Nanoplatelets Hybrids Nanofillers as High-Performance Multifunctional Reinforcements in Epoxy Composites. *Polym Polym Compos* 2017;25:273–84. doi:10.1177/096739111702500404.
- [125] Nuruddin M, Hosur M, Uddin MJ, Baah D, Jeelani S. A novel approach for extracting cellulose nanofibers from lignocellulosic biomass by ball milling combined with chemical treatment. *J Appl Polym Sci* 2016;133. doi:10.1002/app.42990.
- [126] Moon RJ, Martini A, Nairn J, Simonsen J, Youngblood J. *Chem Soc Rev. Chem Soc Rev* 2011;40:3941–94. doi:10.1039/c0cs00108b.
- [127] Nuruddin M, Chowdhury A, Haque SA, Rahman M, Farhad SF, Jahan MS, et al. Extraction and Characterization of Cellulose Microfibrils from Agricultural Wastes in an Integrated Biorefinery Initiative. *Cellul Chem Technol* 2011;45:347–54.
- [128] Nuruddin M, Hosur M, Triggs E, Jeelani S. Comparative Study of Properties of Cellulose Nanofibers from Wheat Straw Obtained by Chemical and Chemi-Mechanical Treatments. *ASME Int. Mech. Eng. Congr. Expo., Montreal, Canada: 2014.* doi:10.1115/IMECE2014-36174.
- [129] Diaz JA, Wu X, Martini A, Moon RJ. Thermal Expansion of Self-Organized and Shear-Oriented Cellulose Nanocrystal Films. *Biomacromolecules* 2013;14:2900–8. doi:10.1021/bm400794e.
- [130] Orts WJ, Godbout L, Marchessault RH, Revol J-F. Enhanced Ordering of Liquid Crystalline Suspensions of Cellulose Microfibrils : A Small Angle Neutron Scattering Study. *Macromolecules* 1998;31:5717–25. doi:10.1021/ma9711452.
- [131] Kvien I, Oksman K. Orientation of cellulose nanowhiskers in polyvinyl alcohol. *Appl PhysA* 2007;87:641–3. doi:10.1007/s00339-007-3882-3.
- [132] Habibi Y, Heim T, Douillard R. AC Electric Field-Assisted Assembly and Alignment of Cellulose Nanocrystals. *J Polym Sci Part B Polym Phys* 2008;46:1430–6. doi:10.1002/polb.

- [133] Gindl W, Emsenhuber G, Maier G, Keckes J. Cellulose in Never-Dried Gel Oriented by an AC Electric Field. *Biomacromolecules* 2009;10:1315–8.
- [134] Reising AB, Moon RJ, Youngblood JP. Effect of Particle Alignment on Mechanical Properties of Neat Cellulose Nanocrystal Films. *J Sci Technol For Prod Process* 2012;2:32–41.
- [135] Microcrystals C, Angle S. Shear-Induced Orientation Phenomena in Suspensions of Cellulose Microcrystals, Revealed by Small Angle X-ray Scattering. *Langmuir* 1999;15:6123–6.
- [136] Diaz JA, Wu X, Martini A, Moon RJ. Thermal Expansion of Self-Organized and Shear-Oriented Cellulose Nanocrystal Films. *Biomacromolecules* 2013;14:2900–2908. doi:10.1021/bm400794e.
- [137] Chowdhury RA, Nuruudin M, Clarkson C, Montes F, Howarter J, Youngblood P. Cellulose Nanocrystal (CNC) Coatings with Controlled Anisotropy as High-Performance Gas Barrier Films. *ACS Appl Mater Interfaces* 2019;11:1376–83. doi:10.1021/acsami.8b16897.
- [138] Sharma SK, Prakash J, Sudarshan K, Sen D, Mazumder S, Pujari PK. Structure at Interphase of Poly (vinyl alcohol) – SiC Nano fi ber Composite and Its Impact on Mechanical Properties: Positron Annihilation and Small-Angle X - ray Scattering Studies. *Macromolecules* 2015;48:5706–13. doi:10.1021/acs.macromol.5b01095.
- [139] Sharma SK, Sudarshan K, Sahu M, Pujari PK. Investigation of free volume characteristics of the interfacial layer in poly(methyl methacrylate)– alumina nanocomposite and its role in thermal behaviour. *RSC Adv* 2016;6:67997–8004. doi:10.1039/C6RA07051E.
- [140] Dryzek E, Wróbel M, Juszyńska-gałązka E. Free-Volume and Tensile Properties of Glass Fibre Reinforced Polyamide 6 Composites. *Acta Phys Pol A* 2017;132:1501–5. doi:10.12693/APhysPolA.132.1501.
- [141] Shrestha S, Diaz JA, Ghanbari S. Hygroscopic Swelling Determination of Cellulose Nanocrystal (CNC) Films by Polarized Light Microscopy Digital Image Correlation. *Biomacromolecules* 2017;18:1482–90. doi:10.1021/acs.biomac.7b00026.
- [142] Torstensen JØ, Liu M, Jin S, Deng L, Hawari AI, Syverud K, et al. Swelling and Free-Volume Characteristics of TEMPO-Oxidized Cellulose Nano fi bril Films. *Biomacromolecules* 2018;19:1016–25. doi:10.1021/acs.biomac.7b01814.

- [143] Dil EJ, Dhieb F Ben, Ajji A. Modeling the effect of nanoplatelets orientation on gas permeability of polymer nanocomposites. *Polymer (Guildf)* 2019;168:126–30. doi:10.1016/j.polymer.2019.02.024.
- [144] Chowdhury RA, Peng SX, Youngblood J. Improved order parameter (alignment) determination in cellulose nanocrystal (CNC) films by a simple optical birefringence method. *Cellulose* 2017;24:1957–70. doi:10.1007/s10570-017-1250-9.
- [145] Horst Czichos, Tetsuya Saito LS. *Springer Handbook of Materials Measurement Methods*. Springer; 2006.
- [146] Zeman S, Kubik L. Permeability of Polymeric Packaging Materials. *Tech Sci* 2007;26–34. doi:10.2478/v10022-007-0004-6.
- [147] Zekriardehani S, Jabarin SA, Gidley DR, Coleman MR. Effect of Chain Dynamics, Crystallinity, and Free Volume on the Barrier Properties of Poly(ethylene terephthalate) Biaxially Oriented Films. *Macromolecules* 2017;50:2845–55. doi:10.1021/acs.macromol.7b00198.
- [148] Sharma SK, Prakash J, Pujari PK. Effects of the molecular level dispersion of graphene oxide on the free volume characteristics of poly (vinyl alcohol) and its impact on the. *Phys Chem Chem Phys* 2015;17:29201–9. doi:10.1039/c5cp05278e.
- [149] Yampolskii YP, Korikov AP, Shantarovich VP, Nagai K, Freeman BD, Masuda T, et al. Gas Permeability and Free Volume of Highly Branched Substituted Acetylene Polymers. *Macromolecules* 2001;34:1788–96. doi:10.1021/ma000628u.
- [150] Sanders DF, Smith ZP, Ribeiro CP, Guo R, Mcgrath JE, Paul DR, et al. Gas permeability , diffusivity , and free volume of thermally rearranged polymers 2 , 2 -bis- (3 , 4-dicarboxyphenyl) hexafluoropropane dianhydride (6FDA). *J Memb Sci* 2012;409–410:232–41. doi:10.1016/j.memsci.2012.03.060.
- [151] Bharadwaj RK. Modeling the Barrier Properties of Polymer-Layered Silicate Nanocomposites. *Macromolecules* 2001;34:9189–92. doi:10.1021/ma010780b.
- [152] John Crank. *About Wiley Online Library Privacy Policy Advertisers & Corporate Partners Connect with Wiley The Wiley Network*. Academic Press; 1968.
- [153] Belbekhouche S, Bras J, Siqueira G, Chappey C, Lebrun L, Khelifi B, et al. Water sorption behavior and gas barrier properties of cellulose whiskers and microfibrils films. *Carbohydr Polym* 2011;83:1740–8. doi:10.1016/j.carbpol.2010.10.036.

- [154] Olson BG, Lin J, Nazarenko S, Jamieson AM. Positron annihilation lifetime spectroscopy of poly(ethylene terephthalate): Contributions from rigid and mobile amorphous fractions. *Macromolecules* 2003;36:7618–23. doi:10.1021/ma034813u.
- [155] George J, Sabapathi S. Cellulose nanocrystals : synthesis , functional properties , and applications. *Nanotechnol Sci Appl* 2015;8:45–54.
- [156] Siracusa V. Food packaging permeability behaviour: A report. *Int J Polym Sci* 2012;2012. doi:10.1155/2012/302029.
- [157] Jasse B, Seuvre AM, Mathlouthi M. Permeability and structure in polymeric packaging materials. *Food Packag Preserv* 1994:1–22. doi:10.1007/978-1-4615-2173-0_1.
- [158] Sajid Alavi, Sabu Thomas, K. P. Sandeep, Nandakumar Kalarikkal JV and SY, editor. *Polymers for packaging applications*. Apple Academic Press; 2014.
- [159] Dhoot SN. Sorption And Transport Of Gases And Organic Vapors In Poly(Ethylene Terephthalate) 2004:1–370.
- [160] Yeo JHO, Lee CH, Park C, Lee K. Rheological, Morphological, Mechanical, and Barrier Properties of PP/EVOH Blends. *Adv Polym Technol* 2001;20:191–201.
- [161] Hubbe MA, Ferrer A, Tyagi P, Yin Y, Salas C, Pal L, et al. Nanocellulose in Thin Films, Coatings, and Plies for Packaging Applications: A Review. *BioResources* 2017;12:2143–233. doi:10.15376/biores.12.1.2143-2233.
- [162] Bondeson D, Mathew A, Oksman K. Optimization of the isolation of nanocrystals from microcrystalline cellulose by acid hydrolysis. *Cellulose* 2006;13:171–80. doi:10.1007/s10570-006-9061-4.
- [163] Moon RJ, Martini A, Nairn J, Simonsen J, Youngblood J. Cellulose nanomaterials review: structure, properties and nanocomposites. vol. 40. 2011. doi:10.1039/c0cs00108b.
- [164] Beck-Candanedo S, Roman M, Gray DG. Effect of reaction conditions on the properties and behavior of wood cellulose nanocrystal suspensions. *Biomacromolecules* 2005;6:1048–54. doi:10.1021/bm049300p.
- [165] Garcia de Rodriguez NL, Thielemans W, Dufresne A. Sisal cellulose whiskers reinforced polyvinyl acetate nanocomposites. *Cellulose* 2006;13:261–70. doi:10.1007/s10570-005-9039-7.

- [166] Diaz JA, Ye Z, Wu X, Moore AL, Moon RJ, Martini A, et al. Thermal Conductivity in Nanostructured Films: From Single Cellulose Nanocrystals to Bulk Films. *Biomacromolecules* 2014;15:4096–4101. doi:10.1021/bm501131a.
- [167] Chowdhury RA, Nuruddin M, Clarkson C, Montes F, Howarter J, Youngblood P. Cellulose Nanocrystal (CNC) Coatings with Controlled Anisotropy as High-Performance Gas Barrier Films. *ACS Appl Mater Interfaces* 2019;11:1376–83. doi:10.1021/acsami.8b16897.
- [168] Shrestha S, Diaz JA, Ghanbari S. Hygroscopic Swelling Determination of Cellulose Nanocrystal (CNC) Films by Polarized Light Microscopy Digital Image Correlation. *Biomacromolecules* 2017;18:1482–1490. doi:10.1021/acs.biomac.7b00026.
- [169] Lin JH, Pan YJ, Liu CF, Huang CL, Hsieh CT, Chen CK, et al. Preparation and compatibility evaluation of polypropylene/high density polyethylene polyblends. *Materials (Basel)* 2015;8:8850–9. doi:10.3390/ma8125496.
- [170] Tyagi P, Hubbe MA, Lucia L, Pal L. High performance nanocellulose-based composite coatings for oil and grease resistance. *Cellulose* 2018;25:3377–91. doi:10.1007/s10570-018-1810-7.
- [171] Salo T, Dimic-misic K, Gane P PJ. Application of pigmented coating colours containing MFC/NFC: Coating properties and link to rheology. *Nord Pulp Pap Res J* 2015;30:165–78.
- [172] Chowdhury RA, Clarkson C, Apalangya VA, Islam SMN, Youngblood JP. Roll-to-roll fabrication of cellulose nanocrystal-poly (vinyl alcohol) composite coatings with controlled anisotropy. *Cellulose* 2019;25:6547–60. doi:10.1007/s10570-018-2019-5.
- [173] Cao Y, Zavattieri P, Youngblood J, Moon R, Weiss J. The relationship between cellulose nanocrystal dispersion and strength. *Constr Build Mater* 2016;119:71–9. doi:10.1016/j.conbuildmat.2016.03.077.
- [174] Liu Y, Shi C, Yuan Q, An X, Jiao D, Zhu L, et al. An amendment of rotation speed-torque transformation equation for the Herschel-Bulkley model in wide-gap coaxial cylinders rheometer. *Constr Build Mater* 2020;237:117530. doi:10.1016/j.conbuildmat.2019.117530.
- [175] Lee WJ, Clancy AJ, Kontturi E, Bismarck A. Strong and Stiff: High-Performance Cellulose Nanocrystal/Poly(vinyl alcohol) Composite Fibers. *ACS Appl Mater Interfaces* 2016;8:31500–4. doi:10.1021/acsami.6b11578.
- [176] Wang P, Hamad WY, MacLachlan MJ. in cellulose nanocrystal suspensions. *Nat Commun* 2016;7:1–8. doi:10.1038/ncomms11515.

- [177] Nassima El Miri, Faissal Aziz, Adil Aboulkas, Mehdi El Bouchti, Hicham Ben Youcef MEA. Effect of plasticizers on physicochemical properties of cellulose nanocrystals filled alginate bionanocomposite films. *Adv Polym Technol* 2018;3171–85. doi:10.1002/adv.22087.
- [178] Gray TAD and DG. Contact Angle Measurements on Smooth Nanocrystalline Cellulose (I) Thin Films. *J Adhes Sci Technol* 2011;25:699–708. doi:10.1163/016942410X525885.
- [179] Ollier RP, Alvarez VA. Surface properties of thermoplastic starch materials reinforced with natural fillers Chapter 5 Surface Properties of Thermoplastic Starch Materials Reinforced with Natural Fillers. *Funct. Biopolym.*, 2018, p. 131–58. doi:10.1007/978-3-319-66417-0.
- [180] Chowdhury RA, Nuruddin M, Clarkson C, Montes F, Howarter J, Youngblood JP. Cellulose Nanocrystal (CNC) Coatings with Controlled Anisotropy as High-Performance Gas Barrier Films. *ACS Appl Mater Interfaces* 2019;11:1376–83. doi:10.1021/acsami.8b16897.
- [181] Nair SS, Zhu JY, Deng Y, Ragauskas AJ. High performance green barriers based on nanocellulose. *Sustain Chem Process* 2014;2:23.
- [182] Mo, C., Yuan, W., Lei, W., & Shijiu Y. Effects of Temperature and Humidity on the Barrier Properties of Biaxially-oriented Polypropylene and Polyvinyl Alcohol Films. *J Appl Packag Res* 2014;6:40–6. doi:10.14448/japr.01.0004.
- [183] Dhoot SN. Sorption and transport of gases and organic vapors in poly (ethylene terephthalate). The University of Texas at Austin, 2004.
- [184] Krohn J, Chemicals E. Factors affecting the permeability of PE blown films. *J Plast Film Sheeting* 1997;13:327–35.
- [185] Ebeaufort ÄRICD, Espre DED. Edible Arabinoxylan-Based Films . 1 . Effects of Lipid Type on Water Vapor Permeability , Film Structure , and Other Physical characteristics. *J Agric Food Chem* 2002;50:3977–83. doi:10.1021/jf0116449.
- [186] Lange J, Wyser Y. Recent Innovations in Barrier Technologies for Plastic Packaging – a Review. *Packag Technol Sci* 2003;16:149–58. doi:10.1002/pts.621.
- [187] Zhang, Z., Britt, I. J., & Tung MA. Permeation of Oxygen and Water Vapor Through EVOH Films as Influenced by Relative Humidity. *J Appl Polym Sci* 2001;82:1866–72. doi:10.1002/app.2030.

- [188] Shanks RA, Li J, Yu L. Polypropylene-polyethylene blend morphology controlled by time-temperature-miscibility. *Polymer (Guildf)* 2000;41:2133–9. doi:10.1016/S0032-3861(99)00399-7.
- [189] Jin X, Li L, Xu R, Liu Q, Ding L, Pan Y. Effects of Thermal Cross-Linking on the Structure and Property of Asymmetric Membrane Prepared from the Polyacrylonitrile. *Polymers (Basel)* 2018;10:539. doi:10.3390/polym10050539.
- [190] Pauly S. *Polymer Handbook*. Third Edit. A Wiley-Interscience Publications; 1989.
- [191] Fong RJ, Robertson A, Mallon PE, Thompson RL. The Impact of Plasticizer and Degree of Hydrolysis on Free Volume of Poly (vinyl alcohol) Films. *Polymer (Guildf)* 2018;10:1036. doi:10.3390/polym10091036.
- [192] Ito K, Saito Y, Yamamoto T, Ujihira Y, Nomura K. Correlation Study between Oxygen Permeability and Free Volume of Ethylene-Vinyl Alcohol Copolymer through Positronium Lifetime Measurement. *Macromolecules* 2001;34:6153–5. doi:10.1021/ma001813a.
- [193] Mohamed HFM, Alaa HB. Positron Annihilation Lifetime Study of Pure and Doped Polyvinyl Chloride with Al₂O₃. 8th Arab Int. Conf. Polym. Sci. Technol., Cairo-Sharm El-Shiekh, EGYPT Positron: 2005.
- [194] Abdel-Hamed MO, Alaa HB. Free Volume and Electrical Conductivity in Pure and Doped Poly- vinyl Chloride with Al₂O₃. *Egypt J Phys* 2017;45:65–77.
- [195] Dhoot SN. Sorption and Transport of Gases and Organic Vapors in Poly (Ethylene Terephthalate). The University of Texas at Austin, 2004.
- [196] Callander DB. *Molecular Modeling of Polymer Free Volume Distribution*. Georgia Institute of Technology, 2005.
- [197] Lan Q, Yu J, Zhang J, He J. Nucleation Enhancement in Stereodefactive Poly (L -lactide) by Free Volume Expansion Resulting from Low-Temperature Pressure CO₂ Preconditioning. *Polymers (Basel)* 2018;10:120. doi:10.3390/polym10020120.
- [198] Luo C, Atvars TDZ, Meakin P, Hill AJ, Weiss RG, F1 D De. Determination of Initial and Long-Term Microstructure Changes in Ultrahigh Molecular Weight Polyethylene Induced by Drawing Neat and Pyrenyl Modified Films. *J AM CHEM SOC* 2003;125:11879–92. doi:10.1021/ja0362205.

- [199] Jeazet HBT, Koschine T, Staudt C, Raetzke K, Janiak C. Correlation of Gas Permeability in a Metal-Organic Framework MIL-101(Cr)–Polysulfone Mixed-Matrix Membrane with Free Volume Measurements by Positron Annihilation Lifetime Spectroscopy (PALS). *Membranes* (Basel) 2013;3:331–53. doi:10.3390/membranes3040331.
- [200] Sharma SK, Sudarshan K, Sahu M, Pujari PK. Investigation of free volume characteristics of the interfacial layer in poly(methyl methacrylate)– alumina nanocomposite and its role in thermal behaviour. *RSC Adv* 2016;6:67997–8004. doi:10.1039/c6ra07051e.
- [201] Erichsen J, Nagel C, K. G, Renner M, Altstädt V, Faupel F. Positron Annihilation Lifetime Measurements of Mechanically Fatigued Polystyrene Samples. *J Polym Sci Part B Polym Phys* 2008;46:1991–5. doi:10.1002/polb.
- [202] Soares BG, Almeida MSM, Ranganathaiah C, Urs MVD, Siddaramaiahb. The characterization of PP / NBR blends by positron annihilation lifetime spectroscopy (PALS): The effect of composition and dynamic vulcanization. *Polym Test* 2007;26:88–94. doi:10.1016/j.polymertesting.2006.08.009.
- [203] Ranade A, Wang H, Hiltner A, Baer E, Shirk JS, Lepkowicz RS. The solid state structure of polycarbonate blends with lead phthalocyanine. *Polymer (Guildf)* 2007;48:624–31. doi:10.1016/j.polymer.2006.11.008.
- [204] Barnard JL. The effect of chemical composition and morphology on the properties of polyolefin films. Stellenbosch University, 2018.
- [205] Ying Li RZ and YCJ. Principles and Applications of Positron and Positronium Chemistry. World Scientific Publishing Co Pte Ltd; 2003. doi:10.12677/mp.2017.74012.
- [206] Nakamura K, Kitagawa T, Nara S, Wakamatsu T, Ishiba Y, Kanehashi S, et al. Permeability of Dry Gases and Those Dissolved in Water through Hydrophobic High Free-Volume Silicon- or Fluorine-Containing Nonporous Glassy Polymer Membranes. *Ind Eng Chem Re* 2013;52:1133–40. doi:10.1021/ie300793t.
- [207] Winberg P, Desitter K, Dotremont C, Mullens S, Vankelecom IFJ, Maurer FHJ. Free Volume and Interstitial Mesopores in Silica Filled Poly (1-trimethylsilyl-1-propyne) Nanocomposites. *Macromol* 2005, 2005;38:3776–82.
- [208] Silva GG, Engenharia E De, Federal U, Gerais DM, Horizonte B, Federal U, et al. Polydimethylsiloxane Membranes Containing Multi-walled Carbon Nanotubes for Gas Separation. *Mater Res* 2017;20:1454–60.

- [209] Dreiss A, Cosgrove T, Benton NJ, Kilburn D, Alam MA, Schmidt RG, et al. Effect of crosslinking on the mobility of PDMS filled with polysilicate nanoparticles : Positron lifetime , rheology and NMR relaxation studies. *Polymer (Guildf)* 2007;48:4419–28. doi:10.1016/j.polymer.2007.05.070.

VITA

Md Nuruddin was born in Dhaka, Bangladesh. He achieved his Bachelor (2009) and Master's (2011) degrees in Applied Chemistry and Chemical Engineering from University of Dhaka, Dhaka, Bangladesh. He came to USA in 2012 and received his master's degree in Materials Science and Engineering in 2014 from Tuskegee University, Alabama, U.S.A. After graduation, he worked at center for Advanced Materials-Tuskegee University (TCAM) research lab as a Laboratory manager and then at Forest Product Lab-Auburn University as a research assistant. Then, he came to Purdue University (West Lafayette) in 2016 to pursue Ph.D. degree in Materials Engineering.

PUBLICATIONS

- **Nuruddin, M.**, DeCocker, K., Sendesi, S. M. T., Whelton, A., Youngblood, J., Howarter, A. (2020). Influence of Aggressive Environmental Aging on Mechanical and Thermo-Mechanical Properties of UV-Cured CIPP Liners. *Journal of Composite Materials*. DOI: 10.1177/0021998320913988.
- Kazım Köse, Miran Mavlan, **Md Nuruddin** & Jeffrey P. Youngblood (2020). TEMPO-oxidized cellulose nanofiber based polymeric adsorbent for use in iron removal. *Cellulose*. DOI: 10.1007/s10570-020-03104-x.
- **Md Nuruddin**, Reaz A. Chowdhury, Nelyan Lopez-Perez, Francisco J Montes, Jeffrey P. Youngblood¹, John Howarter (2020). The Influence of Free Volume Determined by Positron Annihilation Lifetime Spectroscopy (PALS) on Gas Permeability of Cellulose Nanocrystals Films. (Submitted to *ACS Applied Materials & Interfaces*)
- **Md Nuruddin**, Deepa M. Korani, Hyungyung Jo, Reaz A. Chowdhury, Francisco J Montes, John Howarter, Jeffrey P. Youngblood. Gas and Water Vapor Barrier Performance of Cellulose Nanocrystals-Citric Acid Coated Polypropylene for Flexible Packaging. (In preparation)
- **Nuruddin, M.**, Mendis, G., Ra, K., Sendesi, S. M. T., Futch, T., Goodsell, J., & Howarter, J. (2019). Evaluation of the physical, chemical, mechanical, and thermal properties of steam-cured PET/polyester cured-in-place pipe. *Journal of Composite Materials*. DOI: 10.1177/0021998319839132.
- Whelton, A. J., Ra, K., Teimouri Sendesi, S. M., **Nuruddin, M.**, Li, X., Howarter, J. A., & Zyaykina, N. N. (2019). Contaminant Release from Storm Water Culvert Rehabilitation Technologies: Understanding Implications to the Environment and Long-Term Material Integrity. FHWA TPF-5(339).
DOI: 10.5703/1288284317089
- Rencheck, M., Weiss, A. J., El Awad Azrak, S. M., Forti, E. S., **Nuruddin, M.**, Youngblood, J. P., & Davis, C. S. (2019). Nanocellulose Film Modulus Determination Via Buckling Mechanics Approaches. *ACS Applied Polymer Materials*.

- Ra, K., Sendesi, S. M. T., **Nuruddin, M.**, Zyaykina, N. N., Conkling, E. N., Boor, B. E., & Whelton, A. J. (2019). Considerations for Emission Monitoring and Liner Analysis of Thermally Manufactured Sewer Cured-in-Place-Pipes (CIPP). *Journal of Hazardous Materials*, 371,540-549.
- Li,X, Ra, K., **Nuruddin, M.**, Sendesi, S. M. T., Howarter, J. A., Youngblood, J. P., & Whelton, A. J. (2019). Outdoor manufacture of UV-Cured plastic linings for storm water culvert repair: Chemical emissions and residual. *Environmental Pollution*, 245, 1031-1040.
- Chowdhury, R. A., **Nuruddin, M.**, Clarkson, C., Montes, F., Howarter, J., & Youngblood, J. P. (2019). Cellulose Nanocrystal (CNC) Coatings with Controlled Anisotropy as High-Performance Gas Barrier Films. *ACS applied materials & interfaces*, 11(1), 1376-1383.
- Teimouri Sendesi, S. M., Ra, K., Conkling, E. N., Boor, B. E., **Nuruddin, M.**, Howarter, J. A., & Whelton, A. J. (2017). Worksite Chemical Air Emissions and Worker Exposure during Sanitary Sewer and Stormwater Pipe Rehabilitation Using Cured-in-Place-Pipe (CIPP). *Environmental Science & Technology Letters*, 4(8), 325-333.

PATENT

- **Md Nuruddin**, Jeffrey Paul Youngblood, Reaz A Chowdhury. Continuous Roll-To-Roll Fabrication of Cellulose Nanocrystal (CNC) Coatings” (**International Application No.: PCT/US2018/049312, Pub. No.: WO/2019/050819**).
- **Md Nuruddin**, Jeffrey Youngblood, Caitlyn Michelle Clarkson. Method for dispersion of nanocellulose in melt-processed polymers without the introduction of water/solvent during melt processing” (**U.S. patent application no. 62/739,369, Pub. No.: US 2020/0102425**).